



저작자표시-비영리-변경금지 2.0 대한민국

이용자는 아래의 조건을 따르는 경우에 한하여 자유롭게

- 이 저작물을 복제, 배포, 전송, 전시, 공연 및 방송할 수 있습니다.

다음과 같은 조건을 따라야 합니다:



저작자표시. 귀하는 원저작자를 표시하여야 합니다.



비영리. 귀하는 이 저작물을 영리 목적으로 이용할 수 없습니다.



변경금지. 귀하는 이 저작물을 개작, 변형 또는 가공할 수 없습니다.

- 귀하는, 이 저작물의 재이용이나 배포의 경우, 이 저작물에 적용된 이용허락조건을 명확하게 나타내어야 합니다.
- 저작권자로부터 별도의 허가를 받으면 이러한 조건들은 적용되지 않습니다.

저작권법에 따른 이용자의 권리는 위의 내용에 의하여 영향을 받지 않습니다.

이것은 [이용허락규약\(Legal Code\)](#)을 이해하기 쉽게 요약한 것입니다.

[Disclaimer](#)

**Ph.D. Dissertation of engineering**

**Material Engineering of Zinc Oxide  
Semiconductor for Solution-processed  
Thin Film Transistors**

용액형 박막 트랜지스터를 위한 산화 아연  
반도체의 소재 공정

**August 2015**

**Program in Nano Science and Technology  
Graduate School of Convergence Science and  
Technology, Seoul National University**

**Si Yun Park**

# **Material Engineering of Zinc Oxide Semiconductor for Solution-processed Thin Film Transistors**

**Examiner Youn Sang Kim**

**Submitting a Ph.D. Dissertation of Public  
Administration**

**June 2015**

**Program in Nano Science and Technology  
Graduate School of Convergence Science and Technology,  
Seoul National University**

**Si Yun Park**

**Confirming the Ph.D. Dissertation written by  
Si Yun Park**

**June 2015**

**Chair**                                박 원 철                                **(seal)**

**Vice Chair**                                김 연 상                                **(seal)**

**Examiner**                                송 윤 규                                **(seal)**

**Examiner**                                김 수 영                                **(seal)**

**Examiner**                                장 석 태                                **(seal)**

## **Abstract**

# **Material Engineering of Zinc Oxide Semiconductor for Solution-processed Thin Film Transistors**

Si Yun Park

Program in Nano Science and Technology

The Graduate School

Seoul National University

Metal oxide as the active layer of thin film transistors (TFTs) is widely known as unique properties such as transparency and flexibility. Various applications and designs, such as head-up display for cars, smart windows, display tables, smart cards and rollable smart phones are gradually feasible by using metal oxide. For next generation display applications, flexible and wide bandgap semiconducting materials with controlled carrier concentrations are indispensable. In addition, low-cost and large-area manufacturing processes are required for flexible devices on a

plastic substrate. Switching devices as a driving element in the active matrix displays (AM displays) are mostly implanted as TFTs based on ZnO and related oxides. Metal oxide semiconductor TFTs are substituting hydrogenated amorphous silicon (a-Si:H)-based TFTs in AM displays due to their transparency and superior electrical properties such as electron mobility and on/off current ratio. However, some noteworthy results have been reported for the low-temperature annealing and solution-processibility of ZnO, intrinsic ZnO semiconductors still show relatively inferior electron mobility. To address these issues, material engineering of ZnO is required for solution-process, doping process and mechanism analysis.

First, optimized fabrication method of ZnO thin films was investigated by three different zinc oxide sources. Zinc ammine complex is a new precursor for the low-temperature annealing process due to highly volatile property of ammonia. Direct dissolving pristine ZnO into ammonia water is the most efficient method for preparing the ZnO semiconductor precursor which was fabricated by three different zinc oxide sources.

Second, noble doping method for ZnO semiconductors was developed by employing alkali metal dopants. Metal oxide alloys including zinc cations, such as indium zinc oxide (IZO), indium gallium zinc oxide (IGZO) have excellent electrical properties with high field effect mobility. However, use of indium remains a significant challenge due to cost and strategic importance. Interstitial doping of alkali metal cation increases carrier concentration of ZnO semiconductor and affect field effect mobility of TFTs. Li doped ZnO TFTs exhibited excellent electrical properties, i.e., a field effect mobility of  $7.34 \text{ cm}^2/\text{V}\cdot\text{s}$  and an on/off current ratio of  $10^7$ .

Third, exact mechanism and a detailed analysis of the alkali metal dopants,

especially lithium, were discussed. Alkali metal doped ZnO films were investigated for crystallinity, morphology, interface of semiconductor/insulator, optical absorption, and chemical composition analysis with various analytic instruments. It was proved that alkali metal cation dopants locate at the interstitial site in the nanocrystalline ZnO structure and alkali metal dopants increase carrier concentrations of ZnO semiconductor. In addition, a spectroscopic analysis for optical absorption of alkali metal doped ZnO could be used for monitoring the electrical performance without damages.

Finally, alkali earth metal dopants were developed for high mobility and solution-processed ZnO TFTs. Generally, alkali earth metal, especially magnesium (Mg) is widely used for a carrier suppressor of zinc interstitial or oxygen vacancies. However, both magnesium and calcium locate at the interstitial site and increase carrier concentration in aqueous solution-processed ZnO semiconductors. The Ca doped ZnO TFTs (0.2 mol%) showed best performance after annealing at 300 °C and the field effect mobility was 6.02 cm<sup>2</sup>/V·s and the on/off current ratio was 10<sup>7</sup>.

In summary, material engineering of ZnO semiconductor was carried out for TFTs of flexible and transparent electronics. Zinc ammine complex is the alternative of carbon based ZnO precursor for low-temperature process. Alkali and alkali earth metal dopants has potential to achieve high value of field effect mobility in ZnO TFTs.

주요어 : TFTs, ZnO, metal oxide semiconductor, lithium dopant.

학 변 : 2010-22669

# Contents

<b>Abstract .....</b>	<b>I</b>
<b>Contents .....</b>	<b>IV</b>
<b>List of tables and figures .....</b>	<b>V</b>
<b>Abbreviations .....</b>	<b>XIII</b>
<b>Chapter 1. Introduction .....</b>	<b>1</b>
1.1 Reference .....	4
<b>Chapter 2. Literature review .....</b>	<b>5</b>
2.1 Introduction of thin film transistor .....	5
2.1.1 TFT .....	6
2.1.2 Operation of TFT .....	8
2.1.3 Parameters of TFT .....	9
2.1.4 Active matrix display .....	13
2.1.5 Alternatives to silicon .....	14
2.2 Metal oxide semiconductor .....	15
2.2.1 ZnO semiconductor .....	15
2.2.2 Structure and electrical properties of ZnO .....	16
2.2.3 Doping mechanism of ZnO .....	22
2.2.4 Interface trap of ZnO/dielectric layer .....	26
2.3 References .....	29
<b>Chapter 3. Experiments .....</b>	<b>33</b>
3.1 Materials .....	33
3.2 Fabrication of TFTs .....	36
3.3 Characterizations of TFTs .....	36
3.4 Analysis tools .....	37
3.4.1 AFM, HR-TEM and FFT-SAED pattern .....	38
3.4.2 X-ray photoelectron spectroscopy .....	39
3.4.3 UV-vis absorption spectroscopy .....	39
3.5 References .....	41
<b>Chapter 4. Optimization of zinc ammine complex precursors for ZnO TFTs.....</b>	<b>42</b>
4.1 Introduction .....	42
4.2 Results and discussion .....	45
4.2.1 Zinc ammine complex precursors .....	45
4.2.2 TFT performances with different ZnO sources .....	49
4.2.3 Structural, morphological, and chemical analysis of ZnO films .....	54
4.3 Reference .....	61

**Chapter 5. Alkali metal dopants for high-performance and low-temperature ZnO TFTs..... 63**

5.1 Introduction.....63  
5.2 Results and discussion.....65  
    5.2.1 Alkali metal doped ZnO TFTs .....65  
    5.2.2 Role of alkali metal dopants in ZnO semiconductor.....74  
    5.2.3 Ion gel dielectric layer for low operation voltage .....78  
5.3 Reference .....82

**Chapter 6. Characterization of alkali metal doped ZnO TFTs with various analytic tools ..... 85**

6.1 Introduction.....85  
6.2 Results and discussion.....88  
    6.2.1 Structure and morphology of alkali metal doped ZnO films.....88  
    6.2.2 Interface trap of alkali metal doped ZnO films.....94  
    6.2.3 Relation between doping concentration and mobility.....98  
    6.2.4 Optical analysis of alkali metal doped ZnO films.....99  
    6.2.1 Investigation of residual doping effect .....107  
6.3 Reference .....115

**Chapter 7. Enhancement of Electrical Properties for ZnO Thin Film Transistors by Alkali Earth Metal Doping .....119**

7.1 Introduction.....119  
7.2 Results and discussion.....120  
    7.2.1 Electrical properties of alkali earth metal doped ZnO TFTs .....120  
    7.2.2 Carrier concentration of alkali earth metal doped ZnO films .....124  
    7.2.3 Analysis of alkali earth metal doped ZnO films .....127  
    7.2.4 Positive bias test of alkali earth metal doped ZnO TFTs .....132  
7.3 Reference .....136

**Chapter 8. Conclusion..... 138**

**초록(국문)..... 141**

**List of tables and figures**

**Table 1.** Field effect mobility, turn on voltage, and on/off current ratio of pristine/alkali metal doped ZnO TFTs with 10 mol% of Li, 1 mol% of Na, 3 mal% of K, and 1 mol% of Rb.

**Table 2.** Field effect mobility and turn on voltage of TFTs based on pristine and

alkali metal doped ZnO films annealed at 500 °C with SiO<sub>2</sub> gate dielectric (Li 10 mol%, Na 1 mol%).

**Table 3.** E<sub>A</sub> and k<sub>B</sub>T<sub>0</sub> of pristine and Li doped ZnO TFTs (10 mol%).

**Table 4.** Field effect mobility and turn on voltage of TFTs based on pristine and alkali earth metal doped ZnO films annealed at 300 °C with SiO<sub>2</sub> gate dielectric (Mg 0.002 mol%, Ca 0.2 mol%).

**Table 5.** E<sub>A</sub> and k<sub>B</sub>T<sub>0</sub> of pristine, Mg (0.002 mol%), and Ca doped ZnO TFTs (0.2 mol%).

**Figure 1.1.** Images of transistors. (a) transistor could be thought as a switch. (b) symbol used to represent a transistor.

**Figure 1.2.** Schematic image of ZnO thin film transistor.

**Figure 1.3.** I-V characteristics of ZnO TFT. (a) output curve. (b) transfer curve.

**Figure 1.4.** Schematic image of wurtzite ZnO structure.

**Figure 1.5.** JCPDS card of 36-1451 data. (a) x-axis is d spacing (b) x-axis is 2-theta scale.

**Figure 1.6.** (a) hall mobility of bulk ZnO with respect to temperature. (b) hall carrier concentration of bulk ZnO with respect to temperature.

**Figure 1.7.** Ball and stick model of local atomic relaxations around the oxygen vacancy in the ZnO matrix. (a) neutral state, (b) +1 charge state, (c) +2 charge state.

**Figure 1.8.** The density of states distribution near the band edge of an amorphous semiconductor, showing the localized and extended states separated by the mobility edge.

**Figure 1.9.** Schematic density of state, Fermi-Dirac distribution, and the carrier concentration for intrinsic ZnO and alkali metal doped ZnO.

**Figure 2.1.** Photographs of pristine zinc ammine complex precursors which have various amounts of ammonia water. When the as-prepared solution was refrigerated for 5 hours, the pristine ZnO precursor in 12 ml ammonia water was dissolved well.

**Figure 2.2.** Photographs of zinc ammine complex precursors from intrinsic zinc hydroxide and zinc oxide. The table shows the maximum concentration of zinc ammine complex precursors.

**Figure 2.3.** Schematic image of sample preparation for cross-sectional HR-TEM.

**Figure 3.1.** Main reactions in the sol-gel process using metal alkoxides.

**Figure 3.2.** Reaction mechanism of ZnO made from a zinc ammine complex prepared with various zinc oxide sources: ZnO powder, intrinsic Zn(OH)<sub>2</sub>, precipitated Zn(OH)<sub>2</sub>.

**Figure 3.3.** <sup>1</sup>H-NMR spectra of zinc ammine complex with various zinc oxide sources. The <sup>1</sup>H-NMR data were obtained in ppm (δ) from the internal standard and chemical shift. (a) ZnO powder, (b) intrinsic Zn(OH)<sub>2</sub>, (c) precipitated Zn(OH)<sub>2</sub>.

**Figure 3.4.** (a), (b), and (c) transfer curves of ZnO TFTs made from a zinc ammine complex prepared with ZnO powder, intrinsic Zn(OH)<sub>2</sub>, and precipitated Zn(OH)<sub>2</sub>, respectively. (d) average field effect mobility of various ZnO TFTs. (e) Table of the electrical properties of various ZnO TFTs.

**Figure 3.5.** Output characteristic of various ZnO TFTs and the histogram of field effect mobility of various ZnO TFTs as one run at 300 °C. (a) device 1 (ZnO powder), (b) device 2 (intrinsic Zn(OH)<sub>2</sub>), (c) device 3 (precipitated Zn(OH)<sub>2</sub>) (d) histogram data of various ZnO TFTs.

**Figure 3.6.** The hysteresis behavior of various ZnO TFTs with SiO<sub>2</sub> gate dielectric. (a) device 1 (ZnO powder), (b) device 2 (intrinsic Zn(OH)<sub>2</sub>), (c) device 3 (precipitated Zn(OH)<sub>2</sub>).

**Figure 3.7.** (a), (b), and (c) evolution of the linear transfer curves of various ZnO TFTs, as a function of positive bias stress time (40 V, 0–6000 s), (d) relative threshold voltage shift ( $\Delta V_{th}$ ) of various ZnO TFTs as a function of stress time.

**Figure 3.8.** AFM images of various ZnO films made from a zinc ammine complex prepared with various zinc oxide sources (ZnO powder, intrinsic Zn(OH)<sub>2</sub>, and precipitated Zn(OH)<sub>2</sub>) on the SiO<sub>2</sub> substrate at the annealing temperature of 300 °C. (a), (b), and (c) AFM image of various ZnO films.

**Figure 3.9.** Cross-sectional HR-TEM images of various ZnO films made from a zinc ammine complex prepared with various zinc oxide sources (ZnO powder, intrinsic Zn(OH)<sub>2</sub>, and precipitated Zn(OH)<sub>2</sub>) on the SiO<sub>2</sub> substrate at the annealing temperature of 300 °C. (a), (b), and (c) HR-TEM image of various ZnO films.

**Figure 3.10.** Images of FFT-SAED patterns of various ZnO films made from zinc ammine complex prepared with various zinc oxide sources (ZnO powder, intrinsic Zn(OH)<sub>2</sub> and precipitated Zn(OH)<sub>2</sub>) by HR-TEM. (a) ZnO powder, (b) intrinsic Zn(OH)<sub>2</sub>, (c) precipitated Zn(OH)<sub>2</sub>.

**Figure 3.11.** The O 1s XPS spectrum of various ZnO films made from a zinc ammine complex prepared with various zinc oxide sources, (a) ZnO, (b) intrinsic Zn(OH)<sub>2</sub>, (c) precipitated Zn(OH)<sub>2</sub>. (d) the ratio of integrated area oxygen vacancy and total area in the various ZnO semiconductor films

**Figure 4.1.** AFM images of ZnO films. Root mean square roughness of ZnO films were 0.20 nm (Li 1 mol%), 0.19 nm (Li 3 mol%), 0.22 nm (Li 10 mol%), 0.24 nm (Li 15 mol%), and 0.21 nm (pristine ZnO).

**Figure 4.2.** Electrical characteristics of pristine/doped ZnO TFTs with SiO<sub>2</sub> gate dielectric. The channel length and width were 50 and 1000 μm, respectively. (a) transfer characteristics of Li doped ZnO TFTs with different doping concentrations

( $V_D = 40$  V). (b) field effect mobility of Li and Na doped ZnO TFTs as a function of doping concentration. (c) transfer characteristics of the ZnO TFTs based on ZnO doped with various alkali metals (10 mol% Li, 1 mol% Na, 3 mol% K, and 1 mol% Rb).

**Figure 4.3.** Output characteristics of ZnO TFTs based on (a) pristine, (b) Li doped ZnO (Li 10 mol%), (c) Na doped ZnO (Na 1 mol%), (d) K doped ZnO (K 3 mol%), (e) Rb doped ZnO (Rb 1 mol%) with  $\text{SiO}_2$  gate dielectric. The gate voltage was varied between 0 V and 60 V in steps of 12 V. The channel length and width were 50 and 1000  $\mu\text{m}$ , respectively.

**Figure 4.4.** Operational stability of a Li doped ZnO TFT (Li 10 mol%) and the hysteresis behavior of pristine and alkali metal doped ZnO TFTs with  $\text{SiO}_2$  gate dielectric. (a) evolution of transfer characteristics of a Li doped ZnO TFT during 40 continuous operations. (b) changes in the field effect mobility, turn on voltage, and on/off current ratio of a Li doped ZnO TFT during 40 continuous operations (c) pristine ZnO, (d) Li doped ZnO (Li 10 mol%), (e) Na doped ZnO (Na 1 mol%).

**Figure 4.5.** Transfer characteristics of Li doped ZnO TFTs (Li 10 mol%) and transfer characteristics of TFTs based on pristine and alkali metal doped ZnO films annealed at 500  $^\circ\text{C}$  with  $\text{SiO}_2$  gate dielectric (Li 10 mol%, and Na 1 mol%). (a) a maximum field effect mobility was calculated to be  $11.45 \text{ cm}^2/\text{V}\cdot\text{s}$  at  $V_D = 60\text{V}$ . (b) the channel length and width were 50 and 1000  $\mu\text{m}$ , respectively.

**Figure 4.6.** Schematic image of tetrahedral and octahedral site of hexagonal close-packed structure. Site size calculation of each interstitial sites.

**Figure 4.7.**  $\ln \mu$  vs.  $T^{-1}$  plots of pristine/Li doped ZnO TFTs with varied doping concentrations.

**Figure 4.8.** EDX results of (a) pristine and (b) Na doped ZnO (Na 1 mol%) films

annealed at 300°C . Note that nitrogen doping was not observed in the ZnO films utilized in this work.

**Figure 4.9.** Electrical properties of ion gel gated Li doped ZnO TFTs (10 mol% Li). (a) output and (b) transfer characteristics of an ion gel gated Li doped ZnO TFT (10 mol% Li). (c) static behavior of a resistor-loaded inverter with a Li doped ZnO TFT (10 mol% Li). (d) histogram of field effect mobility, turn on voltage, and on/off current ratio of ion gel gated Li doped ZnO TFTs.

**Figure 4.10.** Operational stability of an ion gel gated Li doped ZnO TFT (Li 10 mol%). (a) evolution of the linear transfer curves of an ion gel gated Li doped ZnO TFT. The gate bias during stress was 1 V. (b) changes in field effect mobility, turn on voltage, and on/off current ratio during 20 continuous operations. (c) dynamic stress test of an ion gel gated Li doped ZnO TFT during continuous cycling between ON ( $V_G = -1$  V) and OFF states ( $V_G = 3$  V) at 0.2 Hz.

**Figure 5.1.** Cross-sectional HR-TEM images of Li doped ZnO films on the SiO<sub>2</sub> substrate at annealing temperature 300 °C. (a) pristine ZnO film, (b) Li doped ZnO film with 1 mol%, (c) Li doped ZnO film with 10 mol% (the inset shows FFT-SAED patterns) and (d) Li doped ZnO film with 15 mol%.

**Figure 5.2.** Cross-sectional HR-TEM images of ZnO films with various Li doping concentration (0–15 mol%) and images of lattice parameter calculation.

**Figure 5.3.** Atomic force microscopy (AFM) images of Li doped ZnO films. The root mean square (RMS) roughness values of ZnO films were 0.429 nm (pristine ZnO), 0.565 nm (Li 1 mol%), 0.587 nm (Li 10 mol%), and 0.524 nm (Li 15 mol%).

**Figure 5.4.** (a) evolution of the transfer curves of pristine ZnO TFTs, as a function of bias stress time (0–6000 s). (b) evolution of the transfer curves of Li doped ZnO TFTs (10 mol%), as a function of bias stress time (0–6000 s). (c) relative threshold

voltage shift ( $\Delta V_{th}$ ) of Li doped ZnO TFTs (10 mol%) as a function of stress time. (d) plot of  $\Delta V_{th}/V_0$  vs. bias stress time for the pristine and Li doped ZnO (10 mol%) TFTs. The solid curves were fit to a stretched exponential equation.

**Figure 5.5.** Schematic images of band gap widening on disordered semiconductor.

**Figure 5.6.** (a) the transmittance data of Li doped ZnO films on the glass substrate. The inset shows that the transmittance was elevated and then declined with increasing Li concentration. (b) the  $(ah\nu)^2$  vs. photon energy plot of the Li doped ZnO films with various doping concentrations (0, 1, 10 and 15 mol%).

**Figure 5.7.** (a) the field effect mobility and optical band gap energy of Li doped ZnO semiconductors with various doping concentrations (0, 1, 10 and 15 mol%). (b) the box chart of optical band gap vs. Li doping concentration.

**Figure 5.8.** The average field effect mobility of Li doped ZnO TFTs as one run at 300 °C. (a) pristine ZnO. (b) Li doped ZnO (1 mol%). (c) Li doped ZnO (10 mol%). (d) Li doped ZnO (15 mol%).

**Figure 5.9.** The TGA data of various alkali metal doped ZnO films.

**Figure 5.10.** The wide scan spectrum of ZnO films annealed at 300 °C. (a) pristine ZnO film. (b) Li doped ZnO film (10 mol%). (c) Na doped ZnO film (1 mol%). The right plots show that the residual nitrogen (the peak at 398.1 eV) was not detected.

**Figure 5.11.** XPS spectra of alkali metals doped ZnO films. (a) Li peaks at 55.7 eV in Li doped ZnO films (10 mol%) and inset image is the XPS spectra of Li 1s. (b) Na peaks at 55.7 eV in Na doped ZnO films (1 mol%).

**Figure 5.12.** HR-TEM EDS results of (a) pristine and (b) Li doped ZnO (Li 1 mol%) films. (c) Li doped ZnO (Li 10 mol%) films. (d) Li doped ZnO (Li 15 mol%) films. Note that nitrogen doping was not observed in the ZnO films. All films were

annealed at 300 °C for 1 hour.

**Figure 5.13.** TOF-SIMS results of (a) pristine and (b) Li doped ZnO (Li 10 mol%) film. Etching rate and analysis area was 0.4 Å/s and 100 x 100 µm, respectively.

**Figure 6.1.** (a) mechanism of formation of aqueous precursor-derived ZnO, (b) transfer curves of TFTs based on ZnO semiconductor doped with various alkali earth metals (Mg 0.002 mol%, Ca 0.1 mol%, Ca 0.2 mol%).

**Figure 6.2.** Output characteristic of various ZnO TFTs. (a) pristine ZnO TFT, (b) Mg doped ZnO TFT (0.002 mol%), (c) Ca doped ZnO TFT (0.2 mol%).

**Figure 6.3.** Electrical properties of alkali earth metal doped ZnO films, (a) resistivity data of alkali earth metal doped ZnO films by Hall measurement, (b) bulk carrier concentration and the field effect mobility of ZnO TFTs as a function of various alkali earth metals.

**Figure 6.4.** (a) XRD profiles of the pristine and alkali earth metal doped ZnO powder, (b) TOF-SIMS data of pristine ZnO film, (c) TOF-SIMS data of Ca doped ZnO film (0.2 mol%).

**Figure 6.5.** Cross-sectional HR-TEM images of alkali earth metal doped ZnO films on the SiO<sub>2</sub> substrate at annealing temperature 300 °C. (a) pristine ZnO film, (b) Mg doped ZnO film with 0.002 mol%, (c) Ca doped ZnO film with 0.1 mol%, (d) Ca doped ZnO film with 0.2 mol%. The inset image shows crystalline FFT-SAED patterns.

**Figure 6.6.** Atomic force microscopy (AFM) images of alkali earth metal doped ZnO films. The root mean square (RMS) roughness values of ZnO films were 0.32 nm (pristine ZnO), 0.41 nm (Mg 0.002 mol%), 0.36 nm (Ca 0.1 mol%), and 0.408 nm (Ca 0.2 mol%).

**Figure 6.7.** The hysteresis behavior of pristine and alkali earth metal doped ZnO

TFTs with SiO<sub>2</sub> gate dielectric. (a) undoped ZnO, (b) Mg doped ZnO (Mg 0.002 mol%), (c) Ca doped ZnO (Ca 0.2 mol%).

**Figure 6.8.** (a), (b) and (c) evolution of the linear transfer curves of various ZnO TFTs, as a function of positive bias stress time (40 V, 0–4800 s), (d) relative field effect mobility of various ZnO TFTs, as a function of bias stress time (0–4800 s), (e) relative threshold voltage shift ( $\Delta V_{th}$ ) of various ZnO TFTs as a function of stress time, and (f) plot of  $\Delta V_{th}/V_o$  vs. bias stress time for pristine, Mg (0.002 mol%) and Ca doped ZnO (0.2 mol%) TFTs. The solid curves were fit to a stretched exponential equation.

**Figure 6.9.** (a), (b) and (c) evolution of the linear transfer curves of various ZnO TFTs, as a function of negative bias stress time (-40 V, 0–4800 s), (d) relative field effect mobility of various ZnO TFTs, as a function of bias stress time (0–4800 s), (e) relative threshold voltage shift ( $\Delta V_{th}$ ) of various ZnO TFTs as a function of stress time, (f) Plot of  $\Delta V_{th}/V_o$  vs. bias stress time for pristine, Mg (0.002 mol%) and Ca doped ZnO (0.2 mol%) TFTs. The solid curves were fit to a stretched exponential equation.

**Figure 6.10.** Variation in  $V_{th}$  of various ZnO TFTs to which 40 V and -40 V of gate bias stress was applied.

## Abbreviations

**TFT** thin film transistor

**AM** active matrix

**a-Si:H** hydrogenated amorphous silicon

**IZO** indium zinc oxide

**IGZO** indium gallium zinc oxide

**CRT** cathode ray tube

**FPD** flat panel display

**HUD** head-up display

**HR-TEM** high resolution transmission electron microscopy

**AFM** atomic force microscopy

**XPS** X-ray photoelectron spectroscopy

**EDS** energy-disperse X-ray spectroscopy

**UV-vis spectroscopy** ultraviolet-visible spectroscopy

**TCO** transparent conducting oxide

**XRD** X-ray diffraction

**MOSFET** metal oxide semiconductor field effect transistors

**TFT-LCD** thin film transistor-liquid crystal display

**AMOLED** active matrix organic light emitting diode

**LC** liquid crystal

**LTPS** low temperature polysilicon

**ELA** excimer laser annealing

**CMOS** complementary metal oxide semiconductor

**CBM** conduction band minimum

**JCPDS** joint committee on powder diffraction standard

**DOS** density of state

**DI water** deionized water

**PS-PMMA-PS** polystyrene-block-poly(methylmethacrylate)-block-polystyrene

**[EMIM][TFSI]** 1-ethyl-3-methylimidazolium bisimide(trifluoromethylsulfonyl)

**GI-WAXS** grazing incidence wide angle X-ray scattering

**FFT-SAED** fast fourier transform selective area electron diffraction

**PMMA** polymethylmethacrylate

**NMR** nuclear magnetic resonance

**RMS** root mean square

**PLD** pulsed laser deposition

**RF** sputtering radio frequency sputtering

**MOCVD** metal organic chemical vapor deposition

**ALD** atomic layer deposition

**QSE** quantum confinement size effect

**TGA** thermal gravimetric analysis

**TOF-SIMS** time of flight secondary ion mass spectroscopy

**ICP-AES** inductively coupled plasma-atomic emission spectroscopy

# Chapter 1. Introduction

The change of shape is the key issue of progress in display applications from cathode ray tube (CRT) TVs to flat panel display (FPD). The issue of transparent and flexible displays has been investigated for the next generation of advanced display. Numerous application and designs, such as head-up displays (HUD), transparent active-matrix (AM) displays in windows or as transparent TVs, functional furniture with invisible electronics and augmented-reality devices are based on transparency and flexibility. For that, transparent and flexible semiconductors with controllable carrier concentrations are indispensable. Oxide semiconductor, especially ZnO, is the promising semiconductors which have the ability to production possibility at a low-temperature and solution-process.<sup>1</sup> ZnO have wide band gap ( $E = 3.3$  eV) and intermediate carrier concentration ( $10^{14}$ – $10^{18}$   $\text{cm}^{-3}$ ) by alloying with indium and gallium.<sup>2</sup>

Solution-process which enables continuous mass production is another key issue of low-cost production.<sup>3</sup> Annealing procedure which induces chemical bonding and evaporation of solvent is essential for solution-process. Although thermal energy is sufficiently applied to solution-process based on zinc acetate, residual carbons in ZnO semiconductor exist and generate the barrier to electron transportation. In order to remove these residual carbon completely, high temperature ( $400$  °C) should be applied, and this restricts the substrate to being a rigid one.<sup>4,5</sup> In addition, indium has been introduced in order to compensate for the poor electrical properties of pristine ZnO.<sup>6</sup> Despite good property of indium, there are significant challenges due to high cost.

To address these issues, carbon-free ZnO precursors, alkali metal dopants, alkali

earth metal dopants were developed for low-temperature, high performance, and solution-processed ZnO TFTs.<sup>7,8,9,10</sup> In chapter 2, review of thin film transistor and active matrix display are introduced. This part gives an insight into the crystal structure and electrical properties of ZnO and oxide semiconductors. Especially, the doping mechanism and the role of defects which affect the performance of oxide semiconductor-based electronic devices are presented.

In chapter 3, detailed experiments such as procedure of precursor preparation, fabrication of TFT, materials, doping method, and analysis tools were described.

In chapter 4, zinc ammine complex for low-temperature processed ZnO TFTs was proposed by various zinc oxide sources such as ZnO, intrinsic Zn(OH)<sub>2</sub>, and precipitated Zn(OH)<sub>2</sub>.<sup>7</sup> To confirm coordination chemistry of zinc ammine complex, <sup>1</sup>H-NMR spectra was used. The chemical intermediate in ZnO semiconductor films was identical irrespective of the type of zinc oxide source in the zinc ammine complex precursor. Among three different zinc oxide sources, directly dissolving pristine ZnO into ammonia water is the most efficient method for preparing the ZnO semiconductor precursor.

In chapter 5, alkali metal doped ZnO TFTs were proposed by employing alkali metal doping such as Li, Na, K or Rb. Li doped ZnO TFTs exhibited excellent device performance with a field effect mobility of 7.3 cm<sup>2</sup>/V·s and an on/off current ratio of more than 10<sup>7</sup>.<sup>8</sup> These all alkali metal doped ZnO TFTs were fabricated at maximum process temperature as low as 300 °C, which is compatible with flexible plastic substrates. In addition, Li doped ZnO TFTs with high on-current, low-voltage operation, and excellent operational stability were successfully demonstrated using of the ion gel gate dielectrics.

In chapter 6, the structural, electrical and optical characterizations of Li doped

ZnO TFTs were investigated by various analytic instruments, including HR-TEM, AFM, XPS, EDS, electrical bias stability test and UV-vis spectroscopy.<sup>9</sup> A change in the optical bandgap of Li doped ZnO films explains a trade-off relationship with the field effect mobility of Li doped ZnO TFTs and the doping concentrations.

In chapter 7, alkali earth metal dopants were introduced for high field effect mobility of TFTs.<sup>10</sup> Generally, transparent conducting oxide (TCO) materials, such as indium oxide and indium zinc oxide, can be transformed as semiconductors of TFTs using alkali earth metal dopants as the carrier suppressor. In this result, however, Ca doped ZnO TFTs enhanced electrical performance with the field effect mobility of  $6 \text{ cm}^2/\text{V}\cdot\text{s}$  and on/off current ratio of  $10^7$ . Moreover, the origin of the enhancement in electrical properties with alkali earth metal dopants in ZnO semiconductor was investigated using XRD, Hall measurement.

Finally, in chapter 8, the overall conclusion of this dissertation and future work for continuation of the research is presented.

## 1.1 Reference

- [1] E. Fortunato, P. Barquinha, R. Martins, *Adv. Mater.* 2012, **24**, 2945.
- [2] H. Frenzel, A. Lajn, H. von Wenckstern, M. Lorenz, F. Schein, Z. P. Zhang, M. Grundmann, *Adv. Mater.* 2011, **23**, 1424.
- [3] S. J. Kim, S. Yoon, H. J. Kim, *Jpn. J. Appl. Phys.* 2014, **53**, 02BA02.
- [4] Y. Natsume, H. Sakata, *Thin Solid Films.* 2000, **372**, 30.
- [5] C. G. Choi, S. J. Seo, B. S. Bae, *Electrochem. Solid. St.* 2008, **11**, H7.
- [6] K. Nomura, H. Ohta, A. Takagi, T. Kamiya, M. Hirano, H. Hosono, *Nature.* 2004, **432**, 488.
- [7] S. Y. Park, S. Kim, J. Yoo, K. H. Lim, E. Lee, K. Kim, J. Kim, Y. S. Kim, *RSC Adv.* 2014, **4**, 11295.
- [8] S. Y. Park, B. J. Kim, K. Kim, M. S. Kang, K. H. Lim, T. Il Lee, J. M. Myoung, H. K. Baik, J. H. Cho, Y. S. Kim, *Adv. Mater.* 2012, **24**, 834.
- [9] S. Y. Park, K. Kim, K. H. Lim, B. J. Kim, E. Lee, J. H. Cho, Y. S. Kim, *J. Mater. Chem. C.* 2013, **1**, 1383.
- [10] S. Y. Park, K. Kim, K. H. Lim, E. Lee, S. Kim, H. Kim, Y. S. Kim, *RSC Adv.* 2013, **3**, 21339.

## Chapter 2. Literature review

### 2.1 Introduction of thin film transistor

Silicon based metal oxide semiconductor field effect transistors (MOSFET) which was reported by Atalla and Khang at Bell Labs in 1960 are the most commercially used elements of electronics.<sup>1</sup> The MOSFET is an electrical switch which is integrated of billions of transistors in all smart technology such as computers, smart phones, and tablets. However, MOSFETs have critical limitation that they must be fabricated on a single crystal wafer. Due to the complex manufacturing process of single crystalline silicon, MOSFET based electronics have limitation of maximum size of devices.

Demand on large size of electronics such as flat panel displays (FPD) led to invention of thin film transistors (TFTs).<sup>2</sup> TFTs use thin film of semiconductor as an active layer instead of bulk silicon wafer. The significant advantage of TFTs is capability which can be deposited at low-temperature, large-area. Replacement of silicon wafer enables use of various substrate and shapes including glass and plastic.<sup>3</sup>

MOSFET based on silicon has no optical transparency due to the small bandgap (1.4 eV) of silicon. For innovation, industry requires new semiconductor which have high electrical properties and optical transparency at visible range. In a search of alternatives for amorphous silicon, considerable interest has focused on the wide bandgap materials for next generation electronic applications. Metal oxide semiconductors have optical transparency at visible region, and have excellent electrical properties with high electron mobility, chemical stability, and solution-processability.<sup>4</sup> Up to now, technology of TFT has brought electronics from small

size devices to fancied devices. Detailed expositions of TFTs will be discussed.

### 2.1.1. TFTs

A transistor is basically switching device which controls output signal. As shown in figure 1.1, there are three terminals (input 1, input 2, and output) in one transistor. The transistor will be 'on', when the signal of input 1 pass from input 1 to output. Also, the transistor will be 'off', when the signal does not pass from input 1 to output. Consequently, input 2 determines whether the switch is 'on' or 'off'. TFT which act as a switch has five parts such as drain, source, gate, semiconductor, and dielectric layer.

**Drain:** The drain is an input that is biased at some static bias value. It is called the drain because when the transistor is 'on' electrons will flow into this electrode.

**Source:** The source is the output electrode. It is called the source because when the transistor is 'on' electrons flow from this electrode to the drain. The distance between source and drain is called the channel length.

**Semiconductor:** The semiconductor is the material which connects the drain and source. Semiconductor turned from the insulator to the conductor by induced electric field.

**Gate:** The gate is the second input which applies electric field through dielectric layer. Gate controls flow of electrons from the source to drain by biased voltage of gate electrode.

**Dielectric layer:** The dielectric layer has two main purposes; one is preventing of static charge or dynamic charge injection. The other is inducing dipole moment which applies electric field to semiconductors.

In figure 1.2, schematic image shows the five parts of TFT.

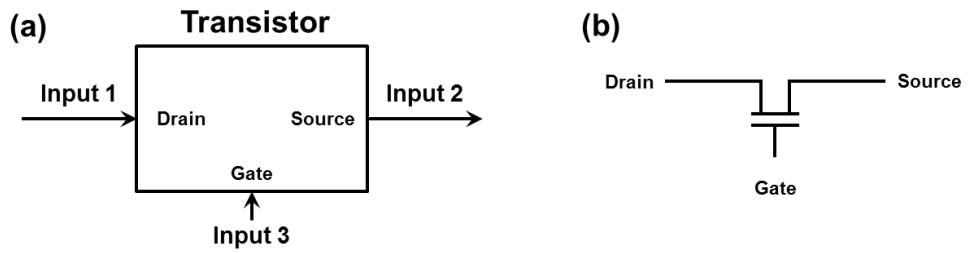


**Figure 1.1.** Images of transistors. (a) transistor could be thought as a switch. (b) symbol used to represent a transistor.

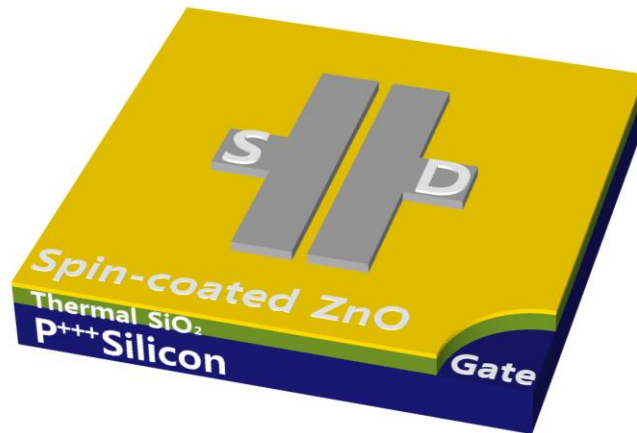


**Figure 1.2.** Schematic image of ZnO thin film transistor.

### **2.1.2. Operation of TFTs**

In terms of operation, TFTs are quite similar to MOSFET because TFTs are one of the field effect transistors. The turn-on of TFTs relies on the modulation of the current flowing in a semiconductor between source and drain. Control of electron flowing is achieved by the capacitive injection of carrier close to the dielectric layer/semiconductor interface. Carrier accumulation is achieved when gate voltage is applied higher than the threshold voltage, corresponding to downward band-banding of the semiconductor close to its interface with the dielectric layer. Depend on types of charge carriers, TFTs are classified under two types which are determined by existence of electrons or holes in the semiconducting channel; n-type and p-type.<sup>5</sup>

MOSFETs use silicon wafer as the substrate and the semiconductor. Remarks of MOSFETs are the formation of channel layer. When a positive voltage is applied on the gate electrode (n-type), the electric field is applied through dielectric layer and creates an 'inversion layer'. Inversion means that the interface of semiconductor/dielectric layer changes to n-type when the substrate is p-type. Saturation of drain current is induced by pinch-off which are indicated the lack of channel region near the drain electrode.

Meanwhile, TFTs have no inversion layer because TFT use deposited semiconductor and an insulating substrate such as glass and plastic substrate. Although MOSFET have high electrical performance due to the high electron mobility of single crystal silicon semiconductors, TFTs have advantage such as ability of low-temperature process and large-area production.

### 2.1.3. Parameters of TFTs

As mention above, increase of current is saturated by pinch-off and different operation is divided into two parts, linear and saturation regions.<sup>1</sup>

**Pre-pinch-off region (linear region):** Drain current ( $I_D$ ) is described by equation 1 at  $V_D < V_G - V_T$ ,

$$I_D = C_i \mu_{FET} \frac{W}{L} [(V_G - V_T)V_D - \frac{1}{2} V_D^2] \quad (1)$$

where  $C_i$  is the gate capacitance per unit area,  $\mu_{FET}$  is the field effect mobility,  $W$  is the channel width and  $L$  is the channel length. For very low  $V_D$ , a quadratic term could be neglected.

**Post-pinch-off region (saturation region):** Drain current ( $I_D$ ) is described by equation 2 at  $V_D > V_G - V_T$ ,

$$I_D = C_i \mu_{sat} \frac{W}{2L} (V_G - V_T)^2 \quad (2)$$

where  $\mu_{SAT}$  is the saturation mobility. In saturation region, the semiconductor close to the drain electrode becomes depleted and increase of drain current is saturated.

The equations of the ideal operation of TFTs are based on gradual channel approximation which was proposed by Shockley. This approximation assumes that the voltages vary gradually along the channel from the drain to the source. Also, they vary perpendicularly to the channel moving from the gate to the semiconductor. The characteristics of TFTs are extracted by their output and transfer curves, shown in figure 1.3.a and b, respectively.

As shown in output characteristic (figure 1.3.a),  $V_D$  is swept for proportional  $V_G$ , linear and saturation regimes are clearly assessed. The plateau of output curve at saturation regime could be used for evaluation whether the channel of semiconductor is fully depleted close to the drain electrode. Flatness of  $V_D$ - $I_D$  curve

at saturation region is essential for electronics because TFTs are used as a current limiter.

Transfer characteristics (figure 1.3.b), where proportional  $V_G$  is swept for a constant  $V_D$ , can be used for extraction of a large number of quantitative electrical parameters.

**On/off current ratio:** This parameter is defined as the ratio of the maximum to minimum drain current. On/off current ratio above  $10^6$  are commercially required in TFTs as electronic switches.<sup>5</sup>

**Threshold voltage:** In n-type TFTs, the devices are classified as enhancement or depletion mode, whether the threshold voltage is positive or negative, respectively.  $V_T$  is the minimum gate voltage to induce channel in semiconductor. The threshold voltage could be determined using different methodologies, such as linear extrapolation of the  $I_D^{1/2}$ - $V_G$  plot or GM-MAX method.<sup>6</sup> However, there is ambiguity in the determination of threshold voltage. The idea of turn-on voltage is widely used, corresponding to necessary potential to fully turn on the transistor.

**Subthreshold swing:** Subthreshold swing (SS) indicates the minimum voltage to increase drain current by one decade.

$$S = \left( \frac{d \log(I_D)}{dV_G} \Big|_{\max I_D} \right)^{-1} \quad (3)$$

Generally, 0.1–0.3 V/dec and small values result in higher speeds and lower power consumption.

**Field effect mobility:** Mobility is directly related to the efficiency of carrier transport of the active material, affecting maximum drain current and operating frequency. In n-type materials, electron mobility of semiconductor is function of several factor of mechanism, such as lattice vibration, impurities, and grain

boundaries. Moreover, scattering at interface is considered, because transportation of electron is restricted to a thin region close to the interface of dielectric/semiconductor.

$$\mu_{\text{SAT}} = \left( \frac{d\sqrt{I_D}}{dV_G} \right)^2 \bigg/ \frac{1}{2} C_i \frac{W}{L} \quad (4)$$

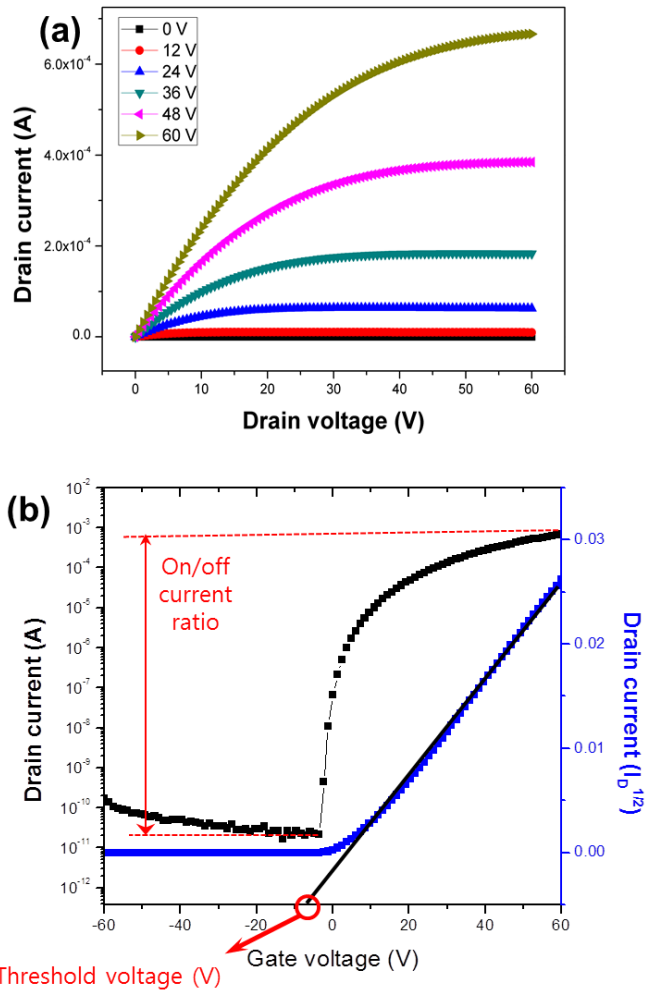


**Figure 1.3.** I-V characteristics of ZnO TFT. (a) output curve. (b) transfer curve.

#### **2.1.4. Active matrix display**

Most common application of TFT is TFT-LCD devices, reducing crosstalk between pixels and improving image quality. Active matrix organic light emitting diode (AMOLED) display also contains a TFT layer. The use of separated TFT for each pixel in the display allows for fast drawing of images without distortion. Herein, these driving methods for display will be discussed. There are two methods to draw images on display: segment driving (or passive matrix) and matrix driving.

The passive matrix driving method is widely used for simple display such as watch and calculator which are directly connected to the drivers. The active matrix is designed for high resolution displays. Each pixel is individually connected a grid of transistors with the ability to hold a charge for a limited period of time. The pixel remains active until the next refresh signal due to the ability of TFTs.

In TFT-LCD, birefringence of nematic liquid crystal (LC) is generally used for control of light. As the electric field from gate electrode is turned on, LC will be twisted and light will pass through. The twist structure of the LC causes the polarization of the light to rotate by a designed angle, when linearly polarized light passes through LC. Conversely, when gate electrode is turned off, light does not pass through the cross-polarized plate and it results in a dark image with lighted background.

In OLED display, there are several advantages such as wide view angle, high contrast, and fast response time because OLED is emissive display.<sup>7</sup> However, an OLED is a current-controlled device and current-controlled circuits are very difficult to accomplish. As the instability of threshold voltage is the main issue of metal oxide TFTs, this is the barrier in implementing an AMOLED for display

products.

### **2.1.5. Alternatives to silicon**

Single crystalline silicon has an electron mobility of  $1417 \text{ cm}^2/\text{V}\cdot\text{s}$  due to the movement through the conduction band of uniform crystal.<sup>8</sup> However, amorphous silicon has an electron mobility of  $1 \text{ cm}^2/\text{V}\cdot\text{s}$  because electron transportation mechanism is degraded to a disordered matrix.<sup>9</sup> To compensate the low mobility of amorphous silicon, researchers developed re-crystallize method which will recover some of its crystal properties. There are several methods of recrystallization and the most commercial method is low temperature polysilicon (LTPS) by excimer laser annealing (ELA).<sup>10</sup> Although LTPS is regarded to clear winner in electron mobility, stability, and capability of CMOS, complexity of process and high investment and high temperature are obstacles for future display.

Organic materials have been a topic of research in the two decades and the commercialization of OLED in display is completed. Organic TFTs showed the advantage of low-temperature and solution-process, and flexible electronics, but still suffer from low mobility for p-type TFTs.<sup>11</sup>

The oxide semiconductors were derived from the results of transparent conductive oxides (TCOs).<sup>4</sup> Distinctive electrical properties of oxide semiconductor are caused by the conduction band minimum (CBM), which works as an electron pathway due to the s-orbital overlap when the principle quantum number is higher than 4.<sup>12</sup> Since the high-performance n-type indium-gallium-zinc oxide (IGZO) TFTs are successfully demonstrated, decade of intense research has established a framework according to the contribution of each cations such as In, Sn, Ga, and Zn.

## 2.2 Metal oxide semiconductor

In ionic semiconductors, the magnitude of the overlap in orbitals could be insensitive to the variation of bond angle because the s-orbitals are isotropic sphere shape. Thus, some materials could have high electron mobility in amorphous state due to this overlap of orbitals. Hosono *et al.* found the transparent semiconductor oxides constituting of heavy post transition metal cations with an electron configuration  $(n-1)d^{10}ns^0$ , where  $n \gg 5$ .<sup>13</sup> In case of crystalline oxide such as ZnO, this condition is loosened 4.

For using metal oxide as semiconducting layer, there is a critical issue of controllability of carrier concentration. Control of carrier concentration of metal oxide semiconductor is quite difficult because electron carriers are easily generated by oxygen vacancies.<sup>14</sup> IGZO is widely used composition for control of carrier concentration. However, indium has very high price and localized deposit area. In this thesis, indium-free ZnO semiconductor by low-temperature process and solution-process is focused.

### 2.2.1. Zinc oxide semiconductor

Various ZnO TFTs were reported by the optimization of the structure of semiconductor, condition of post annealing and control of oxygen pressure.<sup>15,16,17</sup> However, the processing temperature or post-annealing process of the semiconductor was necessary to obtain high quality of ZnO films. To achieve low-temperature process, various vacuum techniques such as sputtering, metal organic chemical vapor deposition, and atomic layer deposition are developed.<sup>18,19,20,21</sup> Although vacuum deposition methods ensure high quality of ZnO films, there are

still challenging problems; high cost, complexity of processing. In terms of continuous process such as roll-to-roll processing, solution-processed ZnO semiconductor have been focused on low-cost continuous process.

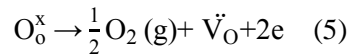
The sol-gel method which uses zinc acetate as precursors is the most widely used method for solution-processed ZnO semiconductor.<sup>22</sup> This method have critical defect that they need high annealing temperature because acetate functional group have high decomposition temperature. Because of this restriction, intensive research has been carried out on the development of precursor with low decomposition temperature.<sup>23,24</sup>

### **2.2.2. Structure and electrical properties of ZnO**

**Crystalline structure of ZnO:** As mentioned above, the advantages of ZnO over amorphous silicon are its own properties which are the higher mobility, transparency at visible region, and solution-processibility. ZnO is a group II-VI semiconductor with a wide bandgap of 3.437 eV at 2 K and have thermodynamically stable structure of wurtzite as seen in figure 1.4.<sup>25</sup> ZnO films generally have polycrystalline structure which have main peak at  $36.2^\circ$  and [101] phase with miller index. X-ray diffraction is used to investigate crystal structure and JCPDS card data of 36-1451 is used for reference data in figure 1.5. In case of very thin film such as thickness of 7 nm of ZnO, however, wide angle X-ray scattering spectroscopy should be used for measuring the precise data of d-spacing, lattice parameter, and intensity data. Ka *et al.* reported that the crystalline structure of ZnO semiconductor films from zinc ammine complex precursors, and they investigated crystalline structure with grazing incidence wide angle X-ray

scattering spectroscopy.<sup>26</sup> The polycrystalline ZnO films has mainly the orientation of growth in [101] phase.

**Electrical properties of ZnO:** Bulk mobility and carrier concentration of ZnO with temperature can be seen in figure 1.6.a and 1.6.b.<sup>27</sup> The electron carriers of ZnO are generated both intrinsically and extrinsically. Perfect single crystal materials at 0 K could not have carrier electron because all lattice sites are occupied. However, carriers could be generated intrinsically at temperature above 0 K by the thermal activation. Also, oxygen vacancies in the metal oxide semiconductor are most well known source of defect. This process can be expressed by following equation written in Kroger-Vink notation.<sup>4</sup>



The oxygen vacancy could have three states ( $\text{V}_\text{o}^0$ ,  $\text{V}_\text{o}^+$ , and  $\text{V}_\text{o}^{2+}$ ) and each ball and stick model of three states is shown in figure 1.7.a, b, and c.<sup>25</sup> Each state of oxygen vacancy has different relaxation energy around atoms and affects stereochemistry. In case of  $\text{V}_\text{o}^0$ , the four Zn atoms are relaxed inward by 12 % of the equilibrium ZnO matrix.  $\text{V}_\text{o}^+$  repels Zn atoms outward by 3 % and  $\text{V}_\text{o}^{2+}$  repels Zn atoms outward by 23 %. These oxygen vacancies induce additional electrons in ZnO semiconductor. The carrier concentration of metal oxide semiconductor is inversely proportional to the oxygen pressure during deposition or annealing process.

In addition, metal-oxygen bonds (M-O bonds) are another factor of electrical properties of ZnO semiconductor. However, the relation between M-O bonds and oxygen vacancies are not clear. For high electrical properties of ZnO semiconductor, it is require that the increment of M-O bonds in the ZnO induced by the high temperatures sintering.<sup>28</sup> The high temperature sintering is essential for

reducing of the oxygen vacancies that creates potential barrier as the electron trap sites, which hinder the free movement of electrons.<sup>29</sup> In contrast of this elucidation, the increase of oxygen vacancies also can enhance the electrical performance of devices. The low oxygen contents annealing or deposition methods could create oxygen vacancy, which creates a doubly charged oxygen vacancy ( $V_O^{2+}$ ) in the ZnO crystal structure with two free electrons.<sup>17</sup> The increment of free electrons induced by oxygen vacancies can enhance the carrier transport by enhancement of the effective density of states in the conduction band.

In the fabrication process, polycrystalline structured binary metal oxide semiconductors such as  $In_2O_3$  and ZnO are generally obtained, which leads to the existence of grain boundaries. These grain boundaries induce trapping of electron by localized state between the energy gaps. In this case, most of electrons are trapped in localized state and small amount of electrons are transported from the localized state to the conduction band by thermal energy.<sup>30</sup> As shown in figure 1.8, band tail, mobility edge, and extended states of polycrystalline semiconductor are described. The disorder from polycrystalline structure influences the mobility of the electrons and holes above the mobility edges which is the separation line of the delocalized state and the localized state. Intrinsic mobility of semiconductor is expressed as

$$\mu = \frac{q\tau}{m} = \frac{qL}{mV_{th}} \quad (6)$$

where  $\tau$  is the scattering time,  $m$  is effective mass,  $L$  is mean free path and  $V_{th}$  is the thermal velocity. Assuming the localized states under conduction band are a single exponential equation, mobility of polycrystalline (or nanocrystalline) ZnO semiconductor can be described as

$$\mu_D = \mu_0 \frac{\tau_{\text{free}}}{\tau_{\text{free}} + \tau_{\text{trap}}} = \mu_0 \frac{N_c}{N_c + N_t \exp(E_T/kT)} \approx \mu_0 \left( \frac{N_c}{N_t} \right) \exp\left(\frac{-E_T}{kT}\right) \quad (7)$$

where  $\mu_D$  is mobility of disordered semiconductor,  $\tau_{\text{free}}$  is the mean path time of conduction band transportation,  $\tau_{\text{trap}}$  is the mean path time of localized state transportation,  $N_c$  is the effective density of states in the conduction band, and  $N_t$  is the number of traps.

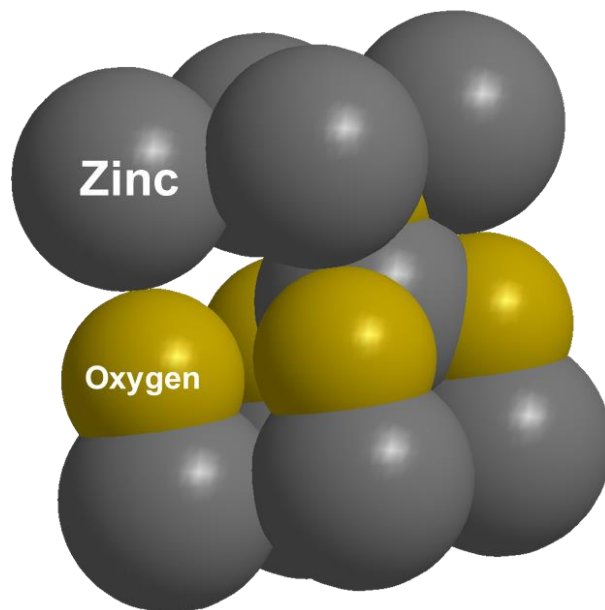


**Figure 1.4.** Schematic image of wurtzite ZnO structure.

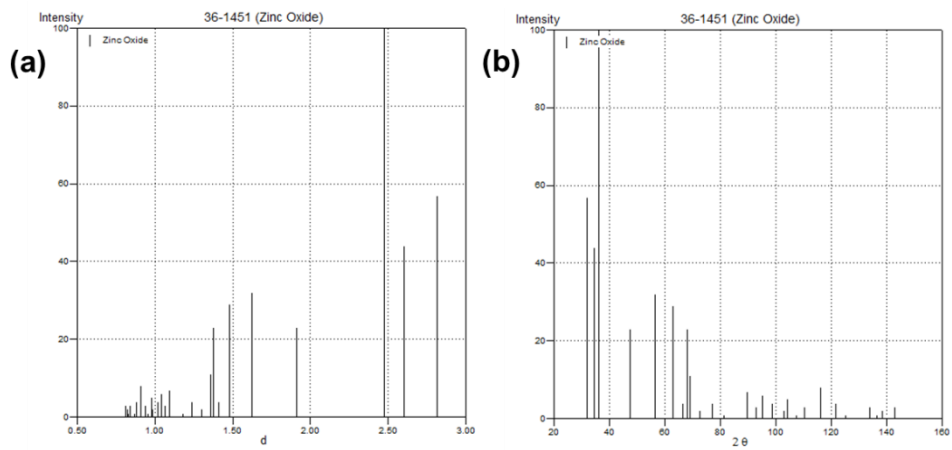


**Figure 1.5.** JCPDS card of 36-1451 data (a) x-axis is d spacing (b) x-axis is 2-theta scale.

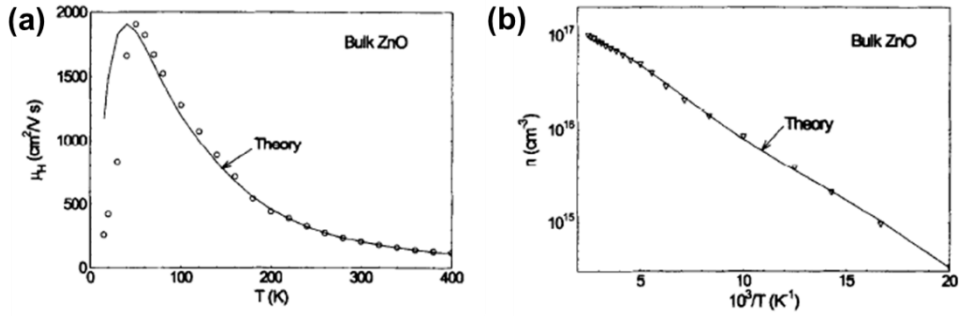


**Figure 1.6.** (a) hall mobility of bulk ZnO with respect to temperature. (b) hall carrier concentration of bulk ZnO with respect to temperature.<sup>27</sup>

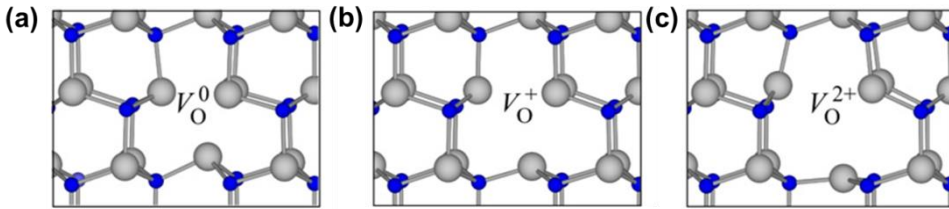


**Figure 1.7.** Ball and stick model of local atomic relaxations around the oxygen vacancy in the ZnO matrix (a) neutral state, (b) +1 charge state, (c) +2 charge state.<sup>25</sup>

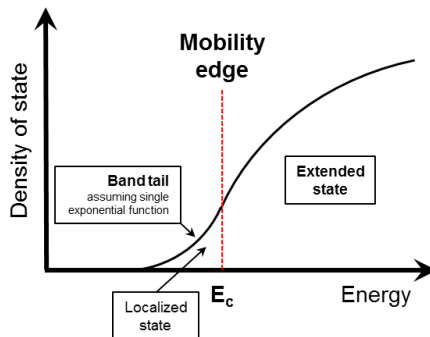


**Figure 1.8.** The density of states distribution near the band edge of a disordered semiconductor, showing the localized and extended states separated by the mobility edge.

### 2.2.3. Doping mechanism of ZnO

To compensate low electron mobility of polycrystalline (or nanocrystalline) ZnO semiconductor, doping is the most effective method. The electron mobility is defined in equation 6. In order to increase the electron mobility, the mean free path time should be increased or the effective mass should be decreased. The effective mass is decided by materials, and tau is related to film condition or donors.<sup>31</sup>

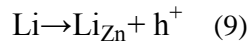
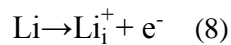
The group III elements such as B, Al, Ga and In is the most common dopants and this dopants are substituted on Zn site. The extra valence electron of the dopants is loosely bonded. As temperature rises to room temperature, this electron is excited to the conduction band and is free to transport. Especially, indium has been focused because indium doped metal oxide has high electron mobility in amorphous structure. Indium has large 5 s-orbital which is insensitive to structural deformation and forms a continuous conducting path for electron transportation. When an external electric field is applied from gate electrode, the electrons flow by the hopping through the 5 s-orbitals of indium cations. This conduction mechanism is called to percolation conduction. Although indium doped ZnO has high electron mobility in amorphous state, the cost of indium has increased rapidly, and even more problematic, indium has become increasingly scarce and strategically important.

Another doping method is the interstitial hydrogen doping. The role of hydrogen in the ZnO was recently discovered by the first-principle calculations.<sup>32</sup> Their calculations suggest  $H_i$  (hydrogen atom in interstitial site of ZnO) still acts as a shallow donor when hydrogen atoms are bonded to transition-metal impurities. Although metal oxide semiconductors are treated by extremely controlled growth

or annealing process, hydrogen is ubiquitous and can easily be incorporated.<sup>33</sup> Hydrogen doping is essential to inject of hydrogen gas for reactive diffusion, and doping process is somewhat cumbersome.

To address this issue, alkali and alkali earth metal dopants were developed for high-performance and low-temperature process TFTs. These amphoteric dopants which could act both a donor and an acceptor were reported in 1960.<sup>34</sup> The electron donor behavior occurs when lithium act as an interstitial impurity. Kolb and Laudise reported that introduction of lithium during hydro thermal growth could enhance the n-type conductivity.<sup>35</sup> In this method, post-growth heat treatment is necessary to achieve diffusing out of zinc interstitials.

In addition, Hosono *et al.* suggested the possibility of effective n-type doping in ZnO through the ion implantation of a cation that has low electron affinity.<sup>13</sup> When group I or II elements occupy the interstitial sites of ZnO matrix, they act as a shallow donor, and increase carrier concentration. Lithium in ZnO could occupy the interstitial site as well as the substitutional zinc site in the ZnO matrix. Equation (8) and (9) explain the Li defect mechanism in ZnO.<sup>36</sup>



In silicon semiconductor, increased carrier concentration does not cause enhancement of electron mobility.<sup>37</sup> The electron mobility decreased inversely by increasing carrier concentration due to impurity scattering effect.<sup>3</sup> In nanocrystalline metal oxide semiconductor, however, carrier concentration affects electron mobility because increased electron density raise probability which electron could be transport in the extended states.

The concentration of electrons in the conduction band is described as

$$n_0 = \int_{E_C}^{\infty} f(E)N(E)dE \quad (10)$$

where  $f(E)$  is Fermi-Dirac distribution and  $N(E)dE$  is the density of states in the energy range  $dE$ .<sup>3</sup> The conduction band electron concentration ( $n_0$ ) is simply the effective density of state at  $E_C$  time the probability of occupancy at  $E_C$ .

$$n_0 = N_C f(E_C) \quad (11)$$

As shown in figure 1.9.a, alkali metal exists below the conduction band minimum (CBM) and acts as a shallow donor. Carrier concentration is calculated from density of state (figure 1.9.a) and Fermi-Dirac distribution (figure 1.9.b), and increased  $N_C$  is shown in figure 1.9.c. From the definition of mobility (equation 7),  $\mu_D$  is the proportional to  $N_C$ . As a result, alkali metal exists in shallow donor state and donates an electron to ZnO matrix and increased carrier concentration enhances electron mobility.

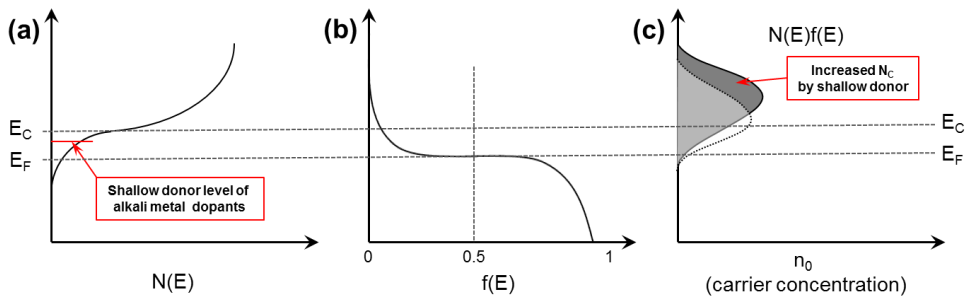


**Figure 1.9.** Schematic density of state, Fermi-Dirac distribution, and the carrier concentration for intrinsic ZnO and alkali metal doped ZnO.

## 2.2.4. Interface trap of ZnO/dielectric layer

Research of metal oxide TFTs has been focused on advancement of the device stability for applying to AMLCD or AMOLED displays.<sup>38,39,40</sup> Highly stable devices should have extremely small variation of threshold voltage ( $V_{th}$ ) and degradation in field effect mobility. It was reported that 0.1 V of threshold voltage shift causes 20 % variations of luminance of the OLED pixels and this reflects the fact that OLED is current-dependent devices.<sup>41</sup> In case of TFT-LCD, retaining of threshold voltage is necessary as much as maintaining of high mobility during prolonged operation.<sup>2</sup>

Cross *et al.* found that positive gate bias stress induces a positive shift in the transfer curve, while negative gate bias stress results in a negative shift.<sup>39</sup> These phenomena upon application of a bias stress could be caused by charge trapping at the channel/gate insulator interface or charge injection into the bulk dielectric. However, devices are recovered initial state after a relaxation (1 hour) with thermal energy of room temperature. As the thermal energy of room temperature is too small to cause charge injection into bulk dielectric layer, shift of threshold voltage could be attributed to charge trapping than charge injection.<sup>7</sup>

Kakalios *et al.* reported the exponential energy distribution of traps, and the equation is described as

$$\exp(-E/k_B T_0) \quad (12)$$

where  $k_B T_0$  is the width of the trap distribution.<sup>42</sup> They extracted trap density from amorphous silicon semiconductor and there is quantitative agreement between the stretched-exponential fitting parameters and the measured temperature. Density of

trap which means dangling bonds in amorphous silicon semiconductor are defined as

$$n_{BT} = N_{donor} - N_d \quad (13)$$

Where  $n_{BT}$  is the density of occupied state in the conduction band tail,  $N_d$  is related to the densities of trap, and  $N_{donor}$  is the carrier concentration.

Jackson established the dependence of the defect kinetics on carrier density.<sup>43</sup> Shifts of threshold voltage on capacitors were studied as a function of time, temperature, and bias. From the experiments, it was reported that shift of threshold voltage could be related to the defect density  $N_d$  and the carrier density of conduction band  $n_{BT}$ . Under bias stress test, the total charge in the semiconductor is equivalent to the charge on the gate which was induced by bias gate voltage. Equivalently,

$$\int_0^{\infty} n_{BT}(x,t)dx + \int_0^{\infty} N_d(x,t)dx = C_i(V_g - V_{th}) \quad (14)$$

where  $x$  is the distance from semiconductor/insulator interface,  $C_i$  is the capacitance of the dielectric layer,  $V_{th}$  is the initial threshold voltage. As  $n_{BT}(x,t)$  and  $N_d(x,t)$  are large only within the accumulation region, equation 14 could be approximated by

$$n_{BT}(t) + N_d(t) = \frac{C_i(V_g - V_{th})}{L_D} \approx N_i \quad (15)$$

where  $N_i$  is the induced charge density by gate bias field. Final equation (15) basically states that the change in defect density is proportional to the variation of threshold voltage. These results could be used to relate shift of threshold voltage to defect densities.<sup>43</sup> Using analytic approximation, stretched exponential model for defect creation was defined as

$$V(t) = \frac{V(0)-V(\infty)}{\left[1+\left(\frac{t}{\tau_c}\right)^\beta\right]^{1/\varepsilon}} + V(\infty) \quad (16)$$

where  $V(0)$ ,  $V(t)$ ,  $V(\infty)$  is the threshold voltage at initial state, time  $t$ , and equilibrium time.  $\beta$  is the stretched exponential exponent ( $T/T_0$ ) and  $\tau$  is the relaxation time constant. However, this model is based on MOS capacitor and the equation should be modified. Wehrspohn *et al.* reported that threshold voltage shift in amorphous silicon TFTs are characterized by the thermalization energy ( $E_{th}$ ) for different times and temperatures and fitted by modified stretched exponential equation.<sup>44</sup>

$$\Delta V_t(E_{th}) = [V_{bias} - V_t(0)] \cdot \left[ 1 - \frac{1}{\left\{ 1 + \exp\left[\frac{(E_{th} - E_A)}{k_B T_0}\right]\right\}^2} \right] \quad (17)$$

$V_{bias}$  is the voltage of bias stress,  $E_{th}$  is the thermalization energy. To a first-order approximation after a time  $t$  at a temperature  $T$ , all possible defect creation sites with  $E \ll kT \ln(vt)$  will have converted into defects. A thermalization energy can therefore be defined by

$$E_{th} = kT \ln(vt) \quad (18)$$

where  $v$  is the attempt-to-escape frequency.<sup>45</sup> In case of poly-Si TFT, frequency is  $10^5 - 10^6 \text{ s}^{-1}$ .<sup>46</sup>

## 2.3 Reference

- [1] B. G. Streetman, S. Banerjee, Solid state electronic devices, Pearson/Prentice Hall, Upper Saddle River, N.J. **2006**.
- [2] Introduction to thin film transistors, Springer, New York **2012**.
- [3] R. A. Street, Hydrogenated amorphous silicon, Cambridge University Press, Cambridge; New York **1991**.
- [4] R. M. Pasquarelli, D. S. Ginley, R. O'Hayre, Chem. Soc. Rev. **2011**, 40, 5406.
- [5] P. Barquinha, Transparent oxide electronics: from materials to devices, Wiley, Hoboken, N.J. **2012**.
- [6] C. Reese, Z. N. Bao, J. Appl. Phys. **2009**, 105, 02456.
- [7] J. S. Park, W. J. Maeng, H. S. Kim, J. S. Park, Thin Solid Films, **2012**, 520, 1679.
- [8] D. C. Cronemeyer, Phys. Rev. **1957**, 105, 522.
- [9] H. Gleskova, P. I. Hsu, Z. Xi, J. C. Sturm, Z. Suo, S. Wagner, J. Non-Cryst. Solids. **2004**, 338, 732.
- [10] S. Y. Yoon, N. Young, P. J. van der Zaag, D. McCulloch, IEEE Electr. Device. L. **2003**, 24, 22.
- [11] J. C. Bijleveld, A. P. Zoombelt, S. G. J. Mathijssen, M. M. Wienk, M. Turbiez, D. M. de Leeuw, R. A. J. Janssen, J. Am. Chem. Soc. **2009**, 131, 16616.
- [12] K. Nomura, H. Ohta, K. Ueda, T. Kamiya, M. Hirano, H. Hosono, Science. **2003**, 300, 1269.
- [13] H. Hosono, J. Non-Cryst. Solids. **2006**, 352, 851.
- [14] A. Janotti, C. G. Van de Walle, Appl. Phys. Lett. **2005**, 87.

- [15] P. Barquinha, L. Pereira, G. Goncalves, R. Martins, E. Fortunato, *Electrochem. Solid. St.* **2008**, 11, H248.
- [16] J. J. Kim, J. Y. Bak, J. H. Lee, H. S. Kim, N. W. Jang, Y. Yun, W. J. Lee, *Thin Solid Films.* **2010**, 518, 3022.
- [17] J. F. Wager, B. Yeh, R. L. Hoffman, D. A. Keszler, *Curr. Opin. Solid. St. M.* **2014**, 18, 53.
- [18] S. Masuda, K. Kitamura, Y. Okumura, S. Miyatake, H. Tabata, T. Kawai, *J Appl. Phys.* **2003**, 93, 1624.
- [19] P. F. Carcia, R. S. McLean, M. H. Reilly, G. Nunes, *Appl. Phys. Lett.* **2003**, 82, 1117.
- [20] J. Zhu, H. Chen, G. Saraf, Z. Duan, Y. Lu, S. T. Hsu, *J. Electron. Mater.* **2008**, 37, 1237.
- [21] S. J. Lim, J. M. Kim, D. Kim, S. Kwon, J. S. Park, H. Kim, *J. Electrochem. Soc.* **2010**, 157, H214.
- [22] M. Ohyama, H. Kozuka, T. Yoko, *Thin Solid Films.* **1997**, 306, 78.
- [23] K. K. Banger, Y. Yamashita, K. Mori, R. L. Peterson, T. Leedham, J. Rickard, H. Sirringhaus, *Nat. Mater.* **2011**, 10, 45.
- [24] M. G. Kim, M. G. Kanatzidis, A. Facchetti, T. J. Marks, *Nat. Mater.* **2011**, 10, 382.
- [25] A. Janotti, C. G. Van de Walle, *Rep. Prog. Phys.* **2009**, 72.
- [26] Y. Ka, E. Lee, S. Y. Park, J. Seo, D. G. Kwon, H. H. Lee, Y. Park, Y. S. Kim, C. Kim, *Org. Electron.* **2013**, 14, 100.
- [27] D. C. Look, D. C. Reynolds, J. R. Sizelove, R. L. Jones, C. W. Litton, G. Cantwell, W. C. Harsch, *Solid. State. Commun.* **1998**, 105, 399.
- [28] S. Jeong, Y. G. Ha, J. Moon, A. Facchetti, T. J. Marks, *Adv. Mater.* **2010**,

22, 1346.

- [29] H. Bong, W. H. Lee, D. Y. Lee, B. J. Kim, J. H. Cho, K. Cho, *Appl. Phys. Lett.* **2010**, 96.
- [30] E. Lee, J. Ko, K. H. Lim, K. Kim, S. Y. Park, J. M. Myoung, Y. S. Kim, *Adv. Funct. Mater.* **2014**, 24, 4689.
- [31] M. Miyao, T. Motooka, N. Natsuaki, T. Tokuyama, *Solid. State. Commun.* **1981**, 37, 605.
- [32] A. Janotti, C. G. Van de Walle, *Nat. Mater.* **2007**, 6, 44.
- [33] C. G. Van de Walle, *Phys. Rev. Lett.* **2000**, 85, 1012.
- [34] J. J. Lander, *J. Phys. Chem. Solids.* **1960**, 15, 324.
- [35] E. D. Kolb, R. A. Laudise, *J. Am. Ceram. Soc.* **1965**, 48, 342.
- [36] G. Srinivasan, R. T. R. Kumar, J. Kumar, *J. Sol-Gel. Sci. Techn.* **2007**, 43, 171.
- [37] D. A. Neamen, *Semiconductor physics and devices : basic principles*, McGraw-Hill, New York, NY **2012**.
- [38] S. Chang, Y. S. Do, J. W. Kim, B. Y. Hwang, J. Choi, B. H. Choi, Y. H. Lee, K. C. Choi, B. K. Ju, *Adv. Funct. Mater.* **2014**, 24, 3482.
- [39] R. B. M. Cross, M. M. De Souza, *Appl. Phys. Lett.* **2006**, 89.
- [40] J. H. Kim, U. K. Kim, Y. J. Chung, J. S. Jung, S. H. Ra, H. S. Jung, C. S. Hwang, J. K. Jeong, S. Y. Lee, *Appl. Phys. Lett.* **2011**, 98.
- [41] H. J. In, O. K. Kwon, *IEEE. Electr. Device. L.* **2009**, 30, 377.
- [42] J. Kakalios, R. A. Street, W. B. Jackson, *Phys. Rev. Lett.* **1987**, 59, 1037.
- [43] W. B. Jackson, *Phys. Rev. B.* **1990**, 41, 1059.
- [44] R. B. Wehrspohn, S. C. Deane, I. D. French, I. G. Gale, M. J. Powell, R. Bruggemann, *Appl. Phys. Lett.* **1999**, 74, 3374.

[45] S. C. Deane, R. B. Wehrspohn, M. J. Powell, Phys. Rev. B. **1998**, 58, 12625.

[46] R. B. Wehrspohn, M. J. Powell, S. C. Deane, I. D. French, P. R. I. Cabarrocas, Appl. Phys. Lett. **2000**, 77, 750.

## Chapter 3. Experiments

### 3.1 Materials

Preparation of ZnO solution: For low-temperature and high-performance ZnO semiconductor, zinc ammine complex is used as precursor of ZnO semiconductor. Since Meyer *et al.* reported zinc ammine hydroxo complex as ZnO precursor, three methods for preparing zinc ammine complex have been reported.<sup>1,2,3,4</sup> Other methods which use zinc hydroxide or zinc oxide powder as precursors were reported. Each preparation methods are following.

**Precipitation method:** 0.5 M zinc nitrate hexahydrate ( $\text{Zn}(\text{NO}_3)_2 \cdot 6\text{H}_2\text{O}$ , AlfaAesar, 99.9 %) was dissolved in the 15 ml of de-ionized (DI) water. Separately, 2.5 M sodium hydroxide (NaOH, Duksan Pure Chemicals Co.,Ltd.) was dissolved in the 10 ml of DI water. A sodium hydroxide solution (10 ml) is added drop by drop to the zinc nitrate solution (15 ml), while stirring at 600 rpm for 10 min. White zinc hydroxide was formed by precipitation, and the total solution and precipitates was centrifuged four times with DI water at 5000 rpm for 5 min. During all four centrifugation processes,  $\text{Na}^+$  and  $\text{NO}_3^-$  were washed away with DI-water. The final centrifuged zinc hydroxide was dissolved in 20 ml ammonium hydroxide (aq) ( $\text{NH}_4\text{OH}$ , AlfaAesar, 99.9 %).<sup>1</sup>

**Direct dissolving of  $\text{Zn}(\text{OH})_2$ :** This method is firstly reported by Song *et al.* Solutions (0.1 M) for the ZnO layer were prepared by directly dissolving zinc hydroxide ( $\text{Zn}(\text{OH})_2$ , Junsei, 98%) in an aqueous ammonia solution ( $\text{NH}_4\text{OH}$ , Alfa Aesar, 99.999%), resulting in a solution of pH 13.5. Prior to coating, the formulated solution was rigorously stirred for 12 h at room temperature and filtered through 0.2  $\mu\text{m}$  membrane filters.<sup>2</sup>

**Direct dissolving of ZnO:** Direct dissolving ZnO into ammonia water is reported by Theissmann *et al.* and our group. ZnO solution was prepared by dissolving 0.001 mole of zinc oxide (Sigma Aldrich, 99.999%) into 12 mL of ammonium hydroxide (aq) ( $\text{NH}_4\text{OH}$ , Alfa aesar, 99.9%). The as-prepared solution was refrigerated for 5 h to increase of the solubility of ZnO. As shown in figure 2.1, the pristine ZnO precursor in 12 ml of ammonia water was dissolved well, when the as-prepared solution was refrigerated for 5 hours.<sup>3,4</sup>

**Optimized concentration of zinc ammine complex precursor from ZnO:** There are previous results using zinc ammine complex for precursors.<sup>1,2,3,4</sup> However, they have the different concentration of precursors due to lack of experiments for the maximum concentration. We tested  $\text{Zn}(\text{OH})_2$  and ZnO to confirm the maximum concentration of precursors. As shown in figure 2.2,  $\text{Zn}(\text{OH})_2$  have slightly higher maximum concentration of zinc ammine precursor and we increased 0.9 mM of zinc ammine complex precursor from ZnO powder.

**Alkali metal dopants:** De-ionized water (10 mL) and alkali metal precursors (lithium hydroxide, sodium hydroxide, potassium hydroxide, or rubidium hydroxide) were added into the ZnO solution. The molar ratios between alkali metal hydroxide and ZnO were 1, 3, 5, 10, and 15 mol%.<sup>4</sup>

**Alkali earth metal dopants:** To enhance electrical properties of ZnO TFTs, 0.1 mL of  $\text{Mg}(\text{OH})_2$  and  $\text{Ca}(\text{OH})_2$  solution ( $\text{Mg}(\text{OH})_2$  powder 0.006 g in 10 mL de-ionized water and  $\text{Ca}(\text{OH})_2$  powder 0.007 g, 0.014 g in 10 ml de-ionized water) was added to the zinc oxide solution; this resulted in Mg and Ca doped ZnO solution. Because of the different solubility in water (0.0014 g/100 mL of magnesium hydroxide and 0.173 g/100 mL of calcium hydroxide at 20 °C), magnesium dopant have low doping concentration (0.002 mol%).<sup>5</sup>

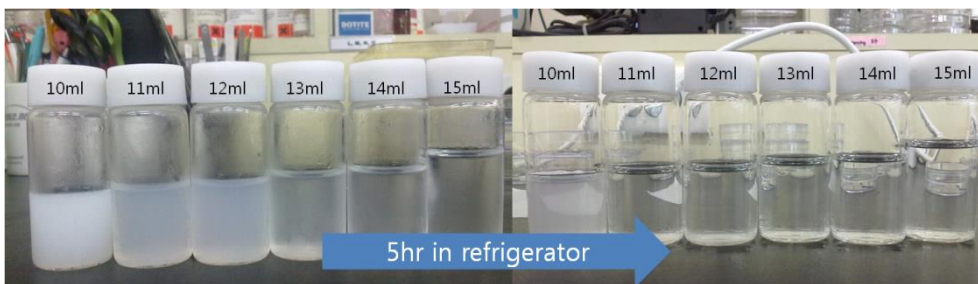
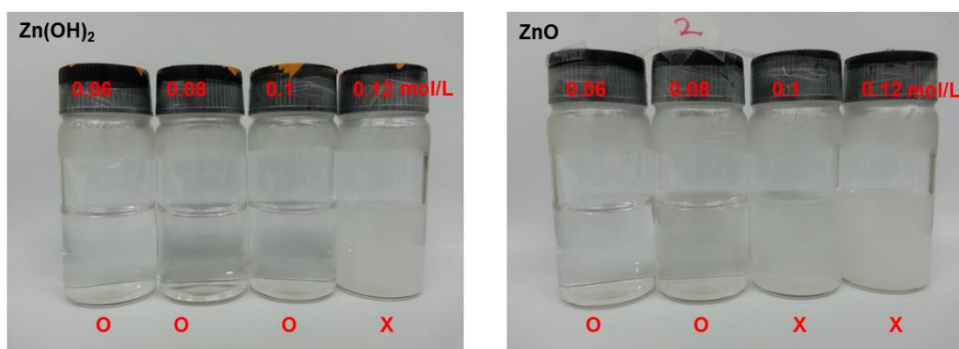


**Figure 2.1.** Photographs of pristine zinc ammine complex precursors which have various amounts of ammonia water. When the as-prepared solution was refrigerated for 5 hours, the pristine ZnO precursor in 12 ml ammonia water was dissolved well.<sup>4</sup>



Precipitated Zn(OH) <sub>2</sub> <sup>1</sup>	Intrinsic Zn(OH) <sub>2</sub> <sup>2</sup>	ZnO <sup>3</sup>	ZnO/refrigerator <sup>4</sup>
0.05~0.07 mol/L	0.1 mol/L	0.05 mol/L	0.083 mol/L

**Figure 2.2.** Photographs of zinc ammine complex precursors from intrinsic zinc hydroxide and zinc oxide. The table shows the maximum concentration of zinc ammine complex precursors.

### 3.2 Fabrication of TFTs

A heavily-doped Si wafer with a thermally grown SiO<sub>2</sub> layer (thickness 200 nm, capacitance 17 nF·cm<sup>-2</sup>) was used as the gate electrode and the gate dielectric. Prior to ZnO deposition, the Si/SiO<sub>2</sub> wafer was cleaned with detergent (Micro-90, Sigma Aldrich), acetone, and isopropyl alcohol. After depositing a layer of pristine/alkali metal doped ZnO film (annealing 300 °C on a hot plate during 1 hour), as described above, Al source/drain electrodes (100 nm) were thermally deposited through a shadow mask. The channel length (*L*) and width (*W*) were 50 and 1000 μm, respectively.

In addition, ion gel dielectric layer was embedded for low-voltage of operation.<sup>5</sup> The ion gel solution including the polystyrene-block-poly(methylmethacrylate)-block-polystyrene (PS-PMMA-PS) triblock copolymer and 1-ethyl-3-methylimidazolium bisimide(trifluoromethylsulfonyl) ([EMIM][TFSI]) ionic liquid in ethyl acetate at a 0.7:9.3:90 ratio (w/w) was drop-cast onto pristine/doped ZnO films with top contact Al source/drain electrodes. The high capacitance of the ion gel (5.17 μF·cm<sup>-2</sup> at 10 Hz) provided high on-current operation at low-voltage. Upon evaporation of ethyl acetate, an ion gel film was formed through a physical association of the PS blocks in the ionic liquid. On top of the ion gel film, an Au top gate electrode (150 nm) was deposited thermally through a shadow mask.

### 3.3 Characterization of TFTs

**Electrical measurements:** The current–voltage measurements were executed under ambient conditions by an Agilent 4155B semiconductor parameter analyzer. To exclude chemical reaction and interface diffusion of oxygen and moisture, bias

stability tests were carried out in a vacuum condition (5 mTorr).

**Thermal energy of electron hopping:** For calculation of activation energy of carrier transportation, pristine/doped ZnO TFTs on silicon substrates are measured within a temperature range of 150-290 K (-123 °C – 17 °C) using vacuum probe station (M5VC, MS TECH) and liquid nitrogen.

**Bias stress test:** A bias test was carried out in vacuum probe station to exclude the shift of the threshold voltage and field effect mobility induced by chemical reaction and interface diffusion in ZnO semiconductor with ambient oxygen and moisture. 40 or 50 V of bias voltage depending on the experiments was continuously applied for 4500–6000 seconds. Drain voltage was not applied.

### 3.4 Analysis of ZnO films

Metal oxide semiconductor in TFTs have thin films because thickness affects many parameters of TFTs such as off current, contact resistance, and field effect mobility. ZnO semiconductor layer from zinc ammine complex precursor has very thin film of 7 nm due to the low concentration of zinc source in precursor. The only problem of zinc ammine complex is the limited solubility of ZnO in ammonia water and this problem induces very thin film. As ZnO film has very thin thickness of film, X-ray diffraction could not be used. Only grazing incidence wide angle X-ray scattering (GI-WAXS) could be used to investigate the crystal structure of ZnO semiconductor from zinc ammine complex.

Cross-sectional high resolution transmission electron microscope (HR-TEM) was used for analyzing of ZnO crystal. Also, Fast Fourier Transform Selective Area Electron Diffraction (FFT-SAED) patterns are used to analyze crystal structure

with various doping concentrations.

Chemical composition of ZnO semiconductor which changes the electrical properties of semiconductor such as oxygen vacancies and metal-oxygen bonds should be investigated. X-ray photoelectron spectroscopy was carried out for investigating oxygen binding energy including oxygen vacancies.

Most of analysis tools caused degradation of metal oxide semiconductor because they require specific sample preparation procedure or secondary electrons from high energy sources. Optical analysis with UV-visible spectroscopy is the effective method for measuring electrical property using optical bandgap without damage of metal oxide semiconductor. Using tauc plot and Burstein-Moss like effect, relation between carrier concentration and optical bandgap was studied.

### **3.4.1. AFM, HR-TEM and FFT-SAED pattern**

The film morphology of the pristine/doped ZnO films was investigated by AFM (Digital instruments Nanoscope III). ZnO layer was spin-coated and etched by focused ion beam (FIB, NOVA 600, Nanolab). Sample preparation procedure of cross-sectional HR-TEM was shown in figure 2.3. For the protection of ZnO film, polymethylmethacrylate (PMMA, 10 wt% in toluene) layer was spin-coated. In FIB process, ion beam etched vertically and Si, SiO<sub>2</sub>, ZnO, PMMA, Pt layers were evaporated. In the result of etching process with FIB, cross-sectional samples could not have the perfect flat surface due to different evaporation ratio and the difference of ZnO thickness could be induced. D spacing of pristine/Li doped ZnO films were extracted from the image of HR-TEM (JEM-2100F, JEOL).

### **3.4.2. X-ray photoelectron spectroscopy**

The pristine/Li doped ZnO films were characterized by measurement of X-ray Photoemission Spectroscopy (XPS, Sigma Probe, ThermoVG). Al K $\alpha$  line was used for the source and carbon (284.5 eV) was used as the reference for calibration. The experimental results of O 1s spectra were coherently fitted by three Gaussian components, centered at 529.9 eV, 530.8 eV, and 531.8 eV, respectively.

### **3.4.3. UV-vis absorption spectroscopy**

For the optical bandgap, the transmittance of ZnO was measured by a UV-visible spectrometer (PerkinElmer, Lambda 35). For the transmittance spectra, the intrinsic ZnO film and alkali metal doped ZnO films were spin-coated on quartz substrate. The  $\alpha$  coefficient can be obtained by modified equation (19), as follows

$$\alpha = \frac{1}{D} \ln \left( \frac{1}{T} \right) \quad (19)$$

D is the film thickness which was measured from cross-sectional HR-TEM images and T is the transmittance.<sup>6</sup>

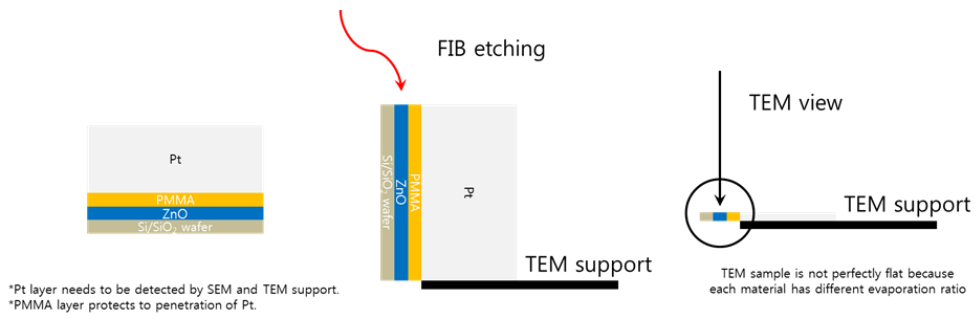


**Figure 2.3.** Schematic image of sample preparation for Cross-sectional HR-TEM.

### 3.5 Reference

- [1] S. T. Meyers, J. T. Anderson, C. M. Hung, J. Thompson, J. F. Wager, D. A. Keszler, *J. Am. Chem. Soc.* **2008**, 130, 17603.
- [2] K. Song, J. Noh, T. Jun, Y. Jung, H. Y. Kang, J. Moon, *Adv. Mater.* **2010**, 22, 4308.
- [3] R. Theissmann, S. Bubel, M. Sanlialp, C. Busch, G. Schierning, R. Schmechel, *Thin Solid Films.* **2011**, 519, 5623.
- [4] S. Y. Park, B. J. Kim, K. Kim, M. S. Kang, K. H. Lim, T. Il Lee, J. M. Myoung, H. K. Baik, J. H. Cho, Y. S. Kim, *Adv. Mater.* **2012**, 24, 834.
- [5] S. Y. Park, K. Kim, K. H. Lim, E. Lee, S. Kim, H. Kim, Y. S. Kim, *RSC Adv.* **2013**, 3, 21339.
- [6] S. W. Xue, X. T. Zu, W. L. Zhou, H. Deng, X. Xiang, L. Zhang, H. Deng, *J. Alloy. Compd.* **2008**, 448, 21.

## Chapter 4. Optimization of Zinc Ammine Complex

### Precursors for ZnO TFTs

#### 4.1 Introduction

There are the various soft-chemistry routes, most of all, sol-gel procedures were successful in the preparation of metal oxides.<sup>1</sup> As shown in figure 3.1, the sol-gel reaction of metal alkoxides involves two main reactions: hydrolysis and condensation.<sup>2</sup> During hydrolysis, oxygen of water shifts nucleophilically position of alkoxide group under release of alcohol. In condensation process, reactions between two hydroxylated metal species leads to M-O-M bonds under release of water or alcohol. In case of ZnO semiconductor preparation, the sol-gel method based on alcohol, which uses zinc acetate as precursors, is the most common method for solution-processed ZnO semiconductors; however, this method needs a high annealing temperature process. High temperature process causes serious restrictions in flexible device applications that use common plastic substrates.<sup>3</sup>

To overcome this limitation, Meyer *et al.* reported that ammine hydroxo zinc complex is a new precursor for the low-temperature annealing process.<sup>4</sup> In the fabrication of ZnO semiconductors, this precursor has several advantages: low-temperature process, high electrical performance, and solution-process. Other methods form preparing a zinc ammine complex using zinc hydroxide or zinc oxide powder as precursors for ZnO semiconductors were also reported.<sup>5,6,7</sup> Although there are several approaches for using zinc ammine complex for ZnO semiconductors, no reports compare directly the performance of the ZnO semiconductors fabricated by different zinc oxide sources. In this chapter, we characterized respectively the TFT performance of ZnO semiconductors fabricated

by the zinc ammine complex made from three different zinc oxide sources. We also analyzed the intermediate structure, oxygen vacancy, and crystal structure for ZnO semiconductors made from each of the zinc oxide sources using various instruments. In our comprehensive study, we found all the similar electrical properties in all ZnO TFTs fabricated by the three different zinc oxide sources, which were previously reported, and proved that the best way to prepare a zinc ammine complex for solution-processed ZnO semiconductor is the simple dissolution of pristine ZnO powder in ammonia water.

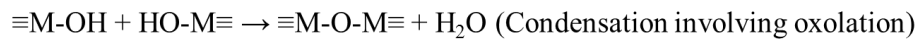
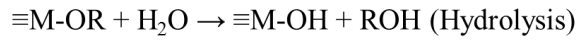


**Figure 3.1.** Main reactions in the sol-gel process using metal alkoxides.<sup>1</sup>

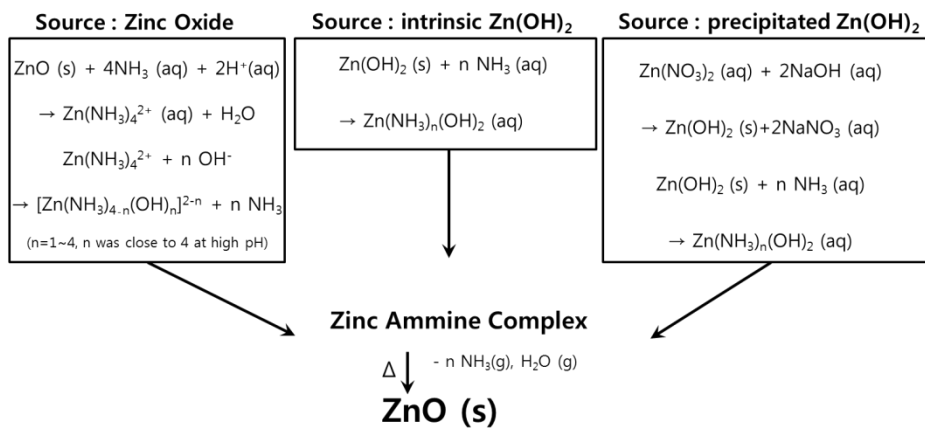
## 4.2 Results and discussion

### 4.2.1. Zinc ammine complex precursor

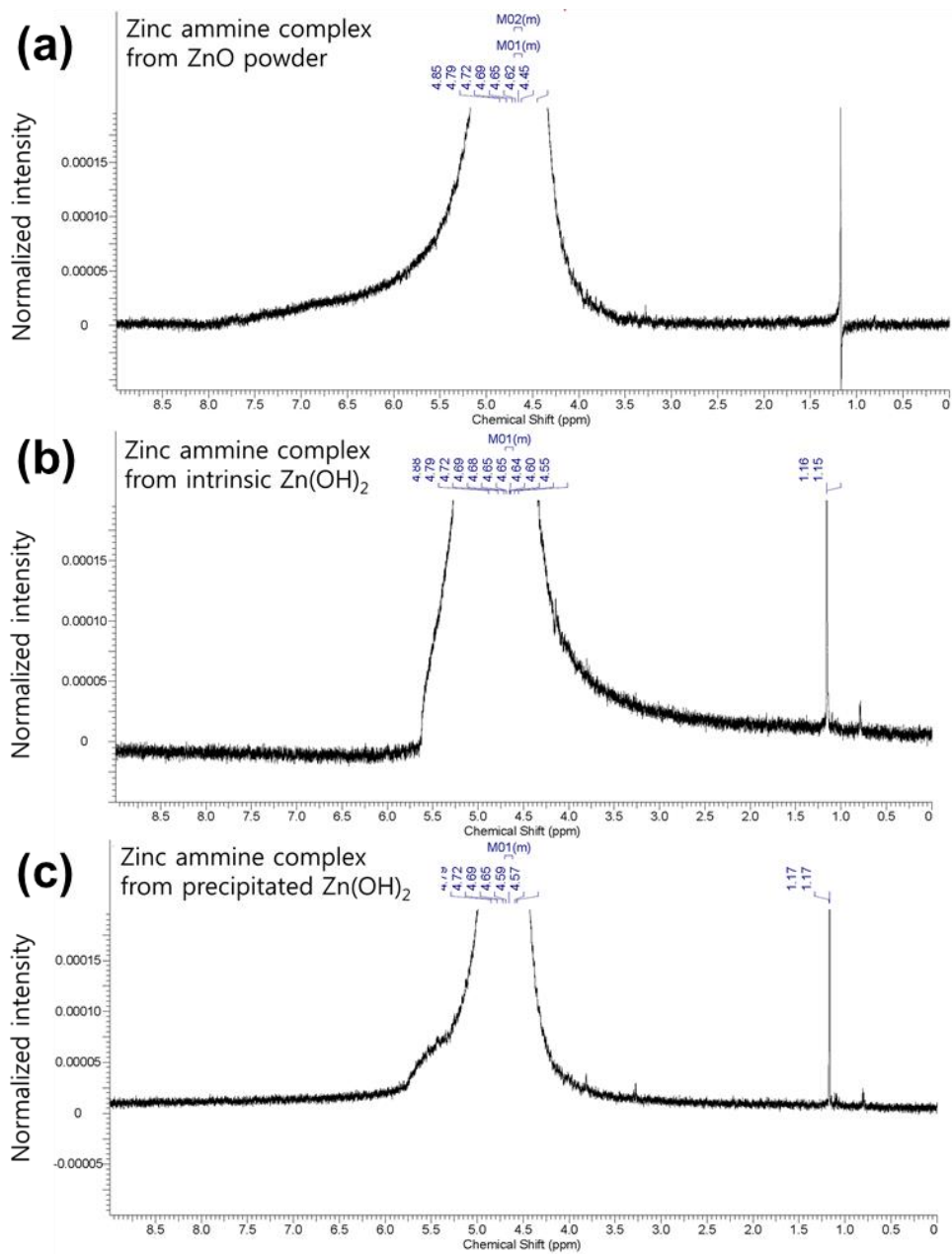
The amphoteric property of ZnO and the weak acidity of the Zn cation provide a wide range of solubility.<sup>8</sup> Meyer *et al.* first reported the dissolution of Zn salts in ammonia water for a ZnO semiconductor precursor.<sup>4</sup> Despite the good performance and process advantages, time-consuming and cumbersome processes for complex precipitation steps cause considerable deviations when preparing the precursor, which may induce large variation of the electrical performance in ZnO TFTs.<sup>6</sup> To avoid the complicated precipitation reaction, Adamopoulos *et al.* and Song *et al.* reported intrinsic zinc hydroxide as the zinc oxide source for a zinc ammine complex.<sup>5,9</sup> However, as high purity zinc hydroxide products are not commercially available, the low purity of zinc hydroxide may degrade the ZnO semiconductor performance. Consequently, zinc hydroxide still has fundamental limitations, such as the complexity of the reaction or the unknown impurity of commercial products. Hence, directly dissolving ZnO powder in to ammonia water stands out as a promising zinc oxide source for a zinc ammine complex due to its one-step fabrication process and high purity level.<sup>7,10</sup> However, there are no comprehensive studies for the structural and electrical properties of ZnO semiconductor films regarding the type of zinc oxide sources.

Figure 3.2 shows the chemical reaction of a zinc ammine complex from different zinc oxide sources.<sup>11</sup> Both zinc oxide and zinc hydroxide were transformed into a zinc ammine complex by aqueous ammonium ion. However, due to the high pH value (pH 11) of ammonia water, the zinc ammine complex was turned into an ammine-hydroxo zinc complex.<sup>12</sup> In the previous papers, zinc intermediates were

given various names, such as ammine-hydroxo zinc complex, sol precursor, or ZnO precursor solution. These unclear expressions created confusion about the intermediate.<sup>13,14</sup> We referred to the zinc ammine complex as an intermediate for escaping confusion. The intermediate is important for low-temperature thermodynamics and the rapid kinetic of transformation to ZnO semiconductors. We investigated <sup>1</sup>H-NMR spectra of various zinc ammine complexes and analyzed them using deuterium dioxide to confirm the intermediate. The <sup>1</sup>H-NMR data in figure 3.3 were obtained in ppm ( $\delta$ ) from the internal standard and chemical shift (multiplicity coupling constant in Hz, integration). The zinc ammine complex made from three zinc oxide sources showed only one peak as a singlet, as follows: ZnO powder  $\delta = 1.16$  (s, 4H): intrinsic Zn(OH)<sub>2</sub>  $\delta = 1.15$  (s, 4H): precipitated Zn(OH)<sub>2</sub>  $\delta = 1.17$  (s, 4H). We could speculate that the detected peaks around 1.16 ppm show the zinc ammine complex proton. From the analysis of the chemical reaction steps and the <sup>1</sup>H-NMR spectra, we could conclude that the same intermediate was fabricated irrespective of zinc oxide sources for the zinc ammine complex. Although the zinc ammine complex for ZnO was prepared from different zinc oxide sources, it had the same ZnO intermediate in the chemical reaction. With these results, we could expect that the ZnO semiconductors fabricated from the zinc ammine complex show a similar performance irrespective of the different zinc oxide sources.



**Figure 3.2.** Reaction mechanism of ZnO made from a zinc ammine complex prepared with various zinc oxide sources: ZnO powder, intrinsic Zn(OH)<sub>2</sub>, precipitated Zn(OH)<sub>2</sub>.



**Figure 3.3.** <sup>1</sup>H-NMR spectra of zinc ammine complex with various zinc oxide sources. The <sup>1</sup>H-NMR data were obtained in ppm ( $\delta$ ) from the internal standard and chemical shift. (a) ZnO powder, (b) intrinsic Zn(OH)<sub>2</sub>, (c) precipitated Zn(OH)<sub>2</sub>.<sup>11</sup>

### 4.2.2. TFT performances with different ZnO sources

<sup>1</sup>H-NMR data proved our speculation that the same chemical intermediate is formed from three different zinc sources. To investigate our speculation specifically, we fabricated bottom gate top contact type of ZnO TFTs. In figure 3.4, devices 1, 2, and 3 represent TFTs including the ZnO film fabricated with the zinc ammine complex prepared with ZnO powder, intrinsic Zn(OH)<sub>2</sub>, and precipitated Zn(OH)<sub>2</sub>, respectively. Figure 3.4.a, b, and c shows the transfer curves of the ZnO TFTs which were fabricated with three zinc oxide sources, respectively. The field effect mobility was derived from the transfer curve at the saturation region. Device 1, 2, and 3 exhibited the average field effect mobility of 2.9 cm<sup>2</sup>/V·s, 2.5 cm<sup>2</sup>/V·s, and 2.6 cm<sup>2</sup>/V·s, respectively. The other electrical properties of the ZnO TFTs prepared using three zinc oxide sources are shown in figure 3.4.e. The output curves of all the ZnO TFTs show n-type behavior irrespective of zinc oxide source in figure 3.5. All of ZnO TFTs shows clear saturation region at high drain current. Considering the histogram data of the ZnO TFTs in figure 3.5.d, these results reveal that similar electrical properties were obtained. In addition, Figure 3.6 shows that the hysteresis of the current between the forward and backward gate voltage sweep was negligible. The hysteresis experiments were carried out in the vacuum probe station in 5 mtorr. A bias stress test (40 V, 6000 s) was also carried out and the curves of  $\Delta V_{th}$  vs. the bias time are shown in figure 3.7. All data show the analogous electrical properties.

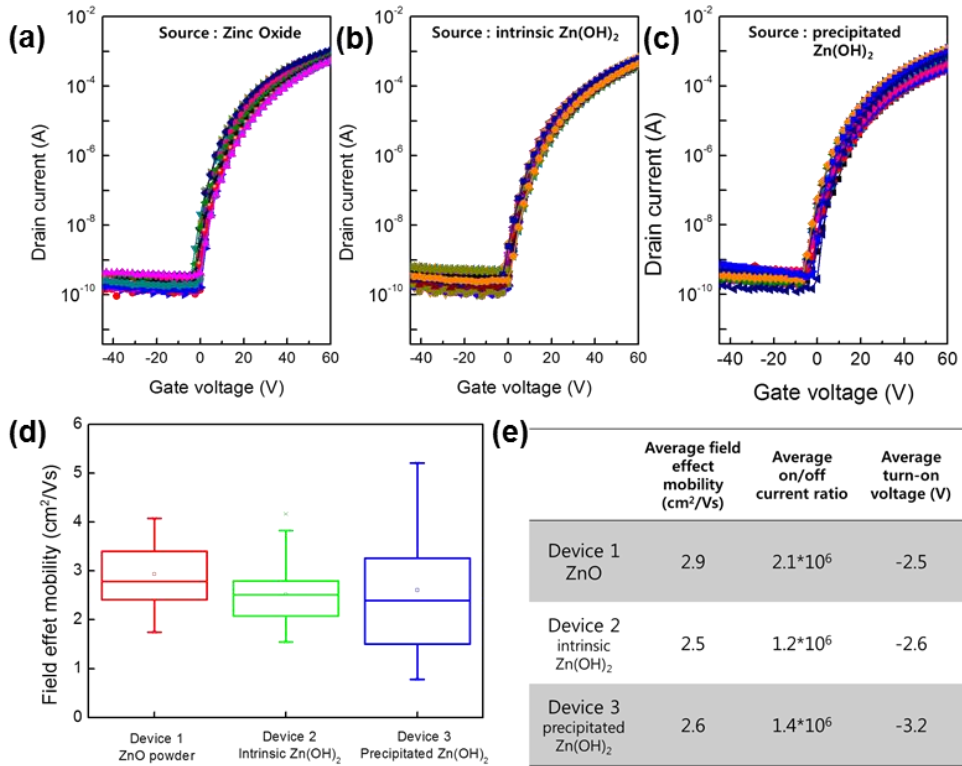


**Figure 3.4.** (a), (b), and (c) transfer curves of ZnO TFTs made from a zinc ammine complex prepared with ZnO powder, intrinsic  $Zn(OH)_2$ , and precipitated  $Zn(OH)_2$ , respectively. (d) average field effect mobility of various ZnO TFTs. (e) table of the electrical properties of various ZnO TFTs.

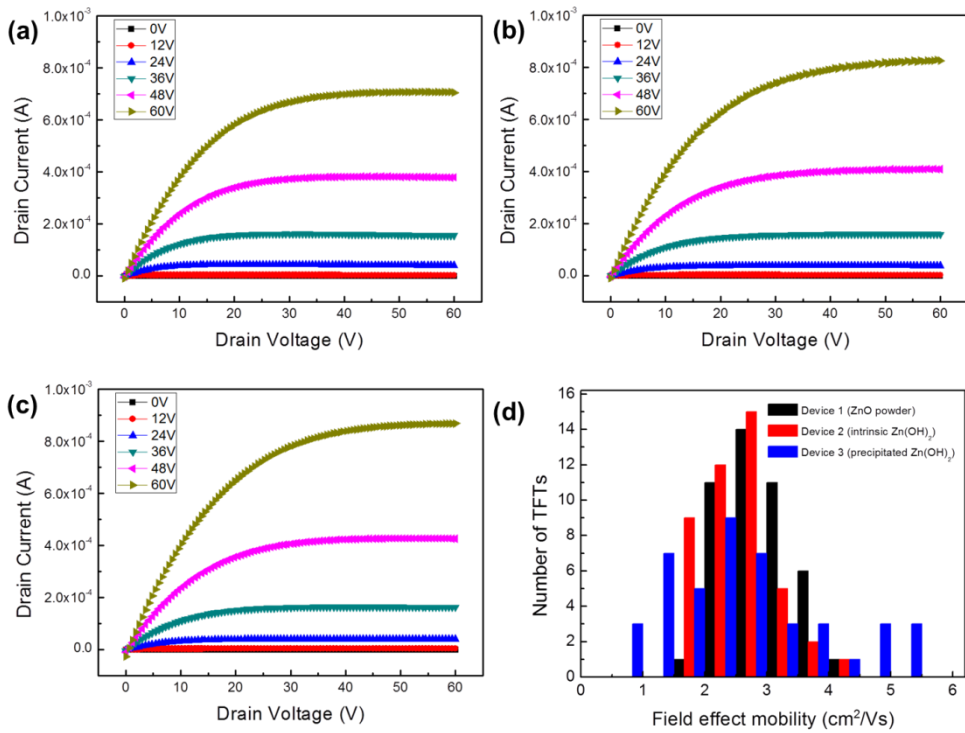


**Figure 3.5.** Output characteristic of various ZnO TFTs and the histogram of of field effect mobility of various ZnO TFTs as one run at 300 °C. (a) device 1 (ZnO powder), (b) device 2 (intrinsic  $\text{Zn(OH)}_2$ ), (c) device 3 (precipitated  $\text{Zn(OH)}_2$ ) (d) histogram data of various ZnO TFTs.

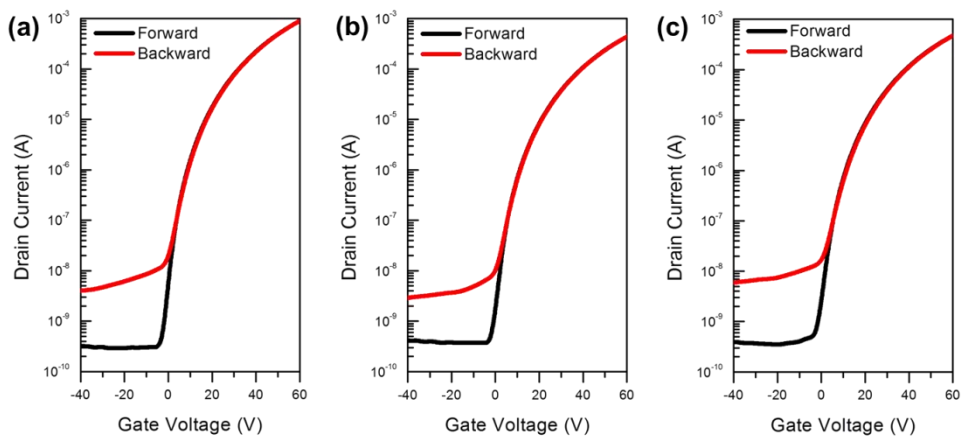


**Figure 3.6.** The hysteresis behavior of various ZnO TFTs with SiO<sub>2</sub> gate dielectric. (a) device 1 (ZnO powder), (b) device 2 (intrinsic Zn(OH)<sub>2</sub>), (c) device 3 (precipitated Zn(OH)<sub>2</sub>).

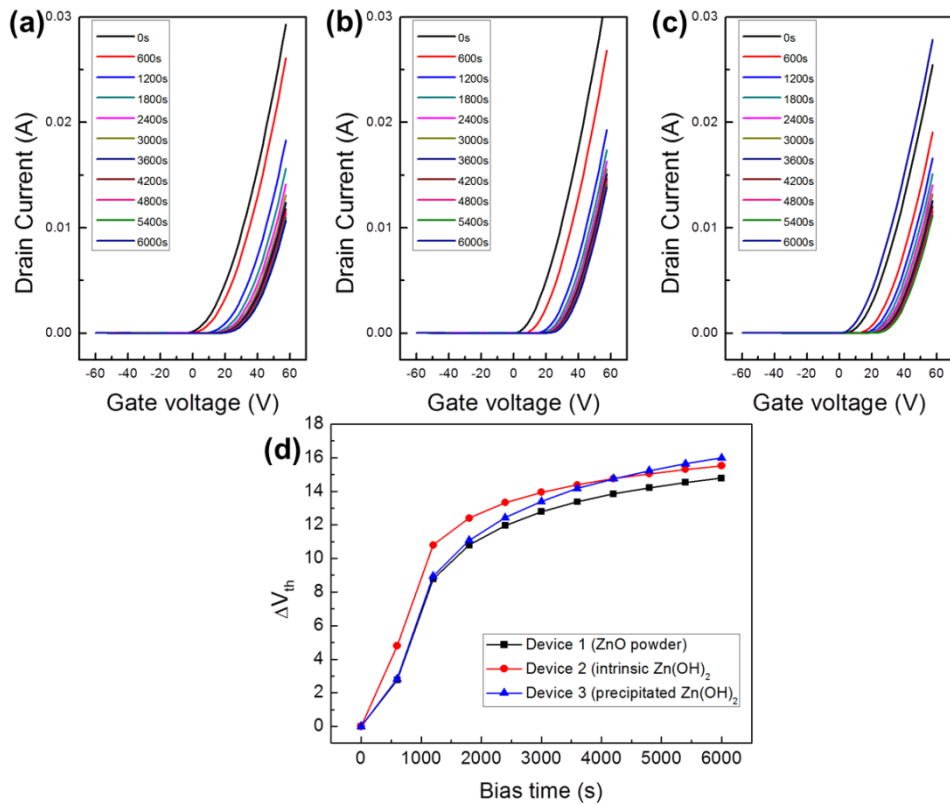


**Figure 3.7.** (a), (b), and (c) evolution of the linear transfer curves of various ZnO TFTs, as a function of positive bias stress time (40 V, 0–6000 s), (d) relative threshold voltage shift ( $\Delta V_{th}$ ) of various ZnO TFTs as a function of stress time.

### **4.2.3. Structural, morphological, and chemical analysis of ZnO films**

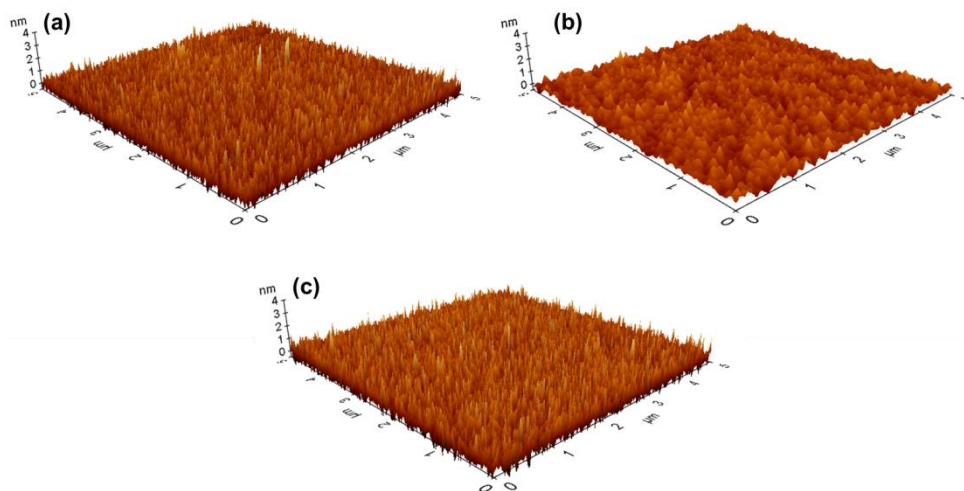
From the analogous data of  $^1\text{H-NMR}$  and the electrical properties of ZnO TFTs, the same chemical intermediate is formatted irrespective of the three different zinc oxide sources and induces electrical properties of the all ZnO TFTs. In this study, the three approaches used for fabricating a zinc ammine complex had the same chemical intermediates and showed a similar performance. However, the large deviation of mobility of device 3 was founded and this variation of devices was caused by the limitation of the precipitation method. In precipitated  $\text{Zn(OH)}_2$  for device 3, during the complex reaction process, each process could cause contamination resulting in considerable deviation in the step-by-step process. The complex and time-consuming processes for synthesis, precipitation, and removing residuals of precipitated  $\text{Zn(OH)}_2$ , also made it difficult to maintain the uniformity of the process. The complexity may be the limitation of a zinc ammine complex made with precipitated  $\text{Zn(OH)}_2$ .

Figure 3.8.a, b and c shows the AFM images of the ZnO thin films in devices 1, 2 and 3. The root mean square (RMS) roughness of the ZnO thin film in devices 1, 2, and 3 were 0.387 nm, 0.326 nm, and 0.439 nm, respectively. As the change of the surface morphology in the ZnO films were too small, any strong correlating was not detected with the field effect mobility.<sup>15</sup> In addition to surface morphology, the crystallinity of ZnO semiconductor also affects the electron transport in the active layer. With regard to binary oxides such as ZnO, they are easily transformed into a polycrystalline structure during a low-temperature annealing process. The electron transport mechanism of polycrystalline semiconductors is dominant to the grain

boundary effect. Since the hopping of electrons is hindered by the grain boundary, which acts as an energy barrier, the grain boundary scattering limits the carrier transport and reduces electron mobility.<sup>16</sup> Figure 3.9.a, b, and c show the high resolution transmission electron microscope (HR-TEM) images of the crystal structure and grain boundary. The nano-crystalline structure of the ZnO semiconductors was observed and thickness of ZnO films was 8 nm, irrespective of zinc oxide source. Figure 3.10 shows the fast Fourier transform selected area electron diffraction (FFT-SAED) patterns of each of the ZnO films. We could not observe any remarkable differences, such as lattice distortions or migrations in the all ZnO films based on different zinc oxide sources for the zinc ammine complex. Faint scattering was induced by the amorphous dielectric layer. These results revealed that the crystal structures, boundary, and morphology of ZnO films were similar irrespective of the type of zinc oxide sources.

Also, the analysis of chemical composition, such as oxygen vacancy and zinc oxide bonding, has been conducted to investigate the conduction mechanism of ZnO semiconductors.<sup>17</sup> As mentioned in chapter 2.2.2, oxygen vacancies could be the major source of the free electron carriers. The metal oxide semiconductors which have disordered structures such as polycrystalline or nanocrystalline structures show the field effect mobility depend on a carrier concentration. For this reason, we carried out x-ray photoelectron spectroscopy (XPS) and analyzed O 1s spectra in XPS. As shown in Figure 3.11.a, b, and c, the experimental O 1s peak of each device was coherently fitted by three Gaussian components, centered at 529.9 eV ( $O_A$ ), 530.8 eV ( $O_B$ ), and 531.8 eV ( $O_C$ ), respectively. The peak at 529.9 eV could be assigned to an oxygen ion in the ZnO lattices ( $O_A$ ), and the peak at 530.8 eV denoted the oxygen vacancies in the ZnO lattices ( $O_B$ ). The peak at 531.8 eV

(O<sub>C</sub>) could be assigned to the oxygen in hydroxide (-OH), which includes the absorbed oxygen on the surface of the ZnO films as -CO<sub>3</sub>, H<sub>2</sub>O, and O<sub>2</sub>.<sup>18,19</sup> In general, a good ZnO semiconductor shows a proper ratio between oxygen deficiency and metal oxide lattice (or ZnO bonding). Although there are the arguments that optimized ratio of M-O bonding and oxygen vacancy, the variation of ratio of each ZnO films from three different zinc sources gives a enough information of the uniformity of ZnO semiconductor quality.<sup>20</sup> In our analyses, the ratio of integrated area oxygen vacancy and total area in the various ZnO semiconductor films was analogous (Figure 3d).<sup>21</sup> We speculated that the same chemical intermediate was formed irrespective of the type of zinc oxide sources and the ZnO semiconductor made from the same chemical intermediate showed the analogous ratio of oxygen vacancy. Consequently, no difference was found in the performance of the solution-processed ZnO TFTs using the zinc ammine complex based on various zinc oxide sources. To avoid a time-consuming process, a large deviation of mobility, or the limitation of impurity, it is optimal to fabricate a zinc ammine complex for solution-processed ZnO TFTs by directly dissolving pure ZnO into ammonia water.



**Figure 3.8.** AFM images of various ZnO films made from a zinc ammine complex prepared with various zinc oxide sources (ZnO powder, intrinsic Zn(OH)<sub>2</sub>, and precipitated Zn(OH)<sub>2</sub>) on the SiO<sub>2</sub> substrate at the annealing temperature of 300 °C. (a), (b), and (c) AFM image of various ZnO films.

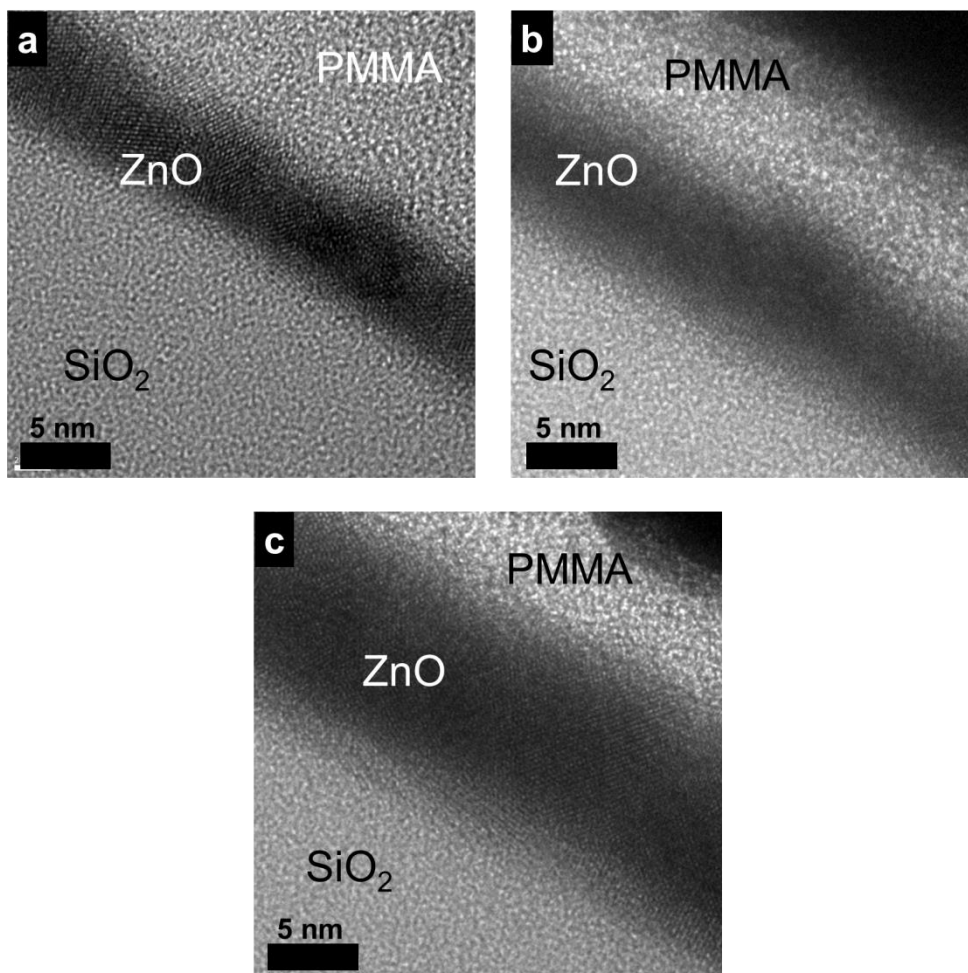


**Figure 3.9.** Cross-sectional HR-TEM images of various ZnO films made from a zinc ammine complex prepared with various zinc oxide sources (ZnO powder, intrinsic Zn(OH)<sub>2</sub>, and precipitated Zn(OH)<sub>2</sub>) on the SiO<sub>2</sub> substrate at the annealing temperature of 300 °C. (a), (b), and (c) HR-TEM image of various ZnO films.

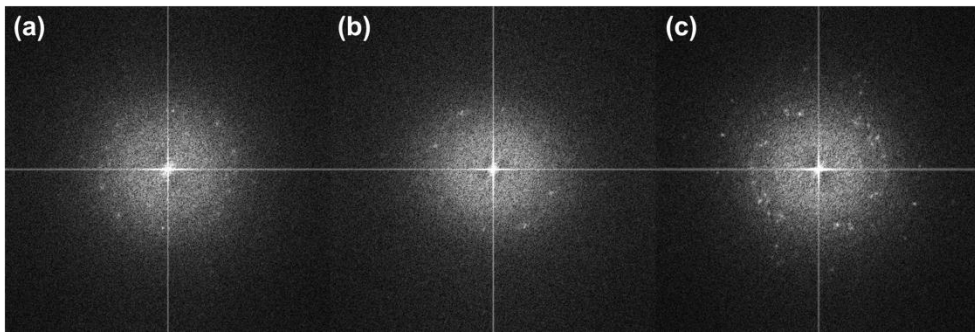


**Figure 3.10.** Images of FFT-SAED patterns of various ZnO films made from zinc ammine complex prepared with various zinc oxide sources (ZnO powder, intrinsic Zn(OH)<sub>2</sub> and precipitated Zn(OH)<sub>2</sub>) by HR-TEM. (a) ZnO powder, (b) intrinsic Zn(OH)<sub>2</sub>, (c) precipitated Zn(OH)<sub>2</sub>.

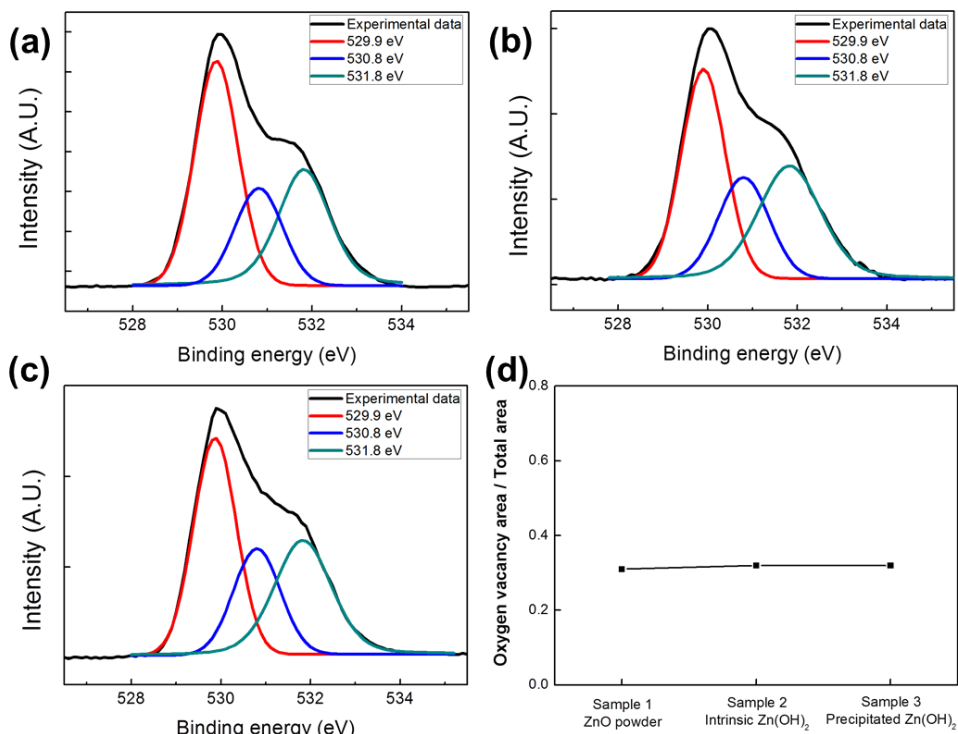


**Figure 3.11.** The O 1s XPS spectrum of various ZnO films made from a zinc ammine complex prepared with various zinc oxide sources, (a) ZnO, (b) intrinsic Zn(OH)<sub>2</sub>, (c) precipitated Zn(OH)<sub>2</sub>. (d) the ratio of integrated area oxygen vacancy and total area in the various ZnO semiconductor films

### 4.3 Reference

- [1] J. N. Hay, H. M. Raval, Chem. Mater. **2001**, 13, 3396.
- [2] M. Niederberger, N. Pinna, Metal oxide nanoparticles in organic solvents : synthesis, formation, assembly and application, Springer, Heidelberg ; New York **2009**.
- [3] V. Zardetto, T. M. Brown, A. Reale, A. Di Carlo, J. Polym. Sci. Pol. Phys. **2011**, 49, 638.
- [4] S. T. Meyers, J. T. Anderson, C. M. Hung, J. Thompson, J. F. Wager, D. A. Keszler, J. Am. Chem. Soc. **2008**, 130, 17603.
- [5] K. Song, J. Noh, T. Jun, Y. Jung, H. Y. Kang, J. Moon, Adv. Mater. **2010**, 22, 4308.
- [6] R. Theissmann, S. Bubel, M. Sanlialp, C. Busch, G. Schierning, R. Schmechel, Thin Solid Films. **2011**, 519, 5623.
- [7] S. Y. Park, B. J. Kim, K. Kim, M. S. Kang, K. H. Lim, T. Il Lee, J. M. Myoung, H. K. Baik, J. H. Cho, Y. S. Kim, Adv. Mater. **2012**, 24, 834.
- [8] J. J. Richardson, F. F. Lange, Cryst. Growth. Des. **2009**, 9, 2576.
- [9] Y. H. Lin, H. Faber, K. Zhao, Q. X. Wang, A. Amassian, M. McLachlan, T. D. Anthopoulos, Adv. Mater. **2013**, 25, 4689.
- [10] S. H. Yu, B. J. Kim, M. S. Kang, S. H. Kim, J. H. Han, J. Y. Lee, J. H. Cho, Acs. Appl. Mater. Inter. **2013**, 5, 9765.
- [11] S. Y. Park, S. Kim, J. Yoo, K. H. Lim, E. Lee, K. Kim, J. Kim, Y. S. Kim, RSC Adv. **2014**, 4, 11295.
- [12] B. Zhao, C. L. Wang, Y. W. Chen, H. L. Chen, Mater. Chem. Phys. **2010**, 121, 1.

- [13] Y. Ka, E. Lee, S. Y. Park, J. Seo, D. G. Kwon, H. H. Lee, Y. Park, Y. S. Kim, C. Kim, *Org. Electron.* **2013**, 14, 100.
- [14] K. Seong, K. Kim, S. Y. Park, Y. S. Kim, *Chem. Commun.* **2013**, 49, 2783.
- [15] G. Adamopoulos, A. Bashir, S. Thomas, W. P. Gillin, S. Georgakopoulos, M. Shkunov, M. A. Baklar, N. Stingelin, R. C. Maher, L. F. Cohen, D. D. C. Bradley, T. D. Anthopoulos, *Adv. Mater.* **2010**, 22, 4764.
- [16] K. Ellmer, *J. Phys. D. Appl. Phys.* **2001**, 34, 3097.
- [17] K. H. Lim, K. Kim, S. Kim, S. Y. Park, H. Kim, Y. S. Kim, *Adv. Mater.* **2013**, 25, 2994.
- [18] P. T. Hsieh, Y. C. Chen, K. S. Kao, C. M. Wang, *Appl. Phys. a-Mater.* **2008**, 90, 317.
- [19] Y. S. Kim, W. P. Tai, S. J. Shu, *Thin Solid Films.* **2005**, 491, 153.
- [20] K. Kim, S. Y. Park, K. H. Lim, C. Shin, J. M. Myoung, Y. S. Kim, *J. Mater. Chem.* **2012**, 22, 23120.
- [21] S. Jeong, Y. G. Ha, J. Moon, A. Facchetti, T. J. Marks, *Adv. Mater.* **2010**, 22, 1346.

# Chapter 5. Alkali metal dopants for high-performance and low-temperature ZnO TFTs

## 5.1 Introduction

Arrays of thin film transistors (TFTs) in next generation displays not only require semiconductors with high-performance, but also require them to feature high optical transparency, and low-temperature and solution-processability.<sup>1</sup> Hydrogenated amorphous silicon (a-Si:H) based TFTs have been used widely as the pixel switches in displays which is labeled as active matrix display.<sup>2,3</sup> However, amorphous silicon has relatively low electron mobility (about  $1 \text{ cm}^2/\text{V}\cdot\text{s}$ ) and its deposition requires a high-cost vacuum process. More importantly, the poor transparency of silicon makes it unsuitable for transparent applications because the transparency is one of the key issues for future display technology.<sup>4</sup> In a search for alternatives for amorphous silicon, considerable interests has focused on metal oxide semiconductors, such as In, Ga, or Zn oxides, as these exhibit high optical transparencies, and have excellent electrical properties with high electron mobility, chemical stability, and solution-processability.<sup>5</sup> For example, ZnO based semiconductors have been successfully incorporated into various electronic devices, such as electron transfer layers for solar cells, transparent electrodes, energy harvesting devices with piezoelectric properties, and channel materials for TFTs.<sup>6,7,8,9</sup> As the electron transporting layer of TFTs, ZnO semiconductors have been deposited by various techniques, such as radio frequency magnetron sputtering, chemical vapor deposition, and spin-coating followed by a post-annealing process.<sup>10,11,12</sup> Although the sputtering and vapor deposition methods have ensured high semiconducting properties and reliability, they are both costly

and the processing is cumbersome.<sup>13</sup> On the other hand, solution-processing of ZnO allows large-area and low-price manufacturing but compromises the resulting relatively low electron mobility.<sup>14</sup>

Various metal oxides including zinc cation, such as indium zinc oxide (IZO) and indium gallium zinc oxide (IGZO), which have good solution-processability at relatively low-temperatures, have been applied to compensate for the poor electrical performance of pure ZnO.<sup>4,15,16</sup> In spite of their good performance, there remains a significant challenge to the use of IZO or IGZO in electronic devices, due to the supply shortage of indium. The cost of indium has increased rapidly to the level of a silver price, and even more problematic, indium has become increasingly scarce and thus strategically important. The use of various dopants has been attempted to create an indium-free ZnO-based semiconductor, however, because these methods were based on a sol-gel process with hydrocarbon functional groups, they all suffered from residual carbon impurities which hamper electron transfer.<sup>17,18,19</sup> In order to remove the impurities, the only possibility is annealing at high temperatures, at least 400 °C, and this restricts the substrate to being a rigid one.<sup>20</sup> Thus, to find an alternative route to improve the carrier mobility of solution-processed ZnO under the conditions of being indium-free, carbon-free, and processed at a low-temperature is critical. Meyer *et al.* reported previously on a carbon-free method with low-temperature processability and compatibility with mechanically flexible substrates.<sup>21</sup> However, the intrinsic electron mobility of ZnO as described in this study is inadequate for use in high quality displays.

To address this issue, we employed alkali metal dopants, focusing particularly on lithium and sodium, in order to fabricate solution-processed ZnO TFTs with

enhanced the field effect mobility. In addition, we introduced unique aqueous zinc ammine complexes ( $\text{Zn}(\text{NH}_3)_4^{2+}$ ) with alkali metal hydroxides into the ZnO semiconductor synthesis, which made possible the successful creation of carbon-free ZnO thin films as the active layer of TFT at a maximum process temperature as low as 300 °C.<sup>22</sup>

## 5.2 Results and discussion

### 5.2.1. Alkali metal doped ZnO TFTs

The alkali metal doped ZnO thin films were prepared from mixtures of a zinc ammine complex and different alkali metal hydroxides. Different molar ratios (1, 3, 5, 10, and 15 mol%) of alkali metal hydroxides, such as lithium hydroxide, sodium hydroxide, potassium hydroxide, and rubidium hydroxide, were added to the zinc ammine complex. The as-prepared solution mixtures were then spin-coated onto silicon wafers ( $\text{SiO}_2/\text{Si}$ ) and were annealed at 300 °C. By annealing at such a temperature, the zinc ammine complex transformed easily into ZnO and volatile ammonia, and thus ZnO films, which were inherently free from carbon impurities, were formed at a relatively low process temperature, in a manner that is adaptable for plastic electronics.<sup>23,24</sup> The thickness of a typical ZnO film was around 7 nm. It is to be noted that no significant changes in the film morphology were observed, as was confirmed with atomic force microscopy (AFM) in the images of figure 4.1.

Figure 4.2.a shows typical transfer curves of Li doped ZnO TFTs with different Li concentrations, all of which showed typical n-type semiconductor behavior. Interestingly, a steady increase in drain current at a fixed gate voltage was observed upon applying lithium dopant into ZnO films up to 10 mol%. This demonstrates

that Li doping improves electron transport through ZnO. However, introducing a greater amount of Li resulted in a decrease in drain current, which implies that Li doping of ZnO beyond 10 mol% actually hampers electron transport. For example, drain current at a gate voltage of 60 V increased by four times upon the initial addition of Li (0–10 mol%) and then decreased upon more being added (15 mol%). Such a decrease in current may be caused by creation of charge trap site when a significant amount of dopants were added to a ZnO film. Details of Li doping at high weight fractions will be discussed in chapter 6. Similarly, the field effect mobility of the Li doped ZnO TFTs increased gradually from 1.6 to 7.3 cm<sup>2</sup>/V·s upon the initial addition of Li (0–10 mol%) but then decreased to 2.7 cm<sup>2</sup>/V·s (15 mol%) when too much Li was added. These results are summarized in figure 4.2.b.

The influence of doping on device performance was examined for other alkali metal dopants such as Na, K, and Rb. Na doped ZnO TFTs also show the analogous tendency of increase of field effect mobility, followed by a decrease in field effect mobility. The highest mobility of Li, Na, K, and Rb doped ZnO TFTs were 7.3 (10 mol% Li), 5.9 (1 mol% Na), 3.7 (3 mol% K), and 4.3 (1 mol% Rb) cm<sup>2</sup>/V·s, respectively. Figure 5.2.c displays the transfer curves of the different alkali metal doped ZnO TFTs, each with the optimum doping concentration that yielded the highest field effect mobility. The main parameters of alkali metal doped ZnO TFTs were summarized in table 1. All ZnO TFTs with alkali metal dopants showed classical behavior of n-type semiconductor in figure 4.3 and clear saturation of drain current.

As shown in figure 4.4.a, the Li doped ZnO TFTs showed excellent device operational stability during 40 continuous operations, and no obvious changes were observed in the transfer characteristics, the field effect mobility, the turn on voltage,

and the on/off current ratio during repeated operations. A negligible hysteresis data in figure 4.5.c, d, e is shown in the transfer characteristics of alkali metal doped ZnO transistors. All stability issues of Li doped ZnO TFTs were tested in vacuum prove station at 5 mtorr. For calculating accurate field effect mobility in saturation region, higher drain voltage was applied ( $V_D = 60$  V), and the field effect mobility increased up to  $11.45 \text{ cm}^2/\text{V}\cdot\text{s}$  (figure 4.5.a).

The perfectness of the crystals of the ZnO film requires atomic diffusivity at high temperature above  $500 \text{ }^\circ\text{C}$ . In our process, low-temperature ( $300 \text{ }^\circ\text{C}$ ) has the advantage of low-temperature process which enables plastic substrate, but crystalline structure is not perfect due to lack of thermal energy. We need to investigate improvement of the performance of the alkali metal doped ZnO TFTs with at higher temperatures. When alkali metal doped ZnO semiconductors were annealed at a higher temperature ( $500 \text{ }^\circ\text{C}$ ), these TFTs showed enhanced the field effect mobility. The results of high annealing temperature process are shown in figure 4.5.b and table 2. However, we focused on the lower temperature process because of the potential for application to flexible devices when based on a plastic substrate.

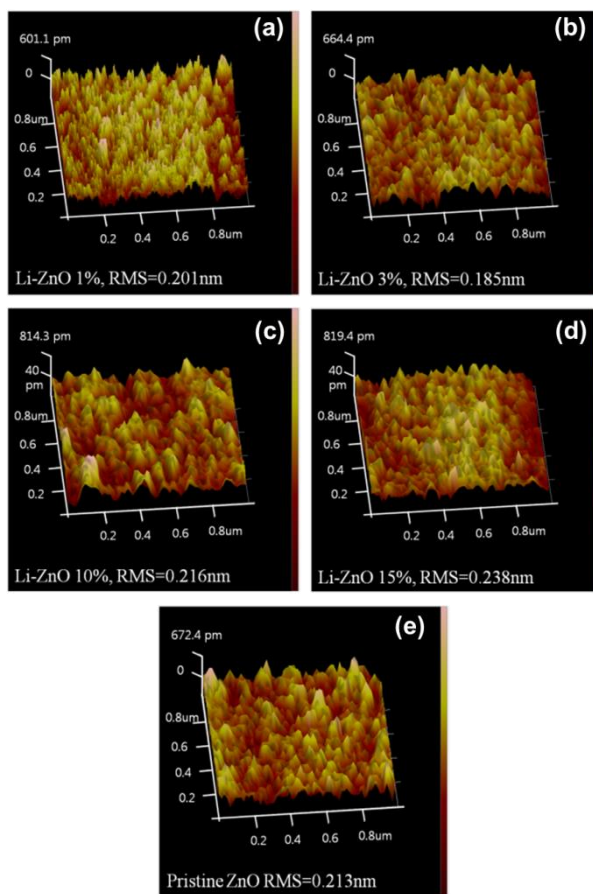


**Figure 4.1.** AFM images of ZnO films. Root mean square roughness of ZnO films were 0.20 nm (Li 1 mol%) , 0.19 nm (Li 3 mol%), 0.22 nm (Li 10 mol%), 0.24 nm (Li 15 mol%), and 0.21 nm (pristine ZnO).

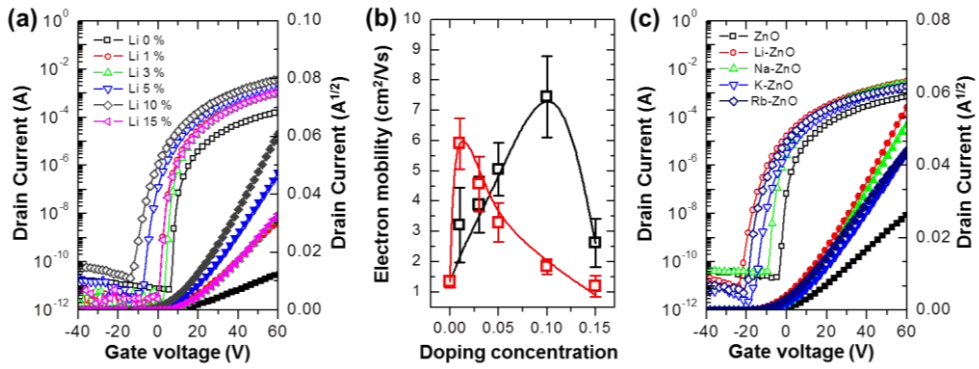


**Figure 4.2.** Electrical characteristics of pristine/doped ZnO TFTs with SiO<sub>2</sub> gate dielectric. The channel length and width were 50 and 1000  $\mu\text{m}$ , respectively. (a) transfer characteristics of Li doped ZnO TFTs with different doping concentrations ( $V_D = 40$  V). (b) field effect mobility of Li and Na doped ZnO TFTs as a function of doping concentration. (c) transfer characteristics of the ZnO TFTs based on ZnO doped with various alkali metals (10 mol% Li, 1 mol% Na, 3 mol% K, and 1 mol% Rb).

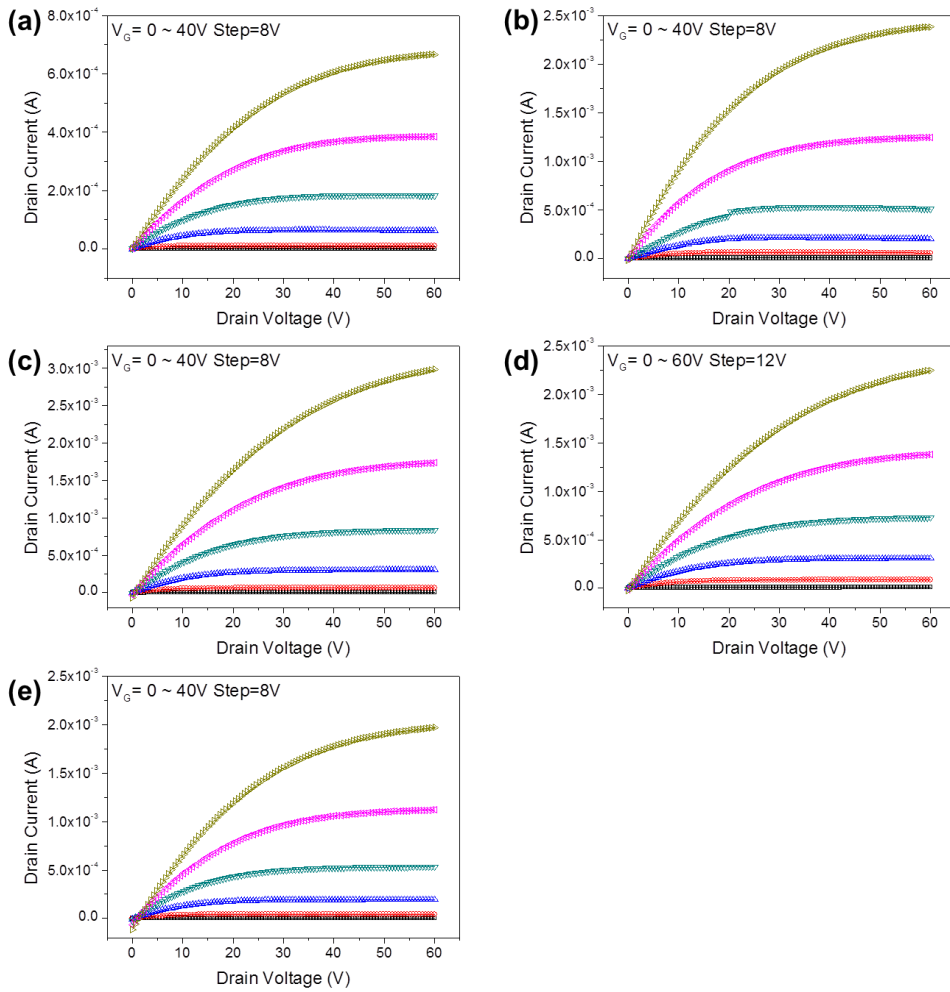


**Figure 4.3.** Output characteristics of ZnO TFTs based on (a) pristine, (b) Li doped ZnO (Li 10 mol%), (c) Na doped ZnO (Na 1 mol%), (d) K doped ZnO (K 3 mol%), (e) Rb doped ZnO (Rb 1 mol%) with SiO<sub>2</sub> gate dielectric. The gate voltage was varied between 0 V and 60 V in steps of 12 V. The channel length and width were 50 and 1000 μm, respectively.

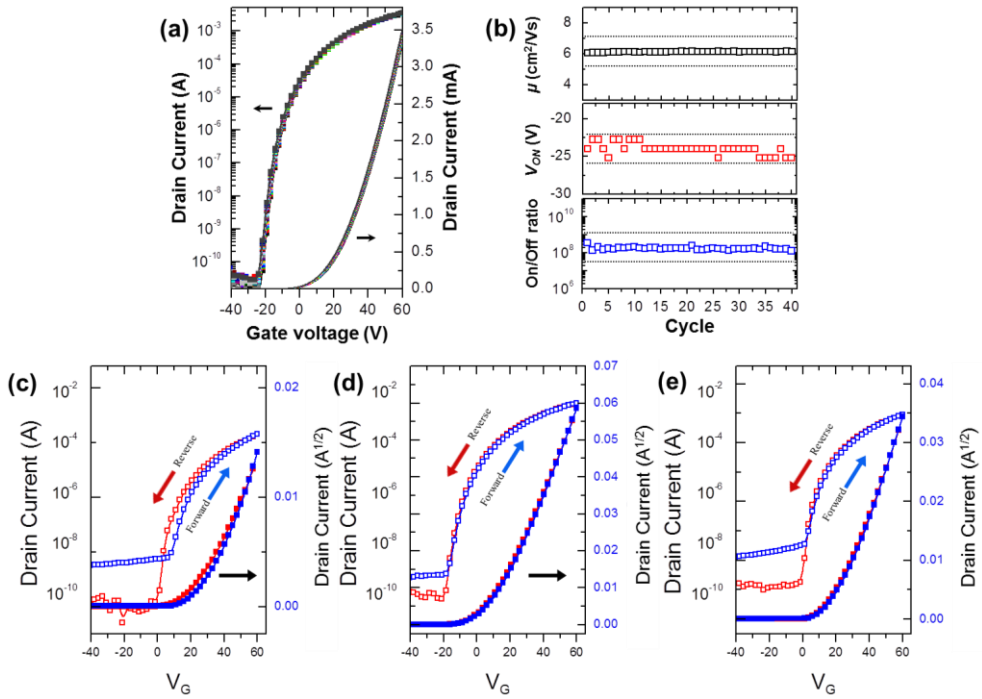


**Figure 4.4.** Operational stability of a Li doped ZnO TFT (Li 10 mol%) and the hysteresis behavior of pristine and alkali metal doped ZnO TFTs with SiO<sub>2</sub> gate dielectric. (a) evolution of transfer characteristics of a Li doped ZnO TFT during 40 continuous operations. (b) changes in the field effect mobility, turn on voltage, and on/off current ratio of a Li doped ZnO TFT during 40 continuous operations (c) pristine ZnO, (d) Li doped ZnO (Li 10 mol%), (e) Na doped ZnO (Na 1 mol%).

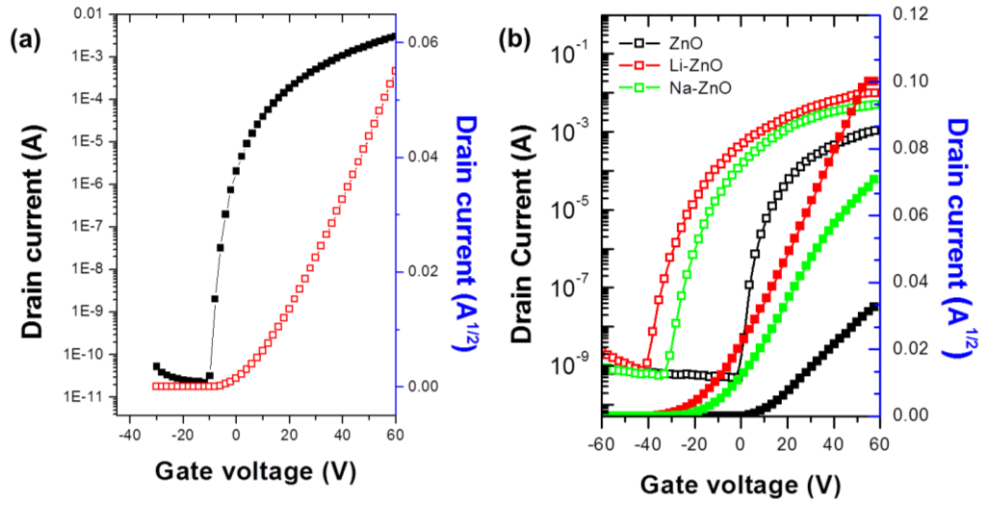


**Figure 4.5.** (a) transfer characteristics of Li doped ZnO TFTs (Li 10 mol%). A maximum field effect mobility was calculated to be  $11.45 \text{ cm}^2/\text{V}\cdot\text{s}$  at  $V_D = 60 \text{ V}$ . (b) transfer characteristics of TFTs based on pristine and alkali metal doped ZnO films annealed at  $500 \text{ }^\circ\text{C}$  with  $\text{SiO}_2$  gate dielectric (Li 10 mol%, and Na 1 mol%). The channel length and width were 50 and  $1000 \text{ }\mu\text{m}$ , respectively.

Type of TFTs	Field effect mobility ( $\text{cm}^2/\text{V}\cdot\text{s}$ )	Turn on voltage (V)	On/off current ratio
Pristine ZnO	1.6	-3.6	$2.1\cdot 10^5$
Li doped ZnO	7.3	-23.8	$3.5\cdot 10^7$
Na doped ZnO	5.9	-9.6	$6.1\cdot 10^7$
K doped ZnO	3.7	-18.0	$1.0\cdot 10^8$
Rb doped ZnO	4.3	-21.6	$3.6\cdot 10^7$

**Table 1.** Field effect mobility, turn on voltage, and on/off current ratio of pristine/alkali metal doped ZnO TFTs with 10 mol% of Li, 1 mol% of Na, 3 mal% of K, and 1 mol% of Rb.

Type of TFTs	Field effect mobility ( $\text{cm}^2/\text{V}\cdot\text{s}$ )	Turn on voltage (V)
Pristine ZnO	3.74	-1.48
Li doped ZnO	15.33	-41
Na doped ZnO	11.10	-33

**Table 2.** Field effect mobility and turn on voltage of TFTs based on pristine and alkali metal doped ZnO films annealed at 500 °C with  $\text{SiO}_2$  gate dielectric (Li 10 mol%, Na 1 mol%).

### 5.2.2. Role of alkali metal dopants in ZnO semiconductor

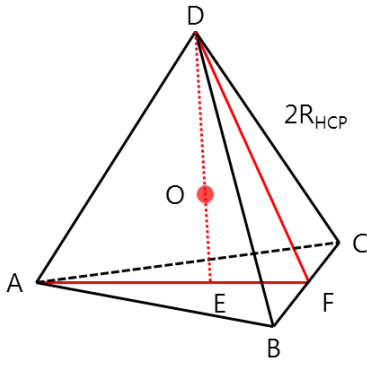
The experimental data show the obvious evidences of enhancements in field effect mobility by introducing alkali metals into ZnO semiconductors. Janotti *et al.* studied that behavior of lithium dopant could be both donor and acceptor. The donor behavior arises when lithium occurs as an interstitial impurity; the acceptor behavior is exhibited when lithium substitutes on a Zn site.<sup>25</sup> Theory predicts that Li and Na in the ZnO semiconductor prefer the interstitial sites (electron donor) over the substitutional sites (acceptor) and thus alkali metal doping enhances n-type ZnO.<sup>26</sup>

In terms of structure of nanocrystalline ZnO, alkali metal dopants could locate three position; tetrahedral site, octahedral site, and grain boundaries. The spatial distance of each site at the hexagonal close-packed structure could be calculated. In case of tetrahedron,  $r_{in}/R_{HCP}$  is 0.225 where  $r_{in}$  is radius of interstitial site and  $R_{HCP}$  is the distance between zinc and oxygen. In octahedral site,  $r_{in}/R_{HCP}$  is 0.414. In figure 4.6, schematic image of each site and calculations are shown. The lattice constant of ZnO which have wurzite structure is 3.25 Å and size of tetrahedral and octahedral interstitial site in the ZnO semiconductor is 0.73 Å and 1.34 Å, respectively.

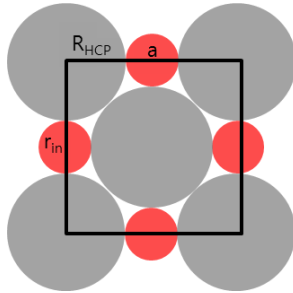
Ionic size of lithium, sodium, potassium, and rubidium is 0.9 Å, 1.16 Å, 1.52 Å, 1.66 Å, respectively.<sup>27</sup> Lithium and sodium cations could locate in octahedral interstitial site, but potassium and rubidium cations are larger than all possible interstitial sites. Hence lithium could be electron donors at interstitial sites and grain boundaries, and potassium and rubidium could locate only in the grain boundaries. These results are consistence with theoretical simulation results.<sup>26</sup> In

addition, the presence of shallow donors related to interstitial Li and Na atoms on ZnO was demonstrated experimentally by a previous analysis based on electron paramagnetic resonance and electron nuclear double resonance experiments.<sup>28</sup> Consistent with the calculation by density function theory with local density approximation and experimental results, we observed a definite increase in the drain current at saturation region and increase in field effect mobility upon introducing Li up to 10 mol%. Also a decrease (negative shift) of turn on voltage is shown, which is another key signature of n-type doping effect (Figure 4.2.a). To further understand the charge transportation in Li doped ZnO semiconductor and the cause for the improvement in field effect mobility, the temperature dependency of field effect mobility for ZnO TFTs with different Li contents (0, 5, and 10 mol%) was examined. Thermal activation energies for carrier hopping in ZnO films with different Li estimated from the slopes of the  $\ln \mu$  vs.  $T^{-1}$  plots within a temperature range of 150–290 K. A lowering of activation energy was observed upon the introduction of Li into ZnO in figure 4.7. (0 mol% is 11.85 meV, 5 mol% is 9.53 meV, 10 mol% is 7.35 meV). Similar results were obtained from p-type doped polycrystalline silicon films with different boron concentrations.<sup>29</sup>

When more than 10 mol% of Li was introduced, threshold voltage shifted positively and the field effect mobility decreased. This result also implies that adding Li beyond 10 mol% of doping concentration creates a greater number of defects in the ZnO films. The detailed experiments and discussions about lithium doping effect will be introduced in chapter 6. Furthermore, energy dispersive X-ray microanalysis (EDX) was carried out to investigate residual nitrogen atoms from ammonia in alkali metal doped ZnO films. We did not observe a nitrogen peak at 0.392 keV (figure 4.8.).



$$\begin{aligned}
 r_{in} &= OD - R_{HCP} = \frac{3}{4}DE - R_{HCP} \quad OD = \frac{3}{4}DE \\
 DE &= \sqrt{DF^2 - EF^2} = \sqrt{DF^2 - \left(\frac{DF}{3}\right)^2} \\
 &= \sqrt{\frac{8}{9}}DF = \sqrt{\frac{8}{9}}\left(\frac{\sqrt{3}}{2} * 2R_{HCP}\right) = \sqrt{\frac{2}{3}}(2R_{HCP}) \\
 r_{in} &= OD - R_{HCP} = \frac{3}{4}DE - R_{HCP} \\
 &= \frac{3}{2}\sqrt{\frac{2}{3}}R_{HCP} - R_{HCP} = \left(\sqrt{\frac{2}{3}} - 1\right)R_{HCP} \\
 \frac{r_{in}}{R_{HCP}} &= \sqrt{\frac{3}{2}} - 1 \approx 0.225
 \end{aligned}$$



$$\begin{aligned}
 r_{in} + R_{HCP} &= \frac{1}{2}a \\
 r_{in} &= \frac{1}{2}a - R_{HCP} \\
 4R_{HCP} &= \sqrt{2}a \\
 r_{in} &= \sqrt{2}R_{HCP} - R_{HCP} \\
 \frac{r_{in}}{R_{HCP}} &= \sqrt{2} - 1 \approx 0.414
 \end{aligned}$$

**Figure 4.6.** Schematic image of tetrahedral and octahedral site of hexagonal close-packed structure. Site size calculation of each interstitial sites.

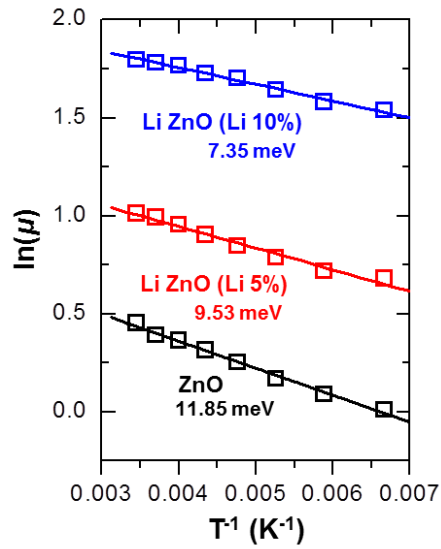


**Figure 4.7.**  $\ln \mu$  vs.  $T^{-1}$  plots of pristine/Li doped ZnO TFTs with varied doping concentrations.

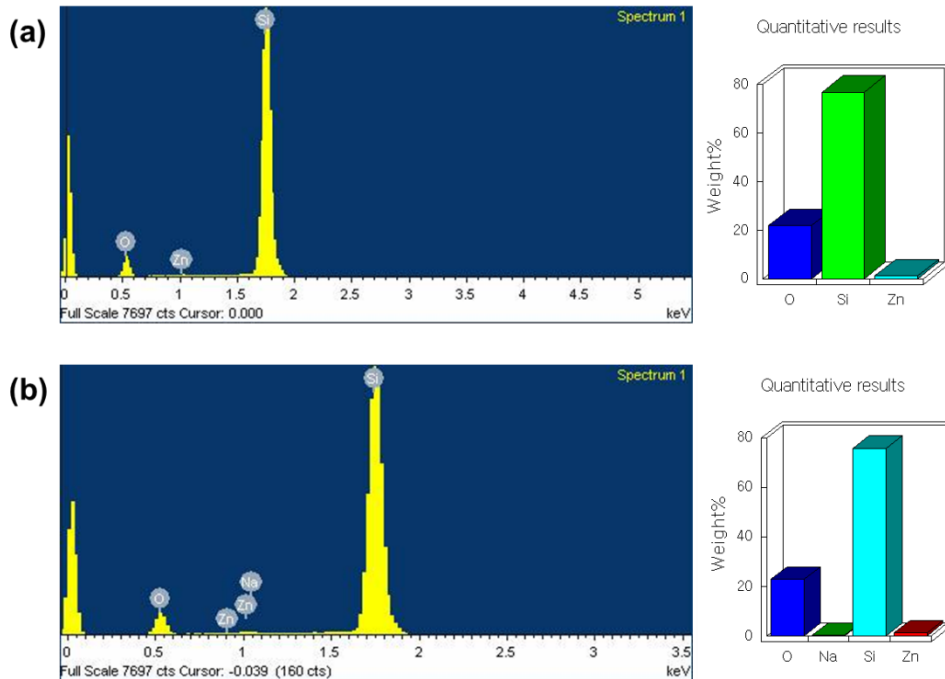


**Figure 4.8.** EDX results of (a) pristine and (b) Na doped ZnO (Na 1 mol%) films annealed at 300 °C . Note that nitrogen doping was not observed in the ZnO films utilized in this work.

### 5.2.3. Ion gel dielectric layer for low operation voltage

For more practical applications of these solution-processed alkali metal doped ZnO TFTs, low operating voltage of the devices is important. The high electrical capacitance of gate insulators with a high dielectric constant ( $k$ ) is essential to drive TFTs with a low operating voltage.<sup>30</sup> Many research groups have conducted studies using binary oxides as the gate insulator, including hafnium (Hf), zirconium (Zr), and yttrium (Y) based oxides because of their high dielectric constant ( $k$ ) and wide bandgap.<sup>31,32,33</sup> However, ion gels is the most powerful dielectric materials and serve as high capacitance gate dielectrics in TFTs operating.<sup>34</sup> This can be achieved by employing solution-processed gate dielectrics with high capacitance that allows inducing a greater number of carriers in a semiconductor channel at low applied voltages.<sup>35</sup> In particular, an ion gel including polystyrene-block-poly(methyl methacrylate)-block-polystyrene (PS-PMMA-PS) triblock copolymer and 1-ethyl-3-methylimidazolium bisimide(trifluoromethylsulfonyl) ([EMIM][TFSI]) ionic liquid was employed.<sup>33</sup> The high capacitance of the ion gel ( $5.17 \mu\text{F}\cdot\text{cm}^{-2}$  at 10 Hz) provided high on-current operation at low-voltage. Figure 4.9.a shows typical output characteristics of the ion gel gated Li doped ZnO TFTs (Li 10 mol%). The output curves show reasonable linear and saturation behaviors below 3 V. A high saturation current of around 1 mA at  $V_G = 3 \text{ V}$  and  $V_D = 2 \text{ V}$  was achieved, which originated from the high capacitance of the ion gel gate dielectric. Figure 4.9.b shows the transfer characteristics at  $V_D$  of -1 V of the ion gel gated Li doped ZnO TFTs. Negligible current hysteresis between forward and reverse  $V_G$  traces was observed. An averaged carrier mobility of  $1.6 \text{ cm}^2/\text{V}\cdot\text{s}$  was achieved with an on/off current ratio of  $10^5$  and threshold voltage of 1.2 V (Figure 4.8.d). Note that the

slightly lower field effect mobility of the ion gel gated devices, as compared to those of the SiO<sub>2</sub> gated devices, may be attributable to the relatively rougher interfaces between the Li doped ZnO active layer and the ion gel gate dielectrics.

The operational stability of transistors is another important requirement for practical applications. Figure 4.10.a shows the evolution of the linear transfer curves of an ion gel gated Li doped ZnO TFT. A sustained gate voltage of 1 V was applied over a period of 90 min. Remarkably, the shift of threshold voltage was very small. The field effect mobility, turn on voltage, and on/off current ratio were also monitored (Figure 4.10.b). The changes in each electrical parameter were within 20 %. Dynamic stress tests were also performed in which the ion gel gated Li doped ZnO TFTs were cycled continuously between on ( $V_G = -1$  V) and off states ( $V_G = 3$  V) at 0.2 Hz (Figure 4.9.c). An on/off current ratio of  $10^5$  was invariant even during 15000 continuous operations, corresponding to more than 20 h. These results confirmed the excellent operational stability of Li doped ZnO TFTs.

A simple resistor loaded inverter, with a 100 k $\Omega$  resistor connected, was fabricated with ion gel gated Li doped ZnO TFTs. An ideal inverter action with small hysteresis was observed where the output voltage was switched between 1 and 0 V as the input gate voltage was swept. The gain ( $\delta V_{out}/\delta V_{in}$ ) of the device was around 2.3, implying that these gates can be used to switch subsequent stages in more complex logic circuits (Figure 4.9.c).

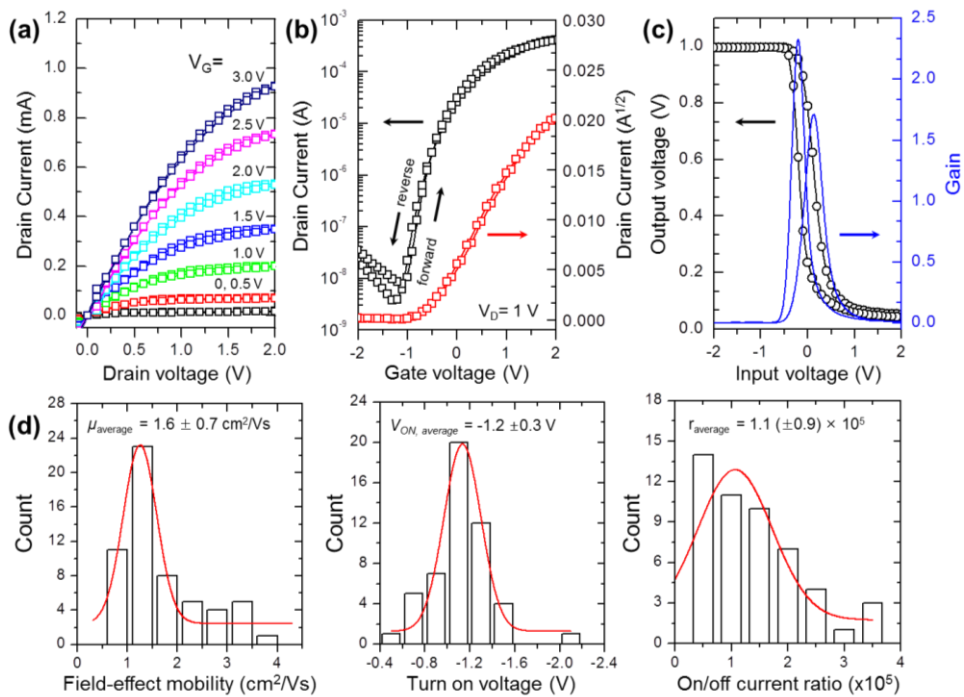


**Figure 4.9.** Electrical properties of ion gel gated Li doped ZnO TFTs (10 mol% Li).

(a) output and (b) transfer characteristics of an ion gel gated Li doped ZnO TFT (10 mol% Li). (c) static behavior of a resistor-loaded inverter with a Li doped ZnO TFT (10 mol% Li). (d) histogram of field effect mobility, turn on voltage, and on/off current ratio of ion gel gated Li doped ZnO TFTs.

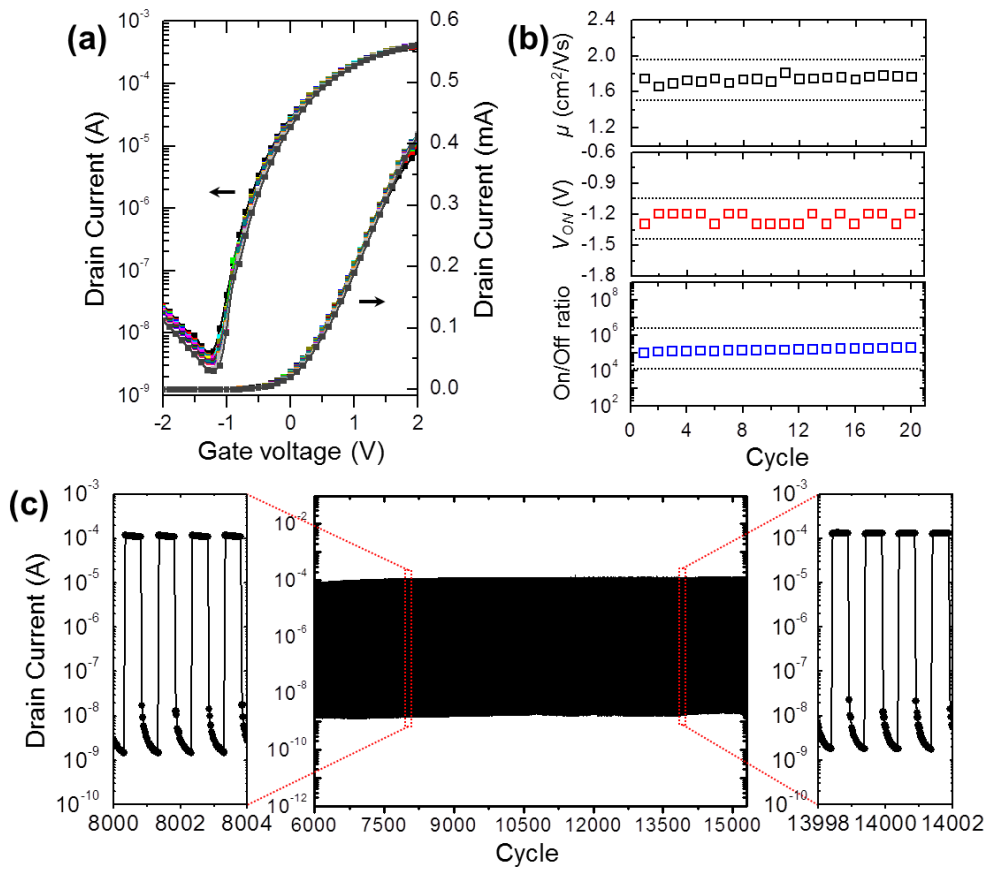


**Figure 4.10.** Operational stability of an ion gel gated Li doped ZnO TFT (Li 10 mol%). (a) evolution of the linear transfer curves of an ion gel gated Li doped ZnO TFT. The gate bias during stress was 1 V. (b) changes in field effect mobility, turn on voltage, and on/off current ratio during 20 continuous operations. (c) dynamic stress test of an ion gel gated Li doped ZnO TFT during continuous cycling between ON ( $V_G = -1$  V) and OFF states ( $V_G = 3$  V) at 0.2 Hz.

### 5.3 Reference

- [1] M. Grundmann, H. Frenzel, A. Lajn, M. Lorenz, F. Schein, H. von Wenckstern, *Phys. Status. Solidi. A.* **2010**, 207, 1437.
- [2] W. E. Spear, P. G. Lecomber, *Solid. State. Commun.* **1993**, 88, 1015.
- [3] T. Tsukada, *J. Non-Cryst. Solids.* **1993**, 166, 721.
- [4] Y. H. Kim, J. S. Heo, T. H. Kim, S. Park, M. H. Yoon, J. Kim, M. S. Oh, G. R. Yi, Y. Y. Noh, S. K. Park, *Nature.* **2012**, 489, 128.
- [5] T. Kamiya, H. Hosono, *NPG. Asia. Mater.* **2010**, 2, 15.
- [6] C. H. Chou, W. L. Kwan, Z. R. Hong, L. M. Chen, Y. Yang, *Adv. Mater.* **2011**, 23, 1282.
- [7] X. Jiang, F. L. Wong, M. K. Fung, S. T. Lee, *Appl. Phys. Lett.* **2003**, 83, 1875.
- [8] Z. L. Wang, J. H. Song, *Science.* **2006**, 312, 242.
- [9] Y. Ohya, T. Niwa, T. Ban, Y. Takahashi, *Japanese Journal of Applied Physics Part 1-Regular Papers Short Notes & Review Papers.* **2001**, 40, 297.
- [10] P. F. Carcia, R. S. McLean, M. H. Reilly, G. Nunes, *Appl. Phys. Lett.* **2003**, 82, 1117.
- [11] C. R. Gorla, N. W. Emanetoglu, S. Liang, W. E. Mayo, Y. Lu, M. Wraback, H. Shen, *J. Appl. Phys.* **1999**, 85, 2595.
- [12] Y. Natsume, H. Sakata, *Thin Solid Films.* **2000**, 372, 30.
- [13] H. C. Cheng, C. F. Chen, C. C. Lee, *Thin Solid Films.* **2006**, 498, 142.
- [14] K. Song, D. Kim, X. S. Li, T. Jun, Y. Jeong, J. Moon, *J. Mater. Chem.* **2009**, 19, 8881.
- [15] K. K. Banger, Y. Yamashita, K. Mori, R. L. Peterson, T. Leedham, J.

- Rickard, H. Siringhaus, *Nat. Mater.* **2011**, 10, 45.
- [16] M. G. Kim, M. G. Kanatzidis, A. Facchetti, T. J. Marks, *Nat. Mater.* **2011**, 10, 382.
- [17] G. Adamopoulos, A. Bashir, S. Thomas, W. P. Gillin, S. Georgakopoulos, M. Shkunov, M. A. Baklar, N. Stingelin, R. C. Maher, L. F. Cohen, D. D. C. Bradley, T. D. Anthopoulos, *Adv. Mater.* **2010**, 22, 4764.
- [18] W. H. Jeong, G. H. Kim, H. S. Shin, B. Du Ahn, H. J. Kim, M. K. Ryu, K. B. Park, J. B. Seon, S. Y. Lee, *Appl. Phys. Lett.* **2010**, 96.
- [19] G. H. Kim, W. H. Jeong, B. Du Ahn, H. S. Shin, H. J. Kim, H. J. Kim, M. K. Ryu, K. B. Park, J. B. Seon, S. Y. Lee, *Appl. Phys. Lett.* **2010**, 96.
- [20] M. Ohyama, H. Kozuka, T. Yoko, *Thin Solid Films.* **1997**, 306, 78.
- [21] S. T. Meyers, J. T. Anderson, C. M. Hung, J. Thompson, J. F. Wager, D. A. Keszler, *J. Am. Chem. Soc.* **2008**, 130, 17603.
- [22] S. Y. Park, B. J. Kim, K. Kim, M. S. Kang, K. H. Lim, T. Il Lee, J. M. Myoung, H. K. Baik, J. H. Cho, Y. S. Kim, *Adv. Mater.* **2012**, 24, 834.
- [23] B. Zhao, C. L. Wang, Y. W. Chen, H. L. Chen, *Mater. Chem. Phys.* **2010**, 121, 1.
- [24] K. Kim, S. Park, J. B. Seon, K. H. Lim, K. Char, K. Shin, Y. S. Kim, *Adv. Funct. Mater.* **2011**, 21, 3546.
- [25] A. Janotti, C. G. Van de Walle, *Rep. Prog. Phys.* **2009**, 72.
- [26] C. H. Park, S. B. Zhang, S. H. Wei, *Phys. Rev. B.* **2002**, 66.
- [27] R. D. Shannon, *Acta. Crystallogr. A.* **1976**, 32, 751.
- [28] S. B. Orlinskii, J. Schmidt, P. G. Baranov, D. M. Hofmann, C. D. Donega, A. Meijerink, *Phys. Rev. Lett.* **2004**, 92.
- [29] T. Matsumoto, Y. Mishima, *J. Appl. Phys.* **1989**, 66, 5058.

- [30] J. Ko, J. Kim, S. Y. Park, E. Lee, K. Kim, K. H. Lim, Y. S. Kim, *J. Mater. Chem. C* **2014**, *2*, 1050.
- [31] H. Shimizu, T. Sato, S. Konagai, M. Ikeda, T. Takahashi, T. Nishide, *Jpn. J. Appl. Phys. 1* **2007**, *46*, 4209.
- [32] J. H. Park, Y. B. Yoo, K. H. Lee, W. S. Jang, J. Y. Oh, S. S. Chae, H. K. Baik, *Acs. Appl. Mater. Inter.* **2013**, *5*, 410.
- [33] K. Song, W. Yang, Y. Jung, S. Jeong, J. Moon, *J. Mater. Chem.* **2012**, *22*, 21265.
- [34] J. H. Cho, J. Lee, Y. Xia, B. Kim, Y. Y. He, M. J. Renn, T. P. Lodge, C. D. Frisbie, *Nat. Mater.* **2008**, *7*, 900.
- [35] S. W. Lee, H. J. Lee, J. H. Choi, W. G. Koh, J. M. Myoung, J. H. Hur, J. J. Park, J. H. Cho, U. Jeong, *Nano. Lett.* **2010**, *10*, 347.

# **Chapter 6. Characterization of alkali metal doped ZnO TFTs with various analytic tools**

## **6.1 Introduction**

Transparency and flexibility are new terms of innovation associated with advanced display applications such as head-up displays for cars, smart windows, display tables, smart cards and rollable smart phones. Hence, thin film transistors (TFTs) as a driving element in devices that utilize an active matrix display require not only semiconductors that are capable of high level of performance but also unique materials properties such as transparency. Advanced process conditions are required, such as a low-temperature sintering for flexible devices on a plastic substrate and solution-processibility for low-cost and large-area manufacturing.<sup>1</sup> TFTs based on metal oxide semiconductors, such as In, Ga and Zn oxides, have garnered a considerable amount of interest owing to their valuable performance characteristics, such as their high electron mobility and large on/off current ratio, as compared to other semiconductors.<sup>2</sup> As metal oxide semiconductors has a wide bandgap with a large exciton binding energy, they have a good transmittance and quite a stability in air.<sup>3,4</sup> Using these outstanding characteristics, TFTs based on metal oxide semiconductors are now excellent candidates for switching devices in next generation displays. To apply metal oxide for the semiconductor in a TFT, metal oxide semiconductors have been deposited as the films on substrates using various vacuum techniques, such as pulsed laser deposition (PLD), radio frequency (RF) sputtering, metal organic chemical vapor deposition (MOCVD) and atomic layer deposition (ALD), all of which ensured outstanding electrical

performance.<sup>5,6,7,8</sup> Fortunato *et al.* reported that amorphous indium zinc oxide (IZO) TFTs fabricated by RF sputtering showed an excellent field effect mobility, which was better than that of conventional amorphous silicon TFTs by one hundred times or even better than the performance of general polycrystalline silicon TFTs.<sup>9</sup> The flexible TFTs with high field effect mobility of  $7 \text{ cm}^2/\text{V}\cdot\text{s}$  were successfully demonstrated using amorphous In-Ga-Zn-O (indium gallium zinc oxide, IGZO) semiconductors fabricated by PLD.<sup>10</sup> As the field electron mobility for applications of display devices such as OLEDs requires over  $5 \text{ cm}^2/\text{V}\cdot\text{s}$ , metal oxide TFTs have good potential for use as switching devices in advanced displays.<sup>11</sup> Despite these remarkable electrical features, batch-type vacuum deposition processes such as PLD, RF sputtering, MOCVD and ALD continue to have fundamental problems that they require high facility investment levels. Solution-processibility in ambient conditions is essential for an advanced device fabrication process to achieve low-cost and large-area manufacturing. For application to flexible devices, a low-temperature process is an important issue. In addition to these requirements, the prerequisite of indium, which is scarce but a strategically important material, is a challenge to be solved. Solution-processes such as drop-cast, spin-cast, ink-jet printing processes can be applied with soluble metal oxide precursors or nanoparticles dispersed in a solvent.<sup>12,13</sup>

In general, metal oxide semiconductor TFTs based on ZnO have been exhibited field effect mobility values ranging from  $0.2$  to  $50 \text{ cm}^2/\text{V}\cdot\text{s}$  depending on various process conditions, such as the deposition method, sintering temperature for crystallinity of the semiconductor and the interface control between the semiconductor and the insulator.<sup>14,15,16</sup> Single-crystalline ZnO semiconductor films are most favorable for TFTs capable of high electrical performance. However, to

obtain high-quality single-crystalline ZnO films, a template substrate such as single-crystal (111) yttria-stabilized zirconia is essential to grow epitaxial ZnO thin layers, and they require a very high growth temperature (700 °C).<sup>17</sup> Also, these single-crystalline ZnO semiconductors require a high-cost vacuum process such as MOCVD or PLD. These process conditions have seriously undetermined the good potential of metal oxide TFTs.

To extend the potential of ZnO TFTs into advanced displays, ZnO semiconductors require not only high electrical performance but also a low-temperature and solution-processible approach. Several previous reports have introduced polycrystalline ZnO TFTs through a low-temperature, solution-based process.<sup>13,16</sup> Meyer *et al.* reported stable precursor inks based on zinc ammine complex. These were transformed to polycrystalline ZnO for active layers of TFTs after annealing at a very low-temperature of 150 °C, and showed a field effect mobility of 0.4 cm<sup>2</sup>/V·s.<sup>13</sup> Recently, we reported the ZnO semiconductor precursors for active channel of transistors, which based on an zinc ammine complex, without time-consuming purification steps and with a low annealing temperature as maximum as 300 °C, and demonstrated the unconventional patterning technique for TFTs array using this ZnO semiconductor precursor.<sup>18,19</sup> Although some noteworthy results have been reported for the low-temperature annealing and solution-processibility, intrinsic ZnO ink still shows relatively inferior electron mobility.<sup>20</sup> This drawback is not good enough to meet the demands of advanced displays, considerable attention has been paid to various dopants to enhance the electrical performance, such as the electron mobility, on/off current ratio and reliability. To enhance the electrical performance, various metal-alloy zinc oxides such as IZO and IGZO, which are still solution-processible, have been reported to compensate for the poor

electrical performance of intrinsic ZnO semiconductors.<sup>21,22</sup> Although devices based on these metal-alloy oxide zinc semiconductors have shown good electrical performance capabilities, the massive use of indium (In) as a dopant causes some problems, which is becoming expensive and strategically important.

To address these issues, we previously introduced alkali metal dopants, particularly focused on lithium (Li) and sodium (Na), to fabricate the low-temperature and solution-processed ZnO TFTs with remarkably enhanced the field effect mobility and on/off current ratio.<sup>18</sup> The alkali metal doped TFTs not only showed excellent performance but also allowed the rare and expensive indium (In) element to be omitted. However, the exact mechanism and a detailed analysis of the alkali metal doping effects remain unavailable, which has undermined the good potential of alkali metal doped metal oxide TFTs. Herein, we discussed the alkali metal doping effects on ZnO semiconductors in terms of its crystallinity, morphology, interface charge trapping, optical bandgap, XPS analysis and so on. In addition, we proved that alkali metals locate at the interstitial sites in the polycrystalline ZnO matrix and newly suggested that the enhancement of the field effect mobility of alkali metal-doped ZnO TFTs can be successfully explained in terms of changes in the optical properties using a spectroscopic analysis.

## **6.2 Results and discussion**

### **6.2.1 Structure and morphology of alkali metal doped ZnO films**

Figure 5.1 shows cross-section HR-TEM images of Li doped ZnO films with various doping concentrations (Li, 0 mol%–15 mol%). The inset image in figure

5.1.c. shows crystalline patterns of Fast-Fourier-Transform-Selected-Area-Electron-Diffraction (FFT-SAED), and shows that Li doped ZnO films have a nanocrystalline structure. In the image of the SAED pattern, although there was faint scattering induced by an amorphous SiO<sub>2</sub> dielectric layer, we could not observe accurate information about the crystalline structure of ZnO semiconductor films with various doping concentration.

ZnO crystalline structures could be analyzed by various methods such as XRD and SAED pattern analysis. However, ZnO films from zinc ammine complex precursor have very thin thickness about 7 nm, and this thickness restrict the use of general XRD equipment. Grazing incidence wide angle X-ray spectroscopy (GI-WAXS) is the only option to investigate crystalline structure of thin films. WAXS employs the synchrotron radiation as the energy source, and this equipment has limitation of use. The last method for the crystal structure of ZnO is the direct measurement of lattice parameter in the image of HR-TEM. Figure 5.2 shows lattice parameters of pristine ZnO films on SiO<sub>2</sub> wafer. The average of lattice parameter of [101] phase was calculated by three different locations in one ZnO sample because [101] phase in ZnO films is easily distinct. It was reported that [101] phase is the majority of nanocrystalline structure of ZnO from zinc ammine complex precursor.<sup>23</sup>

As shown in figure 5.2.a, b, and c, pristine ZnO has the average lattice parameter of 2.47 Å in [101] phase of ZnO. The reference lattice parameter of [101] phase is 2.4759 Å.<sup>24</sup> 10 mol% of Li doped ZnO and 15 mol% of Li doped ZnO have the average lattice parameters of 2.48 Å and 2.14 Å, respectively (figure 5.2.d, e, f and figure 5.2.g, h). The difference of lattice parameter of pristine ZnO and 10 mol% of Li doped ZnO was 0.4 % (0.01 Å). This extra small variation is the value within

error range. When more than 10 mol% of Li was introduced, however, the difference of lattice parameter of pristine ZnO and 15 mol% of Li doped ZnO was 13.3 % (0.32 Å). This difference of lattice parameter could be the result of lattice distortion by various alloyed materials such as Li<sub>2</sub>O, Li<sub>2</sub>O<sub>2</sub>, LiZnO, and LiOH. However, it was impossible to trace the exact composition or crystal structure of the alloyed materials due to the collapse of the main structure of ZnO. From the comparison of lattice parameters of ZnO films with various lithium doping concentrations, interstitial doping is induced up to 10 mol% doping concentration and there is no lattice distortion by impurity doping. However, high doping concentration (15 mol%) induced substitutional doping and cause collapse of ZnO crystalline structure.

Figure 5.3 shows the surface morphology changes in ZnO semiconductor films using Atomic Force Microscope (AFM) at various Li doping concentrations. The values of the root mean square (RMS) roughness were 0.429 nm (pristine ZnO film), 0.565 nm (Li doped ZnO film with Li 1 mol%), 0.582 nm (Li doped ZnO film with Li 10 mol%), and 0.587 nm (Li doped ZnO film with Li 15 mol%). As the changes of the grain size or surface morphology in various ZnO films were too small, there did not seem to be any strong correlation with the enhancement in the electron mobility.<sup>17</sup> The changes of the surface morphology and grain size could not be used to explain the variance in the electron mobility of ZnO TFTs depending on the alkali metal doping concentration, as remarkable changes in the ZnO morphology were not detected in the nanocrystalline ZnO structure after the addition of alkali metal dopants.<sup>25</sup>

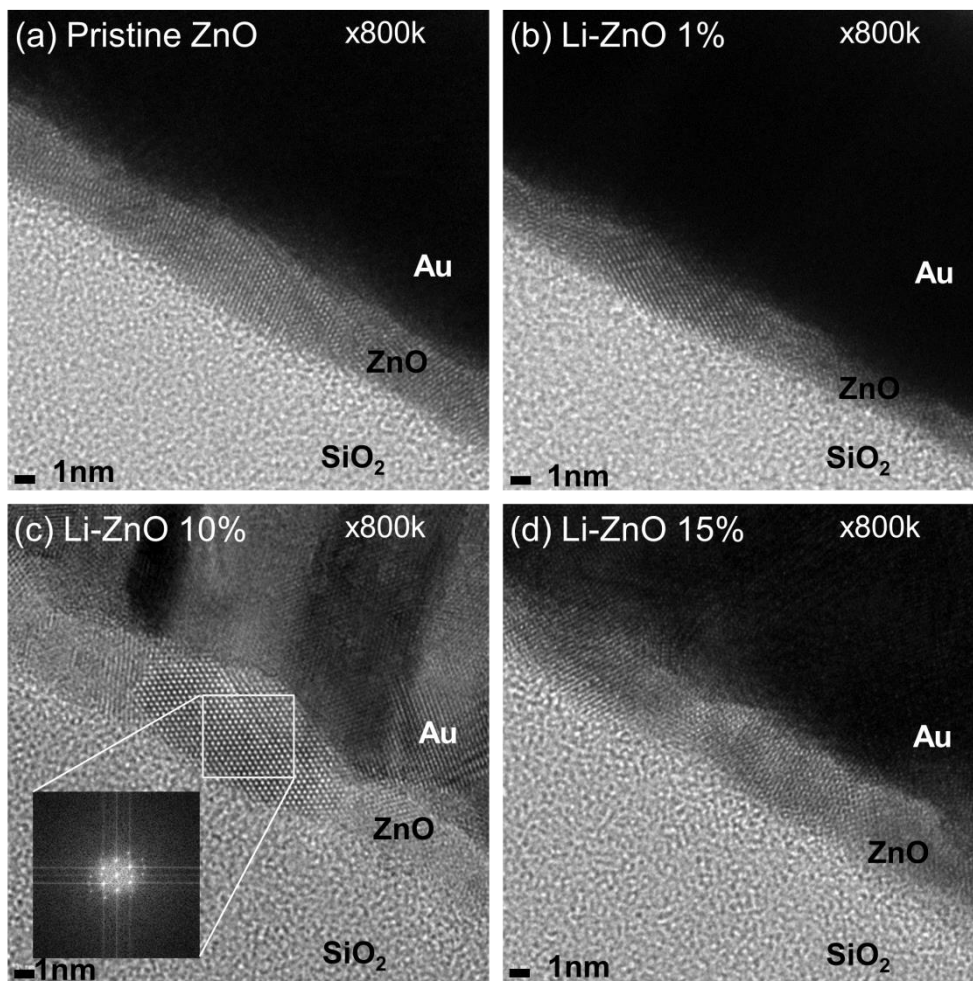


**Figure 5.1.** Cross-sectional HR-TEM images of Li doped ZnO films on the SiO<sub>2</sub> substrate at annealing temperature 300 °C. (a) pristine ZnO film, (b) Li doped ZnO film with 1 mol%, (c) Li doped ZnO film with 10 mol% (the inset shows FFT-SAED patterns), (d) Li doped ZnO film with 15 mol%.

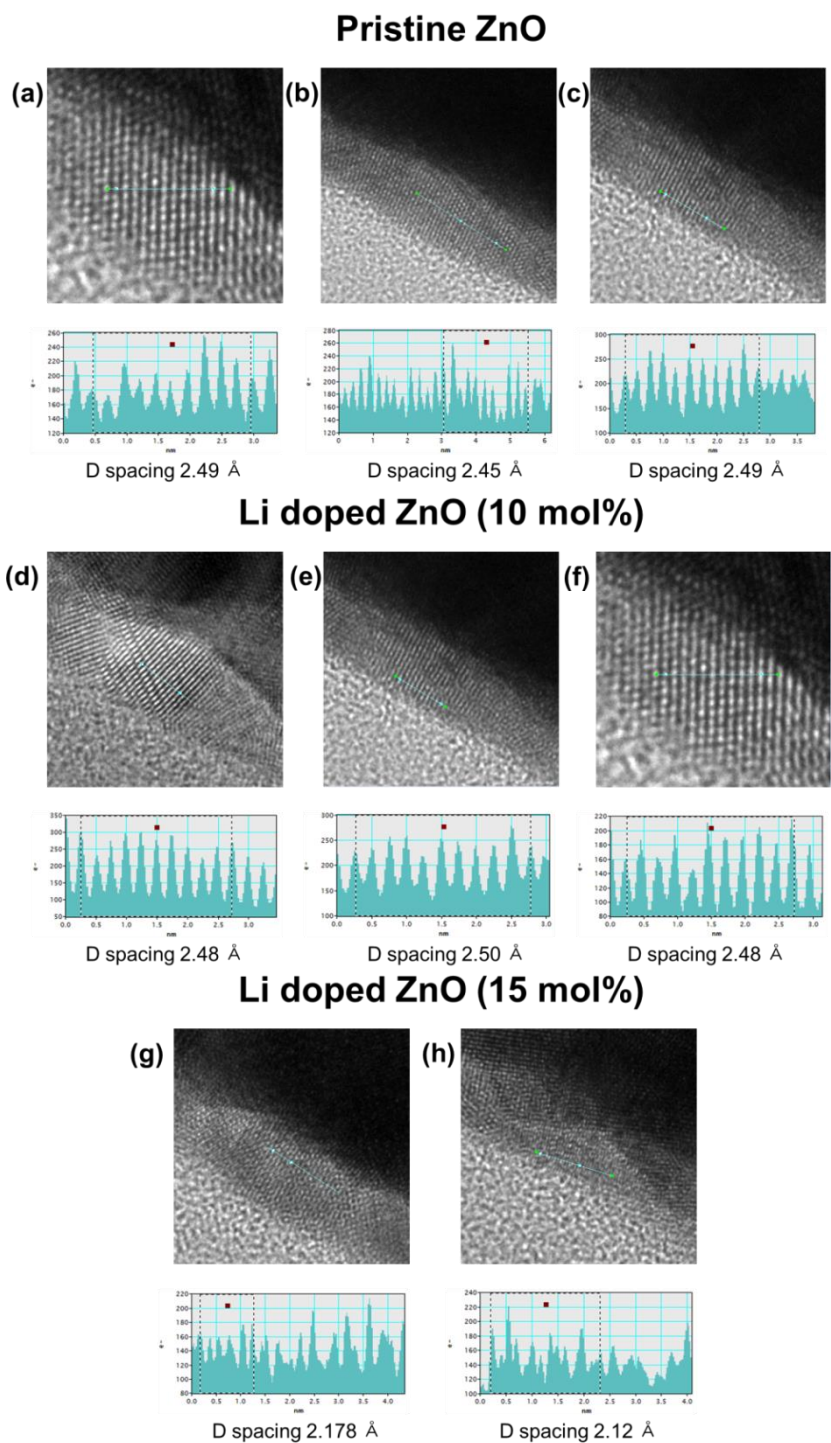


**Figure 5.2.** Cross-sectional HR-TEM images of ZnO films with various Li doping concentration (0–15 mol%) and images of lattice parameter calculation.

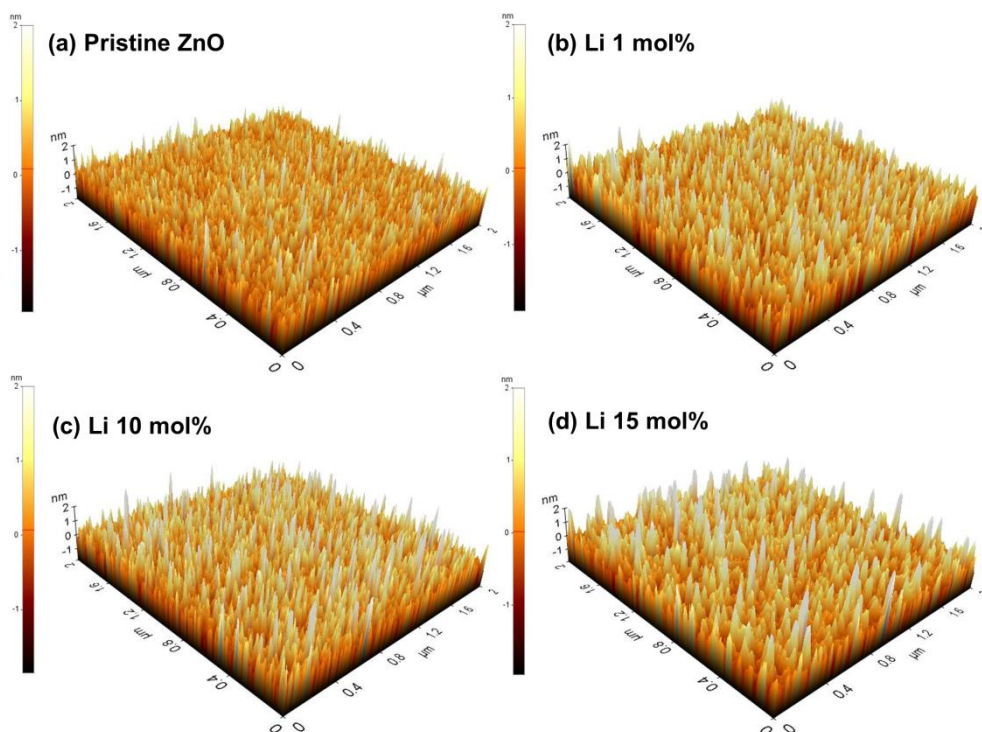


**Figure 5.3.** Atomic force microscopy (AFM) images of Li doped ZnO films. The root mean square (RMS) roughness values of ZnO films were 0.429 nm (pristine ZnO), 0.565 nm (Li 1 mol%), 0.587 nm (Li 10 mol%), and 0.524 nm (Li 15 mol%).

## 6.2.2 Interface trap of alkali metal doped ZnO films

For the TFTs used in advanced displays such as active matrix OLEDs, a highly stable threshold voltage,  $\Delta V_{th}$ , and no degradation of the field effect mobility during repeated operations are essential. Because active matrix OLEDs are a current-dependence device, the TFTs should work at a constant  $\Delta V_{th}$ .<sup>26</sup> Preventing threshold voltage shifts and maintaining high values of field effect mobility are critical issues in metal oxide TFTs when they are used as pixel switches in display applications. In general, the shift of the threshold voltage and field effect mobility during bias stress comes from defects in the semiconductor layer or trap in the interface between the semiconductor and the dielectric layer.<sup>27</sup> As mention in chapter 2.3, this shift upon application of a bias stress could be caused by charge trapping at the channel/gate insulator interface. Through an investigation of the bias stability of ZnO TFTs, the charge trapping sites in the ZnO matrix or interface charge trapping between the ZnO semiconductor and dielectric layers could be elucidated. In our experiments, variables are lithium doping concentration and the same silicon oxide dielectric layer was used. We assume that the effect of bulk traps in same dielectric layer is irrelevant. To exclude the shift of the threshold voltage and field effect mobility induced by chemical reaction and interface diffusion in ZnO semiconductors with ambient oxygen or moisture, bias stability tests were carried out in a vacuum condition.<sup>28</sup>

Figure 5.4.a and b shows the positive shift of the transfer curves of pristine ZnO and 10 mol% Li doped ZnO TFTs depending on the operation time under positive bias stress. A strong gate bias ( $V_G$ ) of 50 V was continuously applied under vacuum conditions for 6,000 seconds. The relative threshold voltage shifts ( $\Delta V_{th}$ ) of TFTs

fabricated with a ZnO semiconductor including Li 10 mol% and a pristine ZnO semiconductor as a reference are summarized in figure 5.4.a and b respectively. Remarkably, the threshold voltage shift in the Li doped ZnO TFTs ( $\Delta V_{th} = 1.67$  V) was much smaller than that in the pristine ZnO TFTs ( $\Delta V_{th} = 6.24$  V). The improvement of  $\Delta V_{th}$  could be understood in terms of the decrease in the interface defects induced from the Li doping in the ZnO matrix. In general, as solution-processed ZnO films have considerable numbers of intrinsic defects in spite of the completeness of the chemical reactions, pristine ZnO TFTs show a slight instability in their  $\Delta V_{th}$  values. Otherwise, at the optimized doping of Li (10 mol%), the charge trapping sites in the ZnO matrix or the interfaces between the ZnO semiconductors and the dielectric layers were reduced by the efficient compensation of traps with Li interstitial doping. Previously, we reported an enhancement of the charge transport in a Li doped ZnO semiconductor using an observation of the thermal activation energy of carrier hopping.<sup>18</sup> These results indicate that the charge trapping sites in the ZnO matrix can be reduced by Li doping in ZnO semiconductors. Furthermore, we think that the highly stable operation of Li doped ZnO TFTs is attributed to the effectual offsetting of the interface traps with Li doping. The electrical stability of ZnO TFTs was quantified by the modeling of the threshold voltage shift using the stretched exponential equation, as

$$\frac{\Delta V_{th}}{\Delta V_0} = \frac{V_{th} - V_{th,initial}}{V_G - V_{th,initial}} = 1 - \frac{1}{\left\{1 + \exp\left[\frac{(E_{th} - E_A)}{k_B T_0}\right]\right\}^{\frac{1}{\alpha-1}}} \quad (1)$$

$V_{th,initial}$  is the initial threshold voltage,  $E_A$  is the typical activation energy for trap creation,  $k_B T_0$  is the slope of the activation energy distribution, and  $\alpha$  is a constant.  $E_{th}$  corresponds to the thermalization energy, defined by

$$E_{th} = k_B T \ln(vt) \quad (2)$$

here,  $k_B$ ,  $v$ ,  $T$  and  $t$  are the Boltzmann constant, the attempt-to-escape frequency, the temperature and the bias stress time, respectively. All possible defect-creation sites with  $E_A < k_B T \ln(vt)$  will then have converted into defects after a time  $t$  at a temperature  $k_B T$ . The curves of  $\Delta V_{th}$  vs. the operation time in figure 5.4.c successfully show the saturation of  $\Delta V_{th}$ , which is a prerequisite of equation (1).<sup>29</sup> Also, as the pristine and Li doped ZnO TFTs in this approach have negligible hysteresis, we successfully calculated  $E_A$  and  $k_B T_0$  from the fitting parameters ( $E_A$ ,  $k_B T_0$ ,  $v$ , and  $\alpha$ ) in figure 5.4.d. The calculated parameters of  $v$  and  $\alpha$  were  $1 \times 10^5$  Hz and 1.5, respectively.<sup>30</sup> These values were acceptable and reasonable, considering previously reported values.<sup>31</sup> The parameters related to the activation energy, i.e.,  $E_A$  and  $k_B T_0$ , varied depending on the Li dopant concentration, as summarized in Table 1. As a high activation energy for trap creation,  $E_A$ , in a semiconductor induces stable operation and a small value of  $\Delta V_{th}$  when the device operates, Li doping could efficiently improve the electrical stability of ZnO TFTs.<sup>29</sup> We think that the drop of  $\Delta V_{th}$  values in Li doped ZnO TFTs (Li 10 mol%) are attributed to interstitial doping of Li in the nanocrystalline ZnO structure.

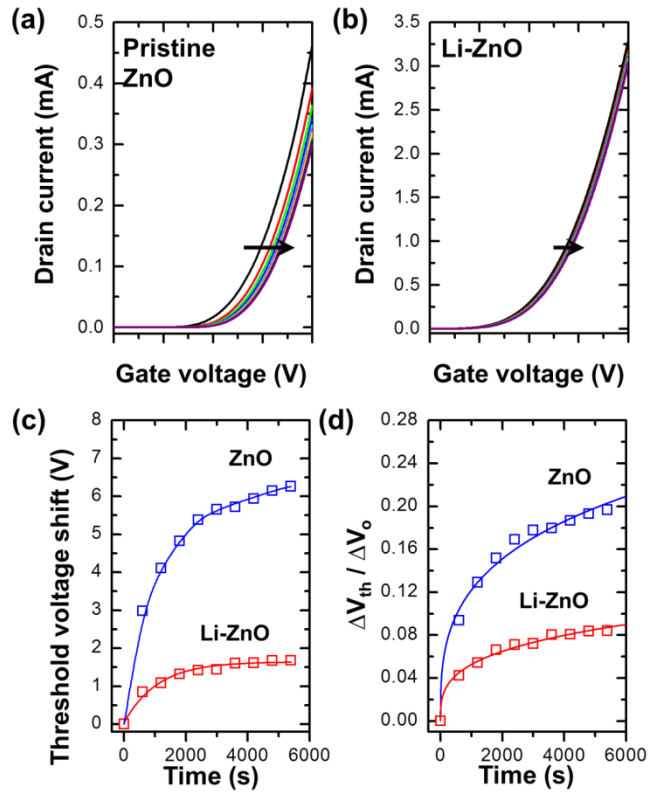


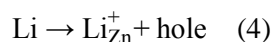
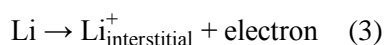
**Figure 5.4.** (a) evolution of the transfer curves of pristine ZnO TFTs, as a function of bias stress time (0–6000 s). (b) evolution of the transfer curves of Li doped ZnO TFTs (10 mol%), as a function of bias stress time (0–6000 s). (c) relative threshold voltage shift ( $\Delta V_{th}$ ) of Li doped ZnO TFTs (10 mol%) as a function of stress time. (d) plot of  $\Delta V_{th}/V_0$  vs. bias stress time for the pristine and Li doped ZnO (10 mol%) TFTs. The solid curves were fit to a stretched exponential equation.

Fitting parameter	Pristine ZnO	Li ZnO (10 mol%)
$E_A$ (eV)	0.679 ( $\pm$ 0.013)	0.772 ( $\pm$ 0.018)
$K_B T_0$ (eV)	0.075 ( $\pm$ 0.006)	0.082 ( $\pm$ 0.005)

**Table 3.**  $E_A$  and  $k_B T_0$  of pristine and Li doped ZnO TFTs (10 mol%).

### 6.2.3 Relation between doping concentration and mobility

Zinc oxide has the unique characteristic in which the injection of electron carriers can be achieved by chemical doping. In conventional crystalline materials such as silicon semiconductors, substitutional doping is a conventional phenomenon which serves to enhance the semiconductor properties from their intrinsic levels. However, in the ZnO semiconductor, as zinc ions have strong ionic bonding with oxygen and bonding has flexibility in coordination structure, the doping mechanism is somewhat more complex than that of a conventional Si semiconductor. A p-type semiconductor property can be obtained when a considerable amount of lithium (Li) exists at substitutional sites in the ZnO matrix.<sup>32</sup> In such a case, lithium acts as an acceptor, which can lead to p-channel of ZnO TFT at negative gate voltage. However, Park *et al.* predicted that Li (or Na) in the ZnO matrix prefers basically interstitial sites to substitutional sites using the first-principles pseudopotential method based on the local density approximation.<sup>33</sup> Alkali metal elements tend to occupy the interstitial sites, in part mitigated by their small atomic radii, rather than substitutional sites, and therefore, act mainly as electron donors instead.<sup>34</sup> Also, Hosono *et al.* suggested the possibility of effective n-type doping in ZnO through the ion implantation of a cation that has low electron affinity.<sup>35</sup> If group-I elements occupy the interstitial sites, they act as a shallow donor.<sup>33</sup> Li in ZnO can occupy the interstitial site as well as the substitutional zinc site in the ZnO matrix. Equations (3) and (4) explain the Li defect mechanism in ZnO.<sup>36</sup>



$\text{Li}_{\text{Zn}}$  and  $\text{Li}_i^{+}$  represent the lithium on the Zn lattice sites in the substitutional

position and the lithium in the interstitial position on the lattice, respectively. ZnO with a wurtzite structure is naturally an n-type semiconductor because of a deviation from stoichiometry due to the presence of intrinsic defects such as O vacancies and Zn interstitials. Given that intrinsic ZnO is an n-type semiconductor that has donor electrons, the interstitial doping can improve the carrier concentration by the increment of electrons. The lattice parameters of [101] phase from HR-TEM images also support that lithium dopants exist at interstitial sites and there is no lattice distortion of ZnO up to 10 mol% of Li doping concentration. Exceeding the optimum dopant concentration (10 mol%), however, the substitutional doping of Li occurred and neutralizes the carriers in the ZnO semiconductor and reduces the field effect mobility of ZnO TFTs. In our experiments, ZnO semiconductor films have nanocrystalline structures and field effect mobility of them is affected by carrier concentration. Following the theory of polycrystalline silicon semiconductor, electron mobility is defined by

$$\mu_D = \mu_0 \left( \frac{N_c}{N_t} \right) \exp\left(\frac{-E_T}{kT}\right) \quad (5)$$

where  $\mu_D$  is mobility of disordered semiconductor,  $N_c$  is the effective density of states in the conduction band, and  $N_t$  is the the number of traps, and  $E_T$  is the energy of thermally activated electron. Increased electron density raise probability which electron could be transport in the extended states. Therefore, we assume that the majority of the alkali metal ions must exist as interstitial donors in the structure rather than as substitutional acceptors and alkali metal dopants enhanced the field effect mobility.

## 6.2.4 Optical analysis of alkali metal doped ZnO films

To investigate interstitial doping, we measured the optical bandgap using a UV-Vis spectroscope. The optical bandgap energy,  $E_{\text{opt}}$ , can be calculated from the absorption coefficient ( $\alpha$ ). We modified equation of optical absorption coefficient as follows,<sup>37</sup>

$$T_{\text{ZnO/glass}} = e^{-(\alpha_{\text{ZnO}}d_{\text{ZnO}})} \times e^{-(\alpha_{\text{g}}d_{\text{g}})}, T_{\text{g}} = e^{-\alpha_{\text{g}}d_{\text{g}}} \quad (6)$$

$$T_{\text{relative ZnO}} = \frac{T_{\text{ZnO/glass}}}{T_{\text{glass}}} = e^{-\alpha_{\text{ZnO}}d_{\text{ZnO}}} \quad (7)$$

$$-\frac{1}{d} \ln(T_{\text{relative ZnO}}) \cong \alpha \quad (8)$$

$D$  is the film thickness and  $T$  is the transmittance. The thickness of ZnO films with 7 nm. We estimated the optical bandgap from the intersection of the linear extrapolated line with the horizontal axis,<sup>38</sup>

$$(\alpha h\nu)^n = A(h\nu - E_{\text{opt}}) \quad (9)$$

$A$  is a constant and  $h\nu$  denotes the photon energy. The value of  $n$  in equation (9) was obtained the best straight line fit to the experimental data for  $n=2$  when  $\alpha$  was plotted against  $h\nu$ . The measured optical bandgap ( $E_{\text{opt}}$ ) was defined as follows,

$$E_{\text{opt}} = E_{\text{g}} - \Delta E \quad (10)$$

The Burstein-Moss shift,  $\Delta E$ , could be expressed as,

$$\Delta E = \frac{h^2 E_{\text{B}}}{8\pi^{2/3}}, E_{\text{B}} = \frac{N^{2/3}}{m_e^*} \quad (11)$$

Thus, equation (10) could be written as follow.

$$E_{\text{opt}} = E_{\text{g}} + \frac{h^3 n^{2/3}}{8m_e^* \pi^{2/3}} \quad (12)$$

$N$  is carrier concentration. Assuming the effective mass  $m_e^*$  to be independent of low doping concentration, we could determine the optical bandgap of pristine ZnO film and the average value of  $m_e^*$  from the UV transmittance plot.<sup>39</sup> To calculate

the optical bandgap, the linear data region of pristine ZnO film was selected. Generally, the band gap of intrinsic ZnO is 3.3 eV, however, the calculated optical bandgap of pristine ZnO film which we selected was 3.24 eV. Under the same linear data region (3.5 eV–3.64 eV) of  $(\alpha h\nu)^2$  vs. photon energy plot, the  $E_{\text{opt}}$  of Li doped ZnO films (1mol%–15mol%) was calculated respectively.

Figure 5.5.a shows the transmission spectra of Li doped ZnO films annealed at 300 °C in ambient air for 1 hour. All films have an average optical transparency that exceeds 90% in the visible wavelength range. The inset image in figure 5.5.a shows that the transmittance was elevated and then declined as the Li concentration increased. These results can be correlated with the change of the optical bandgap value. Figure 5.5.b shows a plot of  $(\alpha h\nu)^2$  vs. the photon energy in the various ZnO films; the  $E_{\text{opt}}$  value can be obtained by extrapolating the linear region to the photon energy axis. The optical bandgap energy values,  $E_{\text{opt}}$ , of Li doped ZnO films were 3.26 eV (0 mol%), 3.28 eV (1 mol%), 3.29 eV (10 mol%), and 3.28 eV (15 mol%).

The widening of the  $E_{\text{opt}}$  values was induced from the quantum confinement size effect (QSE). The QSE arises when the crystalline size of ZnO is similar to its Bohr exciton radius. Size dependence of the optical bandgap energy is clearly detected in the QSE regime when ZnO particles are smaller than 5 nm.<sup>40</sup> However, HR-TEM images show that the crystalline size of ZnO is far from the QSE regime. Also, Burstein-Moss effect is generally observed in a degenerate electron distribution such as ZnO:Al, ZnO:Ga and ITO. However, unlike silicon semiconductor, degenerated metal oxide semiconductor which has a high carrier concentration (over the threshold carrier concentration for degeneracy ( $N > 10^{18} \text{ cm}^{-3}$ )) could have still semiconducting properties.<sup>41</sup> These electrical properties are caused by potential

barriers which were induced by disordered structure. Disordered structure has high trap density and this defect capture electron which hamper the transportation of electron. In case of ZnO films which have a low carrier concentration ( $N < 10^{18} \text{ cm}^{-3}$ ), the band gap widening could be still applied to explain relationship of carrier concentration vs. the optical bandgap. Disordered semiconductors have band tail and these localized states induce bandgap narrowing of ZnO. Add to this localized states, increased carrier concentration have similar effect that electrons are filled over conduction band. But actually, additional carriers increased electrons over mobility edge ( $E_c$ ). The schematic images of these effects are shown in figure 5.5. There are good examples in some remarkable papers of Hosono *et al.*<sup>35,42</sup> Thus, the increase and decrease in the  $E_{\text{opt}}$  values given various alkali metal dopant concentrations could be explained by Burstein-Moss like effects. In keeping with Burstein-Moss like effects, because a doubly occupied state is restricted by the Pauli principle and assuming that the optical transition is vertical, extra energy is required to excite valence electrons to higher states in the conduction band, which causes the widening of the optical bandgap.<sup>43</sup> The alkali metals located at interstitial sites in the ZnO matrix cause an increase in the donor electrons (Equation 3), and the widening optical bandgap is caused by excess donor electrons. When 10 mol% of lithium hydroxide was added, the Li doped ZnO TFTs were highest in terms of field effect mobility and this relation is shown in figure 5.7.a. The box chart of optical band gap vs. Li doping concentration is shown in figure 5.7.b and the distribution chart of Li doped ZnO TFT is shown in 5.8.

The narrowing of the  $E_{\text{opt}}$  value from 3.29 eV to 3.28 eV can be explained by the substitutional doping of Li. When the Li concentration in the ZnO matrix exceeded 10 mol%, despite the interstitial doping that occurred, substitutional Li doping also

occurred simultaneously and in considerable amounts. This substitutional doping of Li generated the electron acceptors (the holes) induced by Li at the substitutional sites (Equation 4), which neutralized the electron donors induced by Li at interstitial sites and decreased the field effect mobility of TFTs. This explanation coincides in the result of lattice parameter change in HR-TEM images. Distortion of lattice parameter supported substitutional doping of lithium. The change of the optical bandgap energy in Li doped ZnO semiconductors as supported by the Burstein-Moss shift successfully showed the increase and decrease of the field effect mobility of Li doped ZnO TFTs and the connection between this and the doping concentration of lithium (Li).

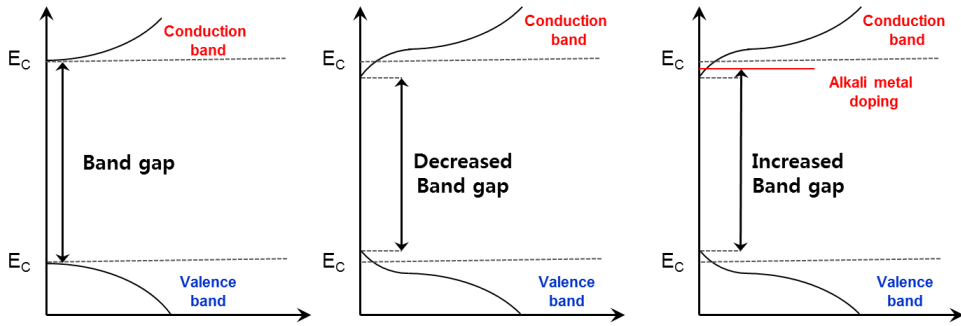


**Figure 5.5.** Schematic images of band gap widening on disordered semiconductor.

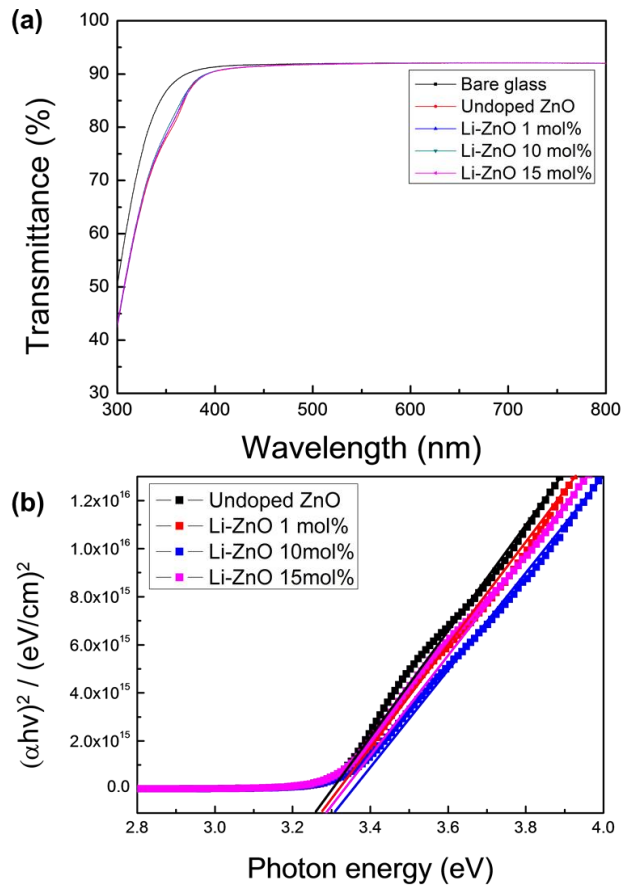


**Figure 5.6.** (a) the transmittance data of Li doped ZnO films on the glass substrate. The inset shows that the transmittance was elevated and then declined with increasing Li concentration. (b) the  $(\alpha h\nu)^2$  vs. photon energy plot of the Li doped ZnO films with various doping concentrations (0, 1, 10 and 15 mol%).

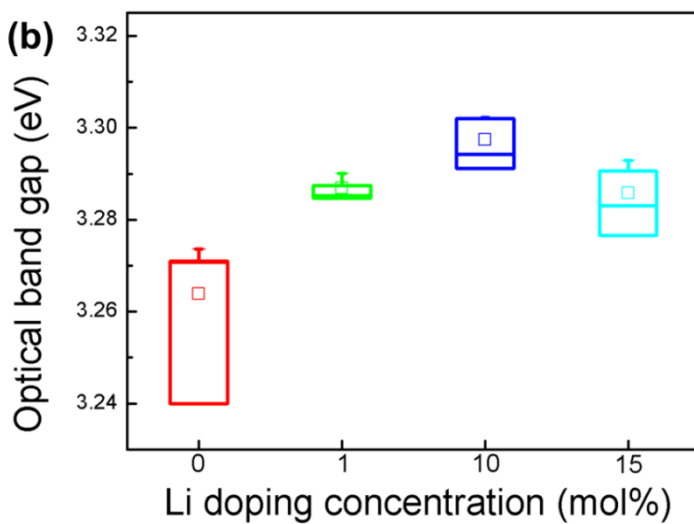
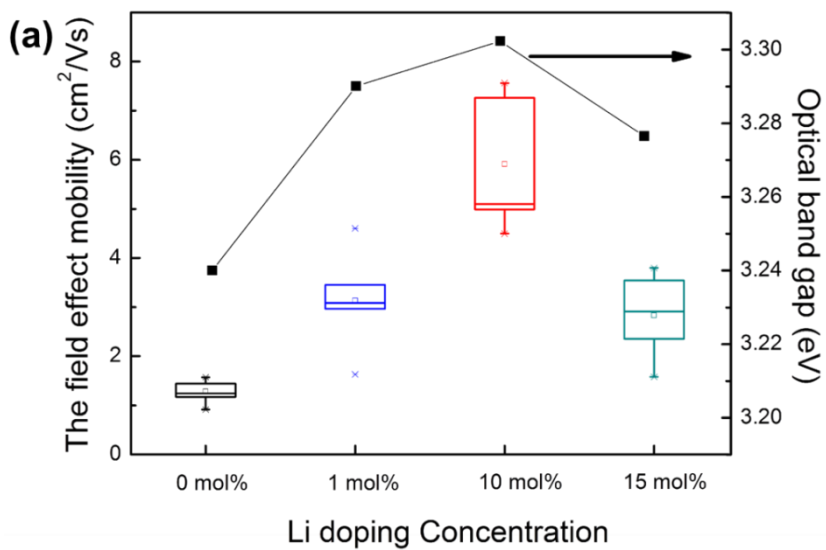


**Figure 5.7.** (a) the field effect mobility and optical band gap energy of Li doped ZnO semiconductors with various doping concentrations (0, 1, 10 and 15 mol%). (b) the box chart of optical band gap vs. Li doping concentration.

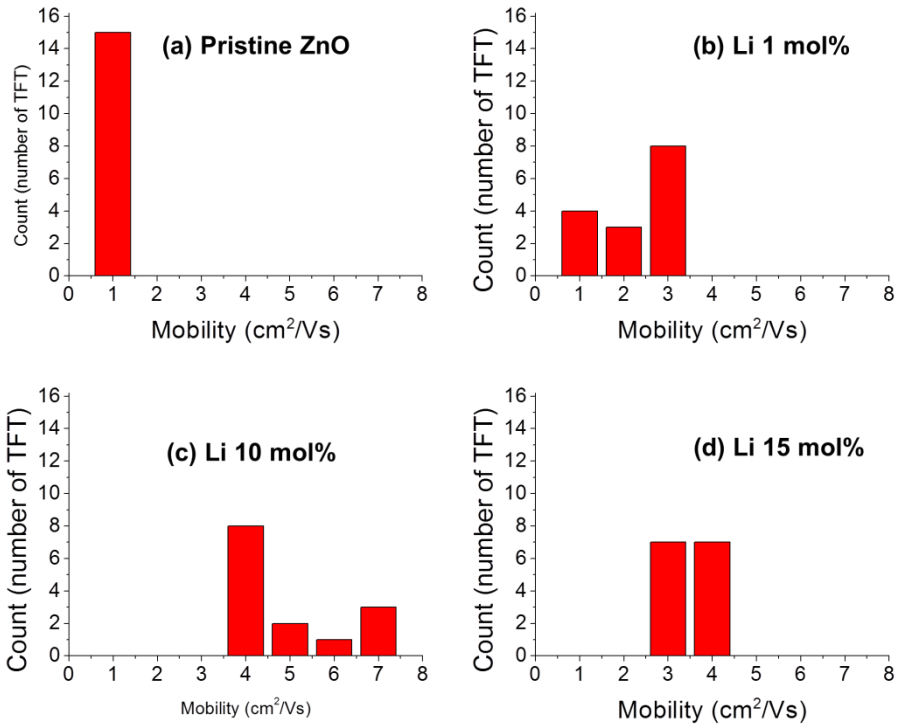


**Figure 5.8.** The average field effect mobility of Li doped ZnO TFTs as one run at 300 °C. (a) pristine ZnO. (b) Li doped ZnO (1 mol%). (c) Li doped ZnO (10 mol%). (d) Li doped ZnO (15 mol%).

## 6.2.5 Investigation of residual doping effect

The chemical requirements for any sol-gel solution-process for metal oxide semiconductors are the completed reaction and absence of residuals in the semiconductor films after the reaction.<sup>13</sup> Although solution-processed ZnO TFTs using various precursors, including In and Ga, which induce good electrical properties, have been reported, ZnO semiconductors based on sol-gel methods are associated with critical problems, as the completeness of the reaction and the presence of residuals should be solved.<sup>44,45</sup> For the complete removal of carbon based organic ligands such as acetate functional groups in the sol-gel precursors of ZnO semiconductors, these films, coated using ZnO precursors with carbon based organic ligands, should be fabricated by post-heating at temperatures in excess of 400 °C so as to be residual-free.<sup>46</sup> High annealing temperature process restricts the use of typical plastic and flexible substrates for advanced electronics and is not applicable to the fabrication of low-cost devices. In general, several methods of preparing precursors to overcome high processing temperatures have been reported, but they require an indium dopant for high-performance ZnO TFTs.<sup>21,22</sup> Also, these previously reported results are not free of carbon-residuals after a low-temperature annealing process.

In this study, we used the zinc ammine complex as a precursor for ZnO semiconductors. Although the sintering temperature in this method was relatively low compared to the sintering temperatures of typical sol-gel methods, at a maximum of 300 °C, zinc ammine complex could be transformed easily into ZnO semiconductor films which did not contain any residuals as a consequence of the volatile ammonia ligands.<sup>20</sup> The completeness of the chemical reactions at a low-

temperature processing reinforced the versatility of the solution-processed ZnO TFTs in this approach. Also, alkali metal doping successfully contributed to the enhancement of the electrical properties of ZnO TFTs without any carbon or unfavorable residuals.

Thermal gravimetric analysis (TGA) data show that the  $\text{NH}_3$  loss process finished completely below 100 °C. From the TGA analysis in figure 5.9., the evaporation of  $\text{NH}_3$  occurred earlier than that of water. Above 100 °C, the residual nitrogen was negligible. For an in-depth study of residual nitrogen, we used electron spectroscopy for a chemical analysis. Figure 5.10 shows the X-ray photoelectron spectroscopy (XPS) spectra of the pristine, Li doped, and Na doped ZnO films fabricated with the aqueous zinc ammine complex precursor on  $\text{SiO}_2$  substrates annealed at 300 °C. If residual nitrogen existed in the prepared films, a peak at 398.1 eV would have been detected. However, clear peaks around 398.1 eV could not be observed in any case in the ZnO films. Only alkali metal dopants were detected at 56 eV and 1072 eV for Li and Na, respectively (figure 5.11.a and b). Inset image of 5.11.a shows the Li 1s peak located at 52.9 eV which is related to Li interstitials corresponding to the valence state of incomplete oxidation.<sup>47</sup> While investigating the HR-TEM results, an energy-dispersive spectrometer (EDS) was used to assess the Li doped ZnO films. Figure 5.12 shows the EDS spectrum of ZnO films with various Li concentrations (0 mol%, 1 mol%, 10 mol%, and 15 mol%). In the EDS analysis, there were no noticeable spectra of residual nitrogen in the alkali metal doped ZnO semiconductor films.

For detecting alkali metal dopants in ZnO films, we carried out TOF-SIMS (time of flight secondary ion mass spectroscopy). Figure 5.13 shows the intensity of Li, Zn and O in alkali metal doped ZnO thin films. In the Li doped ZnO film, high

intensity of Li cations was detected. Both XPS and TOF-SIMS showed the existence of alkali metals in alkali metal doped ZnO films. The investigation of the residuals in alkali metal doped ZnO semiconductor films, as supported by the XPS and EDS data, showed the completeness of the reaction between the zinc ammine complex and alkali metal doped one as a precursor for ZnO semiconductor films.

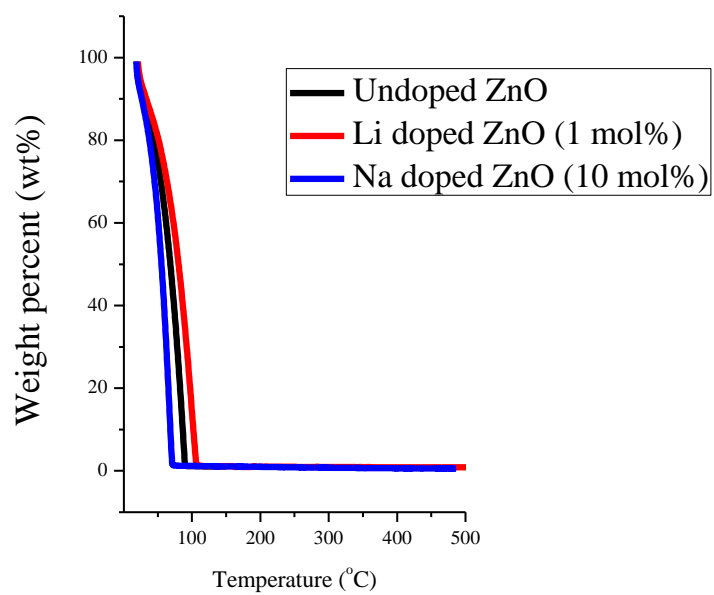


**Figure 5.9.** The TGA data of various alkali metal doped ZnO films.

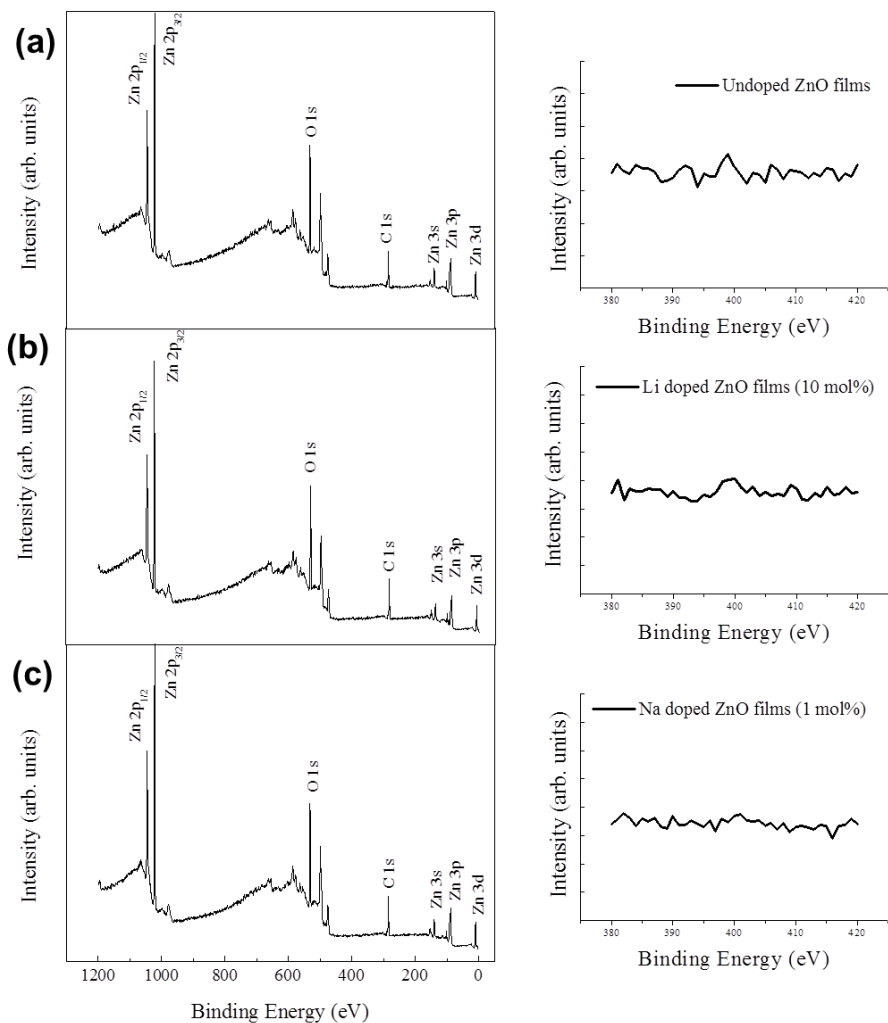


**Figure 5.10.** The wide scan spectrum of ZnO films annealed at 300 °C. (a) pristine ZnO film. (b) Li doped ZnO film (10 mol%). (c) Na doped ZnO film (1 mol%). The right plots show that the residual nitrogen (the peak at 398.1 eV) was not detected.

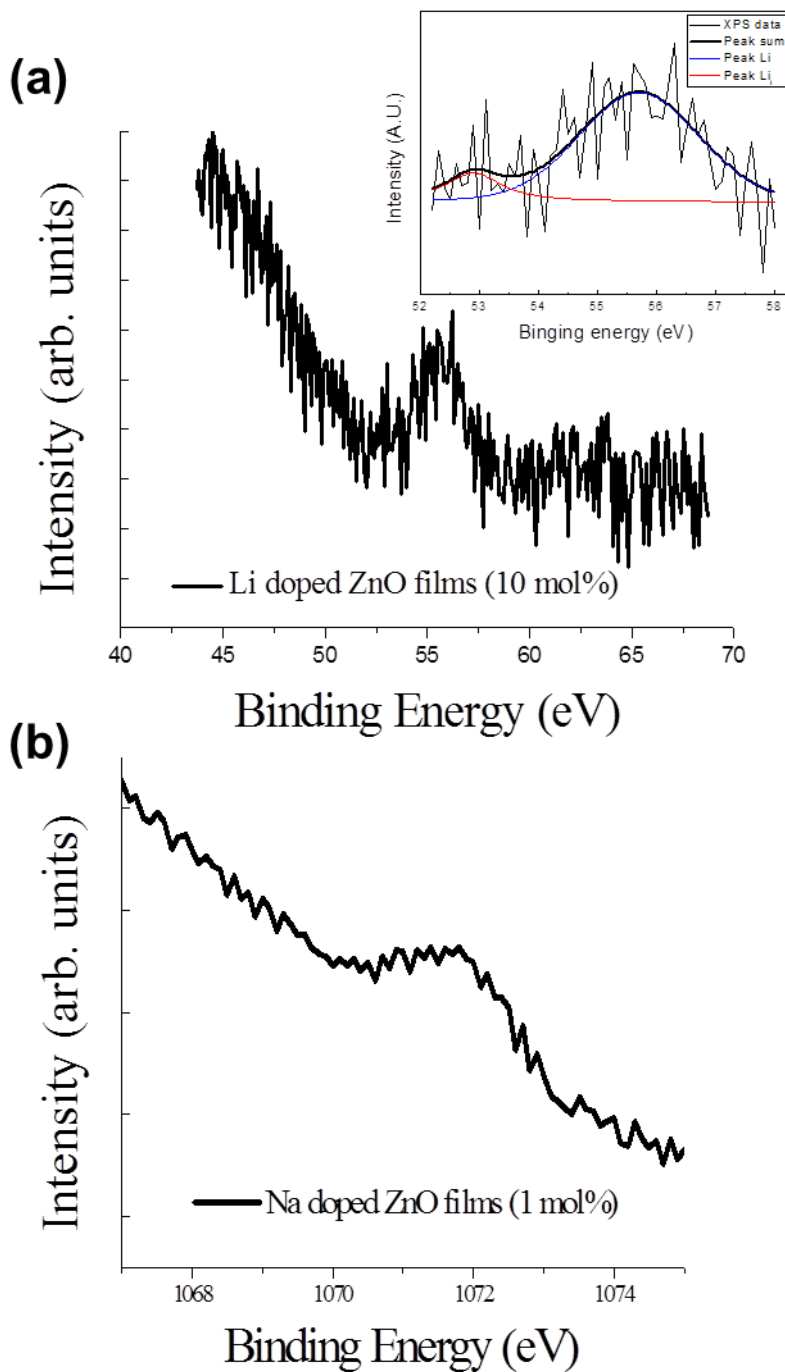


**Figure 5.11.** XPS spectra of alkali metals doped ZnO films. (a) Li peaks at 55.7 eV in Li doped ZnO films (10 mol%) and inset image is the XPS spectra of Li 1s. (b) Na peaks at 55.7 eV in Na doped ZnO films (1 mol%).

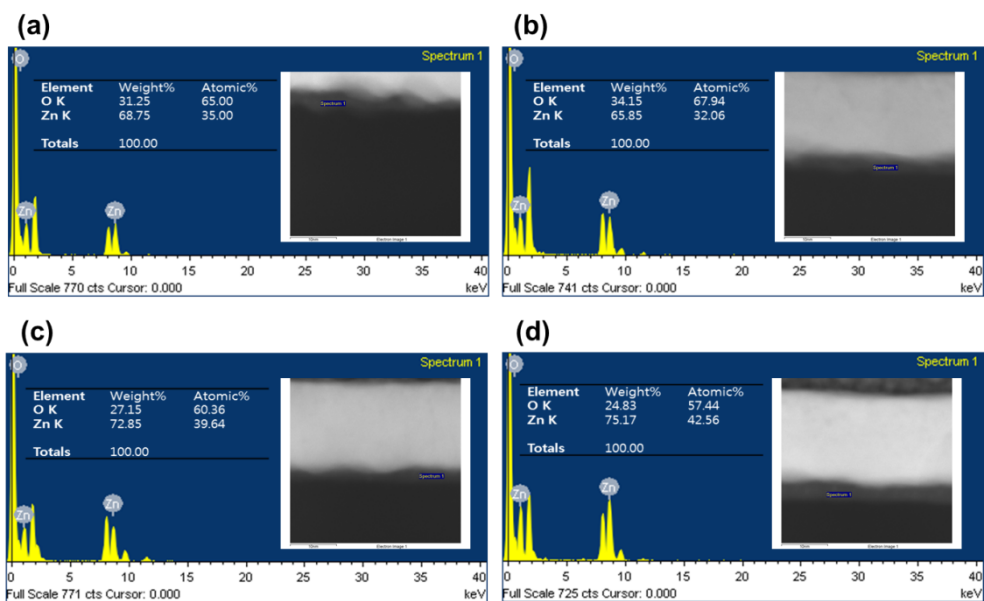


**Figure 5.12.** HR-TEM EDS results of (a) pristine and (b) Li doped ZnO (Li 1 mol%) films. (c) Li doped ZnO (Li 10 mol%) films. (d) Li doped ZnO (Li 15 mol%) films. Note that nitrogen doping was not observed in the ZnO films. All films were annealed at 300 °C for 1 hour.

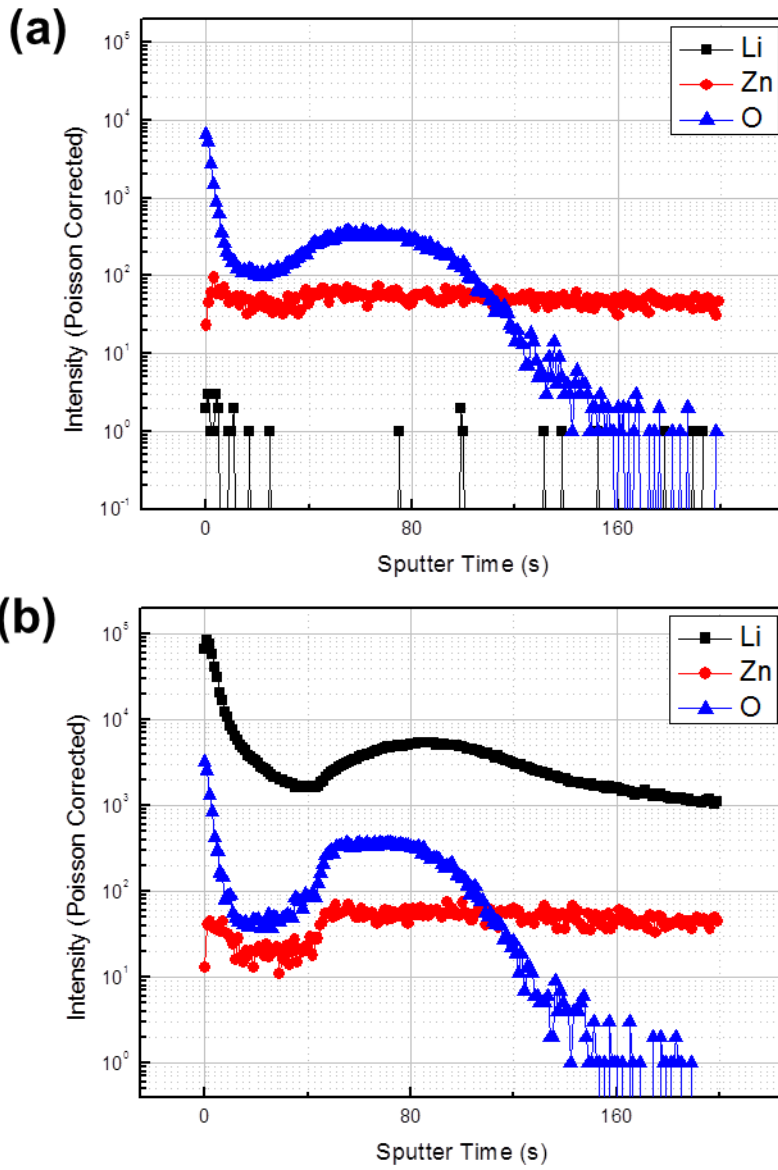


**Figure 5.13.** TOF-SIMS results of (a) pristine and (b) Li doped ZnO (Li 10 mol%) film. Etching rate and analysis area was  $0.4 \text{ \AA/s}$  and  $100 \times 100 \text{ \mu m}$ , respectively.

## 6.3 Reference

- [1] G. H. Gelinck, H. E. A. Huitema, E. Van Veenendaal, E. Cantatore, L. Schrijnemakers, J. B. P. H. Van der Putten, T. C. T. Geuns, M. Beenhakkers, J. B. Giesbers, B. H. Huisman, E. J. Meijer, E. M. Benito, F. J. Touwslager, A. W. Marsman, B. J. E. Van Rens, D. M. De Leeuw, *Nat. Mater.* **2004**, 3, 106.
- [2] M. Grundmann, H. Frenzel, A. Lajn, M. Lorenz, F. Schein, H. von Wenckstern, *Phys. Status. Solidi. A.* **2010**, 207, 1437.
- [3] U. Ozgur, Y. I. Alivov, C. Liu, A. Teke, M. A. Reshchikov, S. Dogan, V. Avrutin, S. J. Cho, H. Morkoc, *J. Appl. Phys.* **2005**, 98.
- [4] H. Frenzel, A. Lajn, H. von Wenckstern, M. Lorenz, F. Schein, Z. P. Zhang, M. Grundmann, *Adv. Mater.* **2011**, 23, 1424.
- [5] S. Masuda, K. Kitamura, Y. Okumura, S. Miyatake, H. Tabata, T. Kawai, *J. Appl. Phys.* **2003**, 93, 1624.
- [6] P. F. Carcia, R. S. McLean, M. H. Reilly, G. Nunes, *Appl. Phys. Lett.* **2003**, 82, 1117.
- [7] J. Zhu, H. Chen, G. Saraf, Z. Duan, Y. Lu, S. T. Hsu, *J. Electron. Mater.* **2008**, 37, 1237.
- [8] S. J. Lim, J. M. Kim, D. Kim, S. Kwon, J. S. Park, H. Kim, *J. Electrochem. Soc.* **2010**, 157, H214.
- [9] E. Fortunato, P. Barquinha, A. Pimentel, L. Pereira, G. Goncalves, R. Martins, *Phys. Status. Solidi-R.* **2007**, 1, R34.
- [10] K. Nomura, H. Ohta, A. Takagi, T. Kamiya, M. Hirano, H. Hosono, *Nature.* **2004**, 432, 488.
- [11] H. J. In, O. K. Kwon, *IEEE Electron. Device. L.* **2009**, 30, 377.

- [12] H. C. Huang, T. E. Hsieh, *Nanotechnology*. **2010**, 21.
- [13] S. T. Meyers, J. T. Anderson, C. M. Hung, J. Thompson, J. F. Wager, D. A. Keszler, *J. Am. Chem. Soc.* **2008**, 130, 17603.
- [14] L. Zhang, J. Li, X. W. Zhang, X. Y. Jiang, Z. L. Zhang, *Appl. Phys. Lett.* **2009**, 95.
- [15] J. Kim, S. H. Lim, Y. S. Kim, *J. Am. Chem. Soc.* **2011**, 133, 2010.
- [16] J. S. Park, W. J. Maeng, H. S. Kim, J. S. Park, *Thin Solid Films*. **2012**, 520, 1679.
- [17] K. Nomura, H. Ohta, K. Ueda, T. Kamiya, M. Hirano, H. Hosono, *Science*. **2003**, 300, 1269.
- [18] S. Y. Park, B. J. Kim, K. Kim, M. S. Kang, K. H. Lim, T. Il Lee, J. M. Myoung, H. K. Baik, J. H. Cho, Y. S. Kim, *Adv. Mater.* **2012**, 24, 834.
- [19] K. Kim, S. Park, J. B. Seon, K. H. Lim, K. Char, K. Shin, Y. S. Kim, *Adv. Funct. Mater.* **2011**, 21, 3546.
- [20] R. Theissmann, S. Bubel, M. Sanlialp, C. Busch, G. Schierning, R. Schmechel, *Thin Solid Films*. **2011**, 519, 5623.
- [21] K. K. Banger, Y. Yamashita, K. Mori, R. L. Peterson, T. Leedham, J. Rickard, H. Sirringhaus, *Nat. Mater.* **2011**, 10, 45.
- [22] M. G. Kim, M. G. Kanatzidis, A. Facchetti, T. J. Marks, *Nat. Mater.* **2011**, 10, 382.
- [23] Y. Ka, E. Lee, S. Y. Park, J. Seo, D. G. Kwon, H. H. Lee, Y. Park, Y. S. Kim, C. Kim, *Org. Electron.* **2013**, 14, 100.
- [24] International Union of Crystallography., Published for the International Union of Crystallography by Munksgaard, Copenhagen 1983, v.
- [25] G. Adamopoulos, A. Bashir, S. Thomas, W. P. Gillin, S. Georgakopoulos,

- M. Shkunov, M. A. Baklar, N. Stingelin, R. C. Maher, L. F. Cohen, D. D. C. Bradley, T. D. Anthopoulos, *Adv. Mater.* **2010**, 22, 4764.
- [26] J. C. Park, S. Kim, S. Kim, C. Kim, I. Song, Y. Park, U. I. Jung, D. H. Kim, J. S. Lee, *Adv. Mater.* **2010**, 22, 5512.
- [27] R. B. M. Cross, M. M. De Souza, *Appl. Phys. Lett.* **2006**, 89.
- [28] P. T. Liu, Y. T. Chou, L. F. Teng, *Appl. Phys. Lett.* **2009**, 95.
- [29] K. Park, S. H. Park, E. Kim, J. D. Kim, S. Y. An, H. S. Lim, H. H. Lee, D. H. Kim, D. Y. Ryu, D. R. Lee, J. H. Cho, *Chem. Mater.* **2010**, 22, 5377.
- [30] R. B. Wehrspohn, M. J. Powell, S. C. Deane, I. D. French, P. R. I. Cabarrocas, *Appl. Phys. Lett.* **2000**, 77, 750.
- [31] K. Suemori, S. Uemura, M. Yoshida, S. Hoshino, N. Takada, T. Kodzasa, T. Kamata, *Appl. Phys. Lett.* **2007**, 91.
- [32] J. Lee, S. Cha, J. Kim, H. Nam, S. Lee, W. Ko, K. L. Wang, J. Park, J. Hong, *Adv. Mater.* **2011**, 23, 4183.
- [33] C. H. Park, S. B. Zhang, S. H. Wei, *Phys. Rev. B.* **2002**, 66.
- [34] D. C. Look, R. L. Jones, J. R. Sizelove, N. Y. Garces, N. C. Giles, L. E. Halliburton, *Physica. Status. Solidi. a-Applied Research.* **2003**, 195, 171.
- [35] H. Hosono, *J. Non-Cryst. Solids.* **2006**, 352, 851.
- [36] G. Srinivasan, R. T. R. Kumar, J. Kumar, *J. Sol-Gel. Sci. Techn.* **2007**, 43, 171.
- [37] K. H. Kim, K. C. Park, D. Y. Ma, *J. Appl. Phys.* **1997**, 81, 7764.
- [38] A. Sarkar, S. Ghosh, S. Chaudhuri, A. K. Pal, *Thin Solid Films.* **1991**, 204, 255.
- [39] S. Karamat, S. Mahmood, J. J. Lin, Z. Y. Pan, P. Lee, T. L. Tan, S. V. Springham, R. V. Ramanujan, R. S. Rawat, *Appl. Surf. Sci.* **2008**, 254, 7285.

- [40] E. A. Meulenkaamp, *J. Phys. Chem. B.* **1998**, 102, 5566.
- [41] P. Barquinha, *Transparent oxide electronics: from materials to devices*, Wiley, Hoboken, N.J. **2012**.
- [42] T. Kamiya, K. Nomura, H. Hosono, *J. Disp. Technol.* **2009**, 5, 273.
- [43] B. E. Sernelius, K. F. Berggren, Z. C. Jin, I. Hamberg, C. G. Granqvist, *Phys. Rev. B.* **1988**, 37, 10244.
- [44] D. Adler, L. P. Flora, S. D. Senturia, *Solid. State. Commun.* **1973**, 12, 9.
- [45] W. H. Jeong, G. H. Kim, H. S. Shin, B. Du Ahn, H. J. Kim, M. K. Ryu, K. B. Park, J. B. Seon, S. Y. Lee, *Appl. Phys. Lett.* **2010**, 96.
- [46] G. H. Kim, W. H. Jeong, B. Du Ahn, H. S. Shin, H. J. Kim, H. J. Kim, M. K. Ryu, K. B. Park, J. B. Seon, S. Y. Lee, *Appl. Phys. Lett.* **2010**, 96.
- [47] J. G. Lu, Y. Z. Zhang, Z. Z. Ye, Y. J. Zeng, H. P. He, L. P. Zhu, J. Y. Huang, L. Wang, J. Yuan, B. H. Zhao, X. H. Li, *Appl. Phys. Lett.* **2006**, 89.

# Chapter 7. Enhancement of Electrical Properties for ZnO Thin Film Transistors by Alkali Earth Metal

## Doping

### 7.1 Introduction

Devices on a flexible substrate possess enormous advantages in actual use, such as excellent portability, light-weight, and contact on the curved surfaces. In addition, transparency is the new term for innovations related to future display applications, such as e-sign, e-paper and smart window. Hence, the manufacturing of flexible and transparent devices is becoming the crucial point for opening the door to the next generation of display devices. To actualize these devices, thin film transistors (TFTs), which are used as switching devices in display devices, need proper physical and electrical characteristics, such as flexibility, transparency, good bias stability, and high mobility.<sup>1</sup> Metal oxide semiconductors, such as ZnO and In<sub>2</sub>O<sub>3</sub> have attracted many researchers because of unique properties, such as transparency and high electron mobility which have been attributed to the overlap of s-orbital structure of transition metal ion.<sup>2</sup> Since the demonstration of indium gallium zinc oxide (IGZO) TFTs by Nomura *et al.*, much effort has been made in research on quaternary metal oxide TFTs to investigate elements that could be used in next generation display applications.<sup>3,4</sup> Vacuum-processed metal oxide semiconductor TFTs have ensured high quality performance, reproducibility, and reliability. However, in next generation display applications, they still have the problems of high facility investment and costs incurred by batch process. Also, the vacuum process has an inherent limitation for continuous fabrication process such

as roll to roll process, which is essential for large-area display devices. Therefore, the development of the process in ambient conditions of solution-processed metal oxide TFTs is critical on advanced display devices with low-cost and large-area manufacturing ability.<sup>5,6,7</sup>

Recently, the various solution-processed and high-performance quaternary metal oxide TFTs that showed a field effect mobility of 3.2–8 cm<sup>2</sup>/V·s have been reported.<sup>8,9</sup> Although quaternary metal oxides, including indium, TFTs show high electrical performance due to large s-orbitals of indium, a serious problem remains that indium is suffering from high cost, uneven and scarce deposits, which make indium strategically important material. We previously introduced alkali metal dopants for solution-processed In-free ZnO semiconductors and reported how to affect the electrical performance of ZnO TFTs.<sup>10,11</sup> In this chapter, we studied magnesium and calcium, alkali earth metal, as new n-type dopants for aqueous-derived In-free ZnO semiconductor. These dopants drastically improved electrical performance of solution-processed ZnO semiconductor, such as field effect mobility and bias stability. In this study, AFM and HR-TEM were carried out to investigate the morphology and crystal structure of an alkali earth metal doped ZnO semiconductor. In addition, the variation of activation energy for interface charge trap creation and carrier concentrations regarding as doping concentration were calculated using a stretched exponential equation and Hall measurement, respectively.

## **7.2 Results and discussion**

### **7.2.1 Electrical properties of alkali earth metal doped ZnO**

## TFTs

Figure 6.1.a shows the mechanism for the formation of a ZnO semiconductor from the zinc ammine complex precursor. Unlike general precursors with the carbonyl group, this aqueous ammonia-derived ZnO precursor can be easily transformed into a ZnO semiconductor under a low-temperature annealing process. The alkali earth metal dopants were mixed with an aqueous ammonia-derived ZnO precursor as the form of hydroxide such as  $\text{Ca}(\text{OH})_2$  and  $\text{Mg}(\text{OH})_2$ . Using the aqueous ZnO precursors including alkali earth metal dopants, TFTs with bottom gate, top contact geometries were fabricated on Si wafer. Figure 6.1.b shows the transfer curves of alkali earth metal doped ZnO TFTs with annealing process at 300 °C. The drain current of alkali earth metal doped ZnO TFTs was drastically increased. The maximum drain current of pristine, Mg doped (0.002 mol%), and Ca doped ZnO TFTs (0.2 mol%) were 0.153 mA, 1.16 mA and 1.37 mA, respectively. We calculated the field effect mobility and these results were shown in table 4. Ca doped ZnO TFTs (0.2 mol%) showed the highest mobility of 6.0  $\text{cm}^2/\text{V}\cdot\text{s}$  and Mg doped ZnO TFTs (0.002 mol %) showed the mobility of 4.86  $\text{cm}^2/\text{V}\cdot\text{s}$ . Figure 6.2 shows the output characteristics of alkali earth metal doped ZnO TFTs with a high saturation drain current of 1 mA. Contrary to alkali metal dopants such as lithium and sodium, both of magnesium and calcium dopants have low doping concentrations to ZnO semiconductor because alkali earth metal hydroxides have limitation of solubility in water. For this reason, it was hard to investigate the tendency of field effect mobility with various doping concentrations.

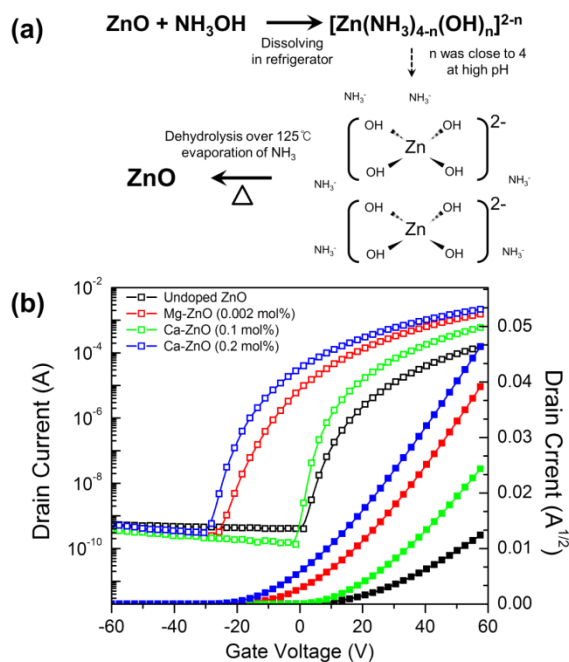


**Figure 6.1.** (a) mechanism of formation of aqueous precursor-derived ZnO, (b) transfer curves of TFTs based on ZnO semiconductor doped with various alkali earth metals (Mg 0.002 mol%, Ca 0.1 mol%, Ca 0.2 mol%).

Type of TFTs	Field effect mobility ( $\text{cm}^2/\text{V}\cdot\text{s}$ )	Turn on voltage (V)	On/off current ratio
Pristine ZnO	1.34	19	$10^5$
Mg doped ZnO	4.86	-10	$10^6$
Ca doped ZnO	6.0	-12	$10^7$

**Table 4.** Field effect mobility and turn on voltage of TFTs based on pristine and alkali earth metal doped ZnO films annealed at 300 °C with SiO<sub>2</sub> gate dielectric (Mg 0.002 mol%, Ca 0.2 mol%).

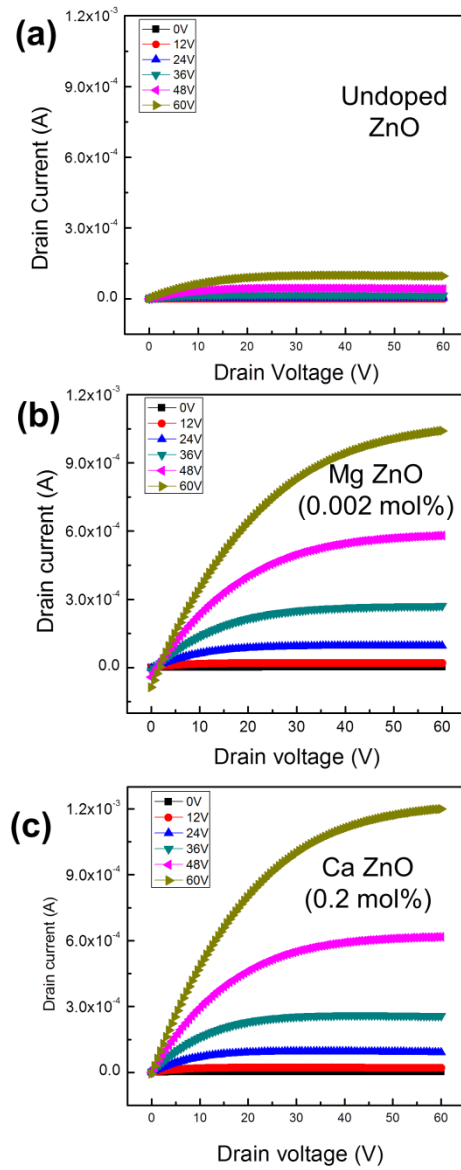


**Figure 6.2.** Output characteristic of various ZnO TFTs. (a) pristine ZnO TFT, (b) Mg doped ZnO TFT (0.002 mol%), (c) Ca doped ZnO TFT (0.2 mol%).

## 7.2.2 Carrier concentration of alkali earth metal doped ZnO films

In general, alkali earth metal dopant, especially magnesium (Mg), is well known as a suppressor of zinc interstitials or oxygen vacancies because of the ionic character of the Mg–O bonds is stronger than that of the Zn–O bonds.<sup>12</sup> This bonding preference was induced by a stronger affinity of Mg ( $E^\circ = -2.37$  V) for oxygen than Zn ( $E^\circ = -0.76$  V) for oxygen in ZnO.<sup>13</sup> Therefore, magnesium dopants reduce carrier electrons in the ZnO films because of the decrease in the oxygen vacancy serving as a source of carriers, thus reducing the Fermi level. Using alkali earth metal dopants as the carrier suppressor, transparent conducting oxide (TCO) materials, such as indium oxide and indium zinc oxide, can be transformed as semiconductors of TFTs.<sup>12,13</sup> In this study, however, the alkali earth metal dopants did not show the general behavior of a carrier suppressor. Interestingly, an increase in drain current at a fixed gate voltage was observed upon the introduction of Mg and Ca into ZnO films up to 0.002 mol% and 0.2 mol%, respectively (Figure 6.1). This demonstrates that Mg and Ca dopants did not reduce electron transport through ZnO. This unusual increase in drain current might have been occurred by the location of alkali earth metal dopants on the interstitial site of ZnO matrix.

Previously, we reported that group-I dopants locate in the interstitial site and act as shallow donors, and that Li doped ZnO TFTs show a negative shift in turn-on voltage ( $V_{on}$ ).<sup>10</sup> Analogously, alkali earth metal doped ZnO TFTs showed the same negative shift of  $V_{on}$ . Bang *et al.* controlled carrier concentration by various post-annealing temperature of ALD processed ZnO films. The carrier concentration of

the ZnO film rapidly increased from  $1.3 \times 10^{15}$  to  $2.1 \times 10^{19} \text{ cm}^{-3}$ , and TFTs showed enhancement of field effect mobility from 1.2 to  $1.9 \text{ cm}^2/\text{V}\cdot\text{s}$ . In addition, turn-on voltage and threshold voltage shifted to negative voltage.<sup>14</sup> A Hall measurement for various ZnO films was carried out to investigate a more exact relation between carrier concentration and electron mobility. Inducing alkali earth metal dopants caused a decrease in the resistivity of ZnO films (Figure 6.3.a). Figure 6.3.b shows a plot of the field effect mobility of various ZnO TFTs vs. bulk carrier concentration. The field effect mobility increased in accordance with increments in carrier concentration, which was induced by alkali earth metals doping. Although this trend is opposite to silicon semiconductor, Hosono *et al.* well explained these phenomena with the percolation conduction theory, in which the transport of free electrons in a conduction band is limited by a potential barrier above conduction band maximum.<sup>14</sup> Also, solution-processed ZnO semiconductors tend to be a polycrystalline structure and create much more defect that act as a potential barrier. This potential barrier impedes electron transportation through conduction band and eventually induces degradation of the field effect mobility. Increased carrier concentration affect effective carrier which contribute electron transporting in conduction band. This means that increased electron density raise probability which electron could be transport in the extended states. Considering our results and polycrystalline theory, we speculated that alkali earth metals locate in the interstitial site of ZnO and act as shallow donors, which increases the carrier concentration of ZnO semiconductor layer by doping.

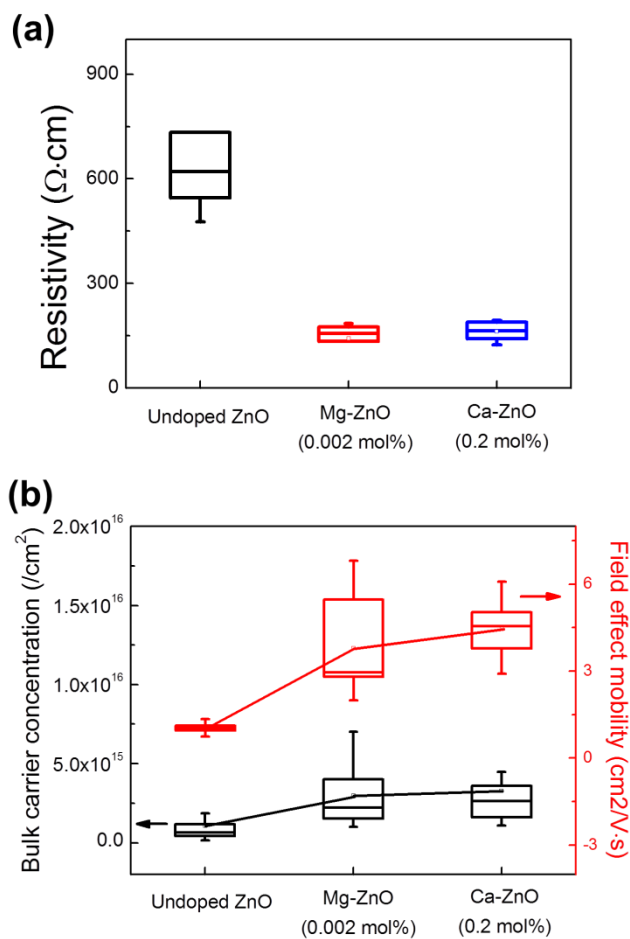


**Figure 6.3.** Electrical properties of alkali earth metal doped ZnO films, (a) resistivity data of alkali earth metal doped ZnO films by Hall measurement, (b) bulk carrier concentration and the field effect mobility of ZnO TFTs as a function of various alkali earth metals.

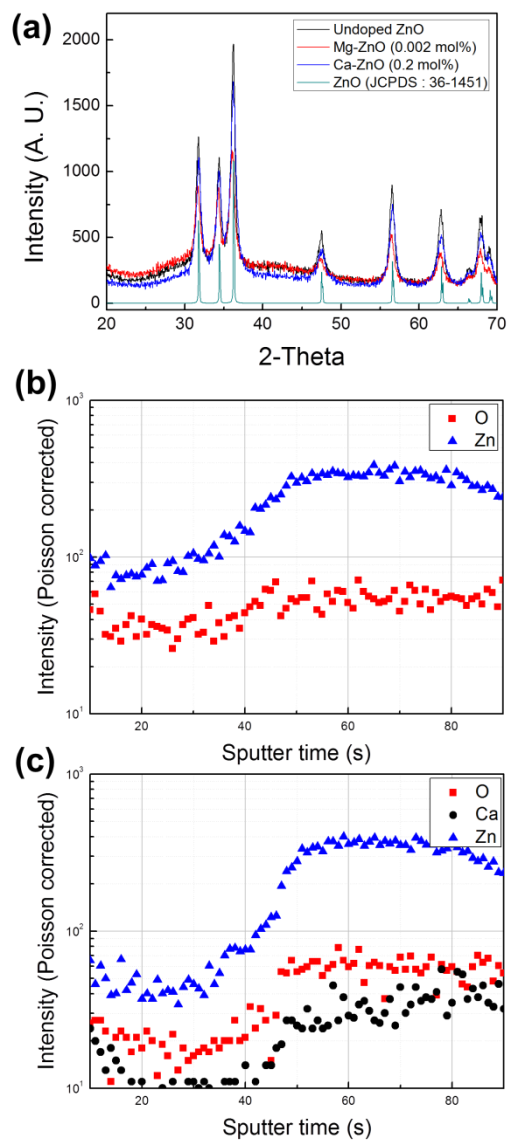
### 7.2.3 Analysis of alkali earth metal doped ZnO films

Magnesium is generally used for band gap engineering due to its large bandgap energy (6.3 eV). Also, MgO is used as heterostructured semiconductors which are composed of layers of MgO and ZnO. These heterostructured semiconductor devices provide carrier or optical confinement such as LEDs, laser, and high electron mobility transistors.<sup>16</sup> For investigating the existence of alkali earth metal oxides, XRD was carried out. In Figure 6.4.a, MgO and CaO bonding were not detected within XRD resolution. This XRD analysis clearly showed that the Mg and Ca dopants were solely located in the ZnO matrix as interstitial doping. The lack of the MgO or CaO pattern in XRD does not necessarily indicate the Mg or Ca is an interstitial dopant. Also, a Ca peak was detected in TOF-SIMS data (figure 6.4.b and c), which is the evidence of well distribution of Ca in the ZnO matrix. These results are not sufficient to draw a conclusion on the location of the dopant. However, it is very hard to detect the alkali earth metal cation in ZnO semiconductor due to thin ZnO films (5–7 nm) and a small quantity of dopant. Hence, we prepared alkali earth metal doped ZnO powders from the same alkali earth metal doped ZnO precursors. Instead of spin coating, we just dried alkali earth metal doped ZnO precursors at 300 °C and carried out Inductively Coupled Plasma-Atomic Emission Spectroscopy (ICP-AES). The 651 ppm was detected in the case of calcium cation dopant.<sup>17</sup>

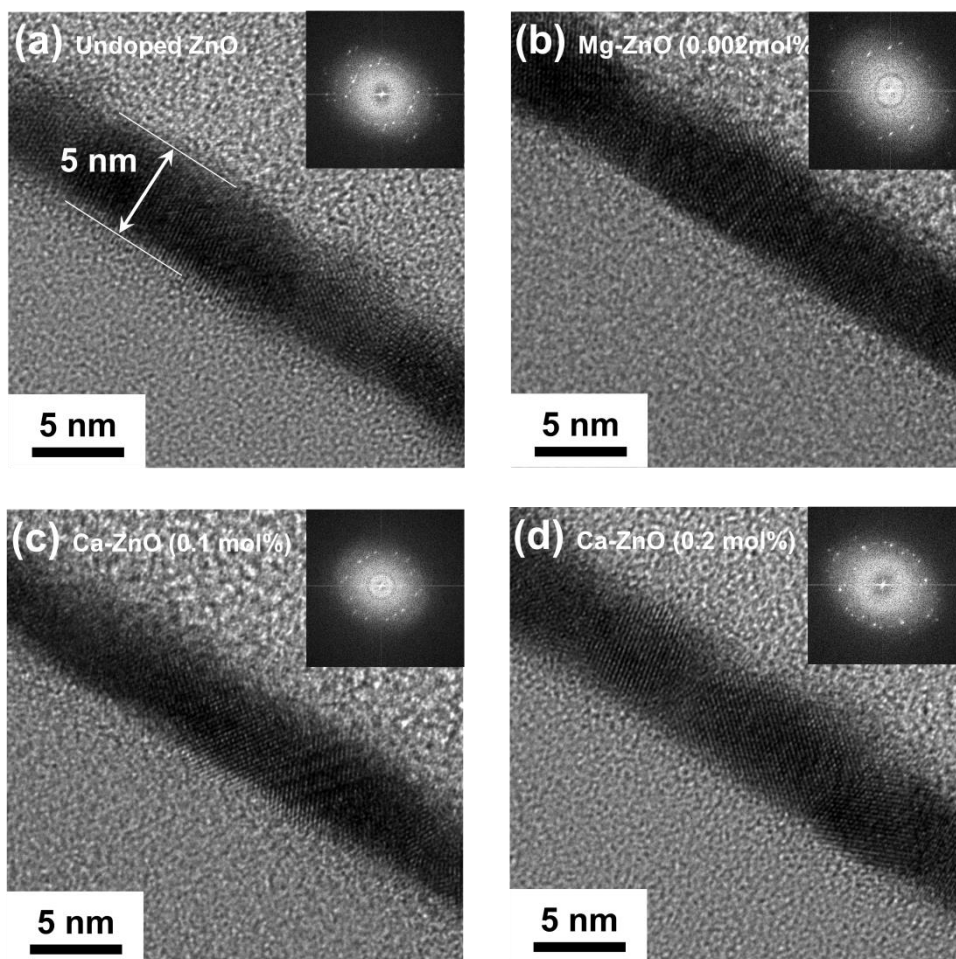
We also investigated the morphology of pristine and alkali metals doped ZnO film, because the electrical performance of polycrystalline ZnO TFTs are affected by film conditions, such as lattice distortion, morphology, or grain boundary.<sup>18,19</sup>

Figure 6.5 shows cross-sectional HR-TEM images of alkali earth metal doped ZnO

films. Each inset image shows Fast Fourier Transform Selected Area Electron Diffraction (FFT-SAED) patterns. We could not observe any remarkable lattice distortion or migration induced by alkali earth metal doping. The root mean square roughness is shown in Figure 6.6. The values were 0.32 nm (pristine ZnO), 0.41 nm (Mg doped ZnO with 0.002 mol%), 0.36 nm (Ca doped ZnO with 0.1 mol%), and 0.40 nm (Ca doped ZnO with 0.2 mol%), respectively. Because the changes in lattice distortion and roughness in various ZnO films were negligible, we concluded that there were no strong relations between the field effect mobility and morphology of various ZnO films.



**Figure 6.4.** (a) XRD profiles of the pristine and alkali earth metal doped ZnO powder, (b) TOF-SIMS data of pristine ZnO film, (c) TOF-SIMS data of Ca doped ZnO film (0.2 mol%).



**Figure 6.5.** Cross-sectional HR-TEM images of alkali earth metal doped ZnO films on the SiO<sub>2</sub> substrate at annealing temperature 300 °C. (a) pristine ZnO film, (b) Mg doped ZnO film with 0.002 mol%, (c) Ca doped ZnO film with 0.1 mol%, (d) Ca-doped ZnO film with 0.2 mol%. The inset image shows crystalline FFT-SAED patterns.

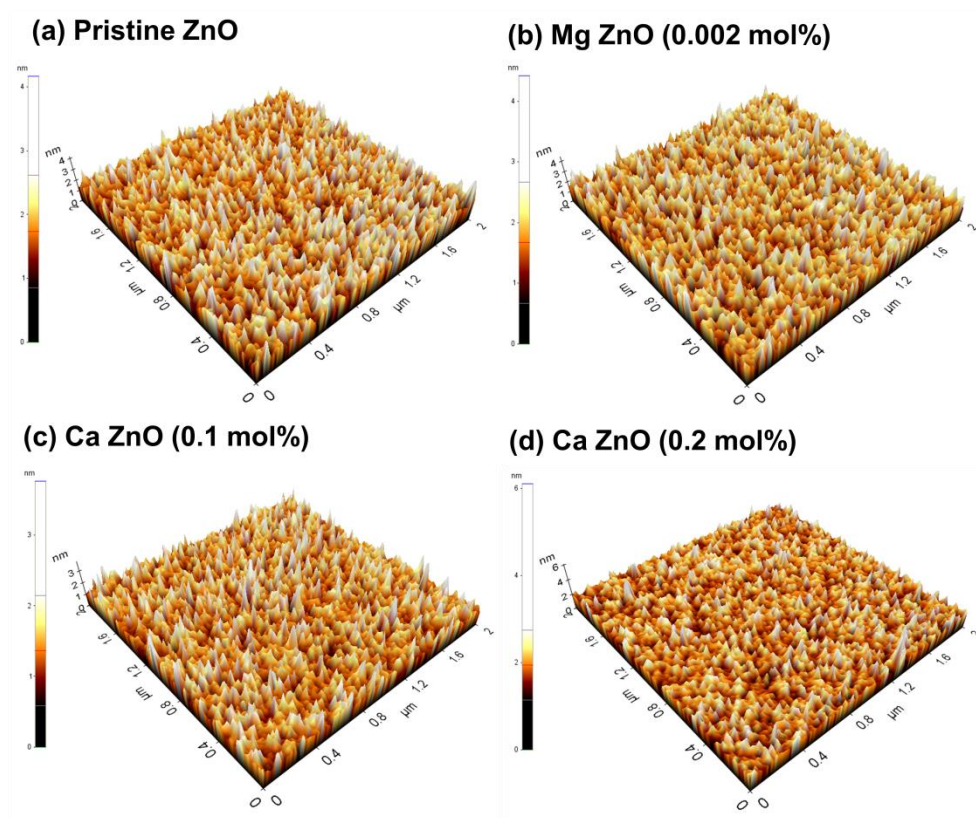


**Figure 6.6.** Atomic force microscopy (AFM) images of alkali earth metal doped ZnO films. The root mean square (RMS) roughness values of ZnO films were 0.32 nm (pristine ZnO), 0.41 nm (Mg 0.002 mol%), 0.36 nm (Ca 0.1 mol%), and 0.408 nm (Ca 0.2 mol%).

## 7.2.4 Positive bias test of alkali earth metal doped ZnO TFTs

TFTs in the backplane of advanced display devices should be stable in operation. We found that alkali earth metal doping enhances the stability of ZnO TFTs. The alkali earth metal doped ZnO TFTs showed little hysteresis, which induces the looping transistor characteristics.<sup>20</sup> Figure 6.7 shows hysteresis of current between forward and reverse gate voltage was negligible and consistently stable under bias stress.<sup>21</sup> 40 voltage of positive bias was applied at gate electrode for 4800 seconds. Despite intrinsic nanocrystalline ZnO films, small shifts of threshold voltage were also observed because the alkali earth metal dopants could fill the traps of grain boundary of the ZnO matrix (figure 6.8.a, b, and c).<sup>22</sup> Figure 6.8.d shows stable values of relative field effect mobility during prolonged stress. The curves of  $\Delta V_{th}$  vs. the bias time are shown in figure 6.8.e. The amount of activation energy required for trap creation was calculated using a stretched exponential equation (table 5).<sup>23</sup> Elevated activation energy for trap creation explains the small shift in drain current when TFTs are stressed with a positive bias (figure 6.8.f). In addition, alkali earth metal doped ZnO TFTs showed highly stable properties under the negative bias test (figure 6.9). Figure 6.10 showed the variation in  $V_{th}$  of various ZnO TFTs to which 40 V and -40 V of gate bias stress was applied.

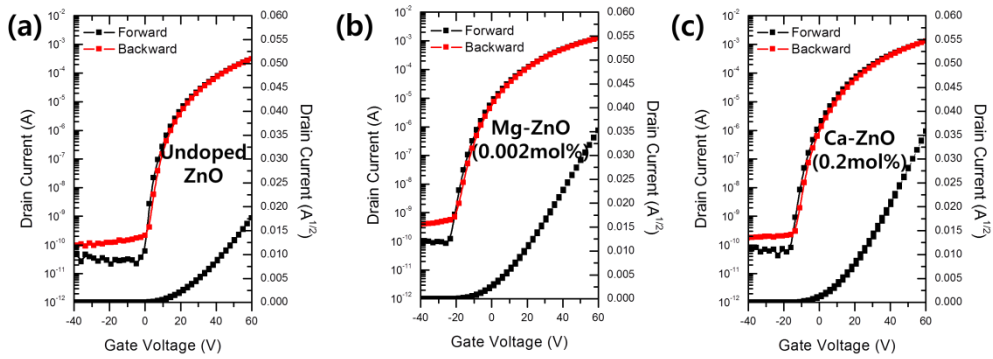


**Figure 6.7.** The hysteresis behavior of undoped and alkali earth metal doped ZnO TFTs with SiO<sub>2</sub> gate dielectric. (a) undoped ZnO, (b) Mg-ZnO (Mg 0.002 mol%), (c) Ca-ZnO (Ca 0.2 mol%).

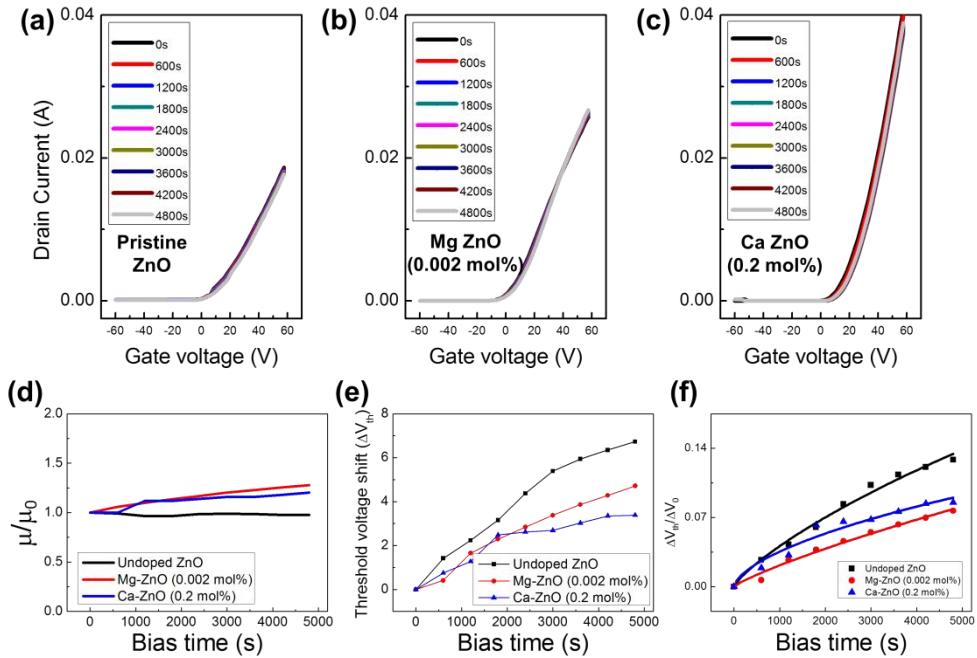


**Figure 6.8.** (a), (b) and (c) evolution of the linear transfer curves of various ZnO TFTs, as a function of positive bias stress time (40 V, 0–4800 s), (d) relative field effect mobility of various ZnO TFTs, as a function of bias stress time (0–4800 s), (e) relative threshold voltage shift ( $\Delta V_{th}$ ) of various ZnO TFTs as a function of stress time, and (f) plot of  $\Delta V_{th}/V_0$  vs. bias stress time for pristine, Mg (0.002 mol%) and Ca doped ZnO (0.2 mol%) TFTs.

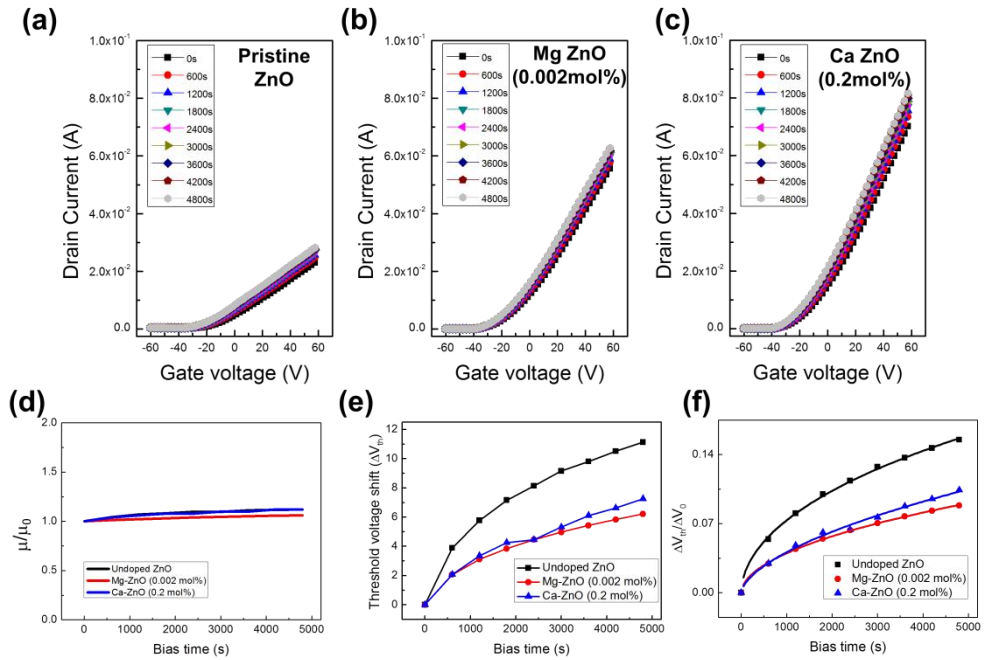


**Figure 6.9.** (a), (b) and (c) evolution of the linear transfer curves of various ZnO TFTs, as a function of negative bias stress time (-40 V, 0–4800 s), (d) relative field effect mobility of various ZnO TFTs, as a function of bias stress time (0–4800 s), (e) relative threshold voltage shift ( $\Delta V_{th}$ ) of various ZnO TFTs as a function of stress time, (f) plot of  $\Delta V_{th}/V_0$  vs. bias stress time for pristine, Mg (0.002 mol%) and Ca doped ZnO (0.2 mol%) TFTs.

Fitting parameter	Pristine ZnO	Mg doped ZnO (0.002 mol%)	Ca doped ZnO (0.2 mol%)
$E_A$ (eV)	0.5017 ( $\pm 0.0054$ )	0.54126 ( $\pm 0.01756$ )	0.5140 ( $\pm 0.00692$ )
$k_B T_0$ (eV)	0.0298 ( $\pm 0.0018$ )	0.03855 ( $\pm 0.00516$ )	0.02819 ( $\pm 0.00191$ )

**Table 5.**  $E_A$  and  $k_B T_0$  of pristine, Mg (0.002 mol%), and Ca doped ZnO TFTs (0.2 mol%).

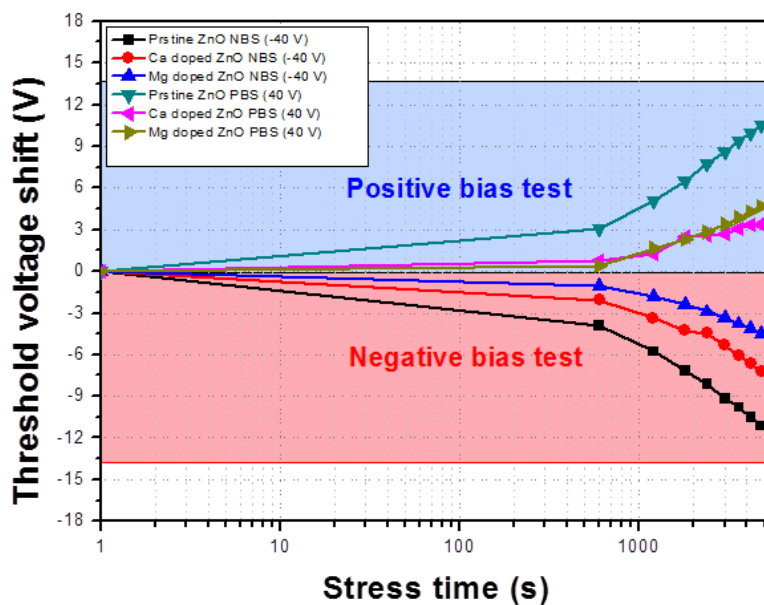


**Figure 6.10.** Variation in  $V_{th}$  of various ZnO TFTs to which 40 V and -40 V of gate bias stress was applied.

### 7.3 Reference

- [1] J. S. Park, W. J. Maeng, H. S. Kim, J. S. Park, *Thin Solid Films*. **2012**, 520, 1679.
- [2] H. Hosono, *J. Non-Cryst. Solids*. **2006**, 352, 851.
- [3] K. Nomura, H. Ohta, K. Ueda, T. Kamiya, M. Hirano, H. Hosono, *Science*. **2003**, 300, 1269.
- [4] M. Grundmann, H. Frenzel, A. Lajn, M. Lorenz, F. Schein, H. von Wenckstern, *Phys. Status. Solidi. A*. **2010**, 207, 1437.
- [5] G. Adamopoulos, A. Bashir, W. P. Gillin, S. Georgakopoulos, M. Shkunov, M. A. Baklar, N. Stingelin, D. D. C. Bradley, T. D. Anthopoulos, *Adv. Funct. Mater.* **2011**, 21, 525.
- [6] P. Atanasova, D. Rothenstein, J. J. Schneider, R. C. Hoffmann, S. Dilfer, S. Eiben, C. Wege, H. Jeske, J. Bill, *Adv. Mater.* **2011**, 23, 4918.
- [7] Y. J. Zeng, M. Menghini, D. Y. Li, S. S. Lin, Z. Z. Ye, J. Hadermann, T. Moorkens, J. W. Seo, J. P. Locquet, C. Van Haesendonck, *Phys. Chem. Chem. Phys.* **2011**, 13, 6931.
- [8] K. K. Banger, Y. Yamashita, K. Mori, R. L. Peterson, T. Leedham, J. Rickard, H. Sirringhaus, *Nat. Mater.* **2011**, 10, 45.
- [9] M. G. Kim, M. G. Kanatzidis, A. Facchetti, T. J. Marks, *Nat. Mater.* **2011**, 10, 382.
- [10] S. Y. Park, B. J. Kim, K. Kim, M. S. Kang, K. H. Lim, T. Il Lee, J. M. Myoung, H. K. Baik, J. H. Cho, Y. S. Kim, *Adv. Mater.* **2012**, 24, 834.
- [11] K. Kim, S. Park, J. B. Seon, K. H. Lim, K. Char, K. Shin, Y. S. Kim, *Adv. Funct. Mater.* **2011**, 21, 3546.

- [12] G. H. Kim, W. H. Jeong, B. Du Ahn, H. S. Shin, H. J. Kim, H. J. Kim, M. K. Ryu, K. B. Park, J. B. Seon, S. Y. Lee, *Appl. Phys. Lett.* **2010**, 96.
- [13] C. J. Ku, Z. Q. Duan, P. I. Reyes, Y. C. Lu, Y. Xu, C. L. Hsueh, E. Garfunkel, *Appl. Phys. Lett.* **2011**, 98.
- [14] S. Bang, S. Lee, J. Park, S. Park, W. Jeong, H. Jeon, *J. Phys. D: Appl. Phys.* **2009**, 42.
- [15] T. Kamiya, K. Nomura, H. Hosono, *J. Disp. Technol.* **2009**, 5, 273.
- [16] A. Janotti, C. G. Van de Walle, *Rep. Prog. Phys.* **2009**, 72.
- [17] E. A. Meulenkaamp, *J. Phys. Chem. B.* **1998**, 102, 5566.
- [18] C. Y. Tsay, H. C. Cheng, M. C. Wang, P. Y. Lee, C. F. Chen, C. K. Lin, *Surf. Coat. Tech.* **2007**, 202, 1323.
- [19] G. Adamopoulos, A. Bashir, S. Thomas, W. P. Gillin, S. Georgakopoulos, M. Shkunov, M. A. Baklar, N. Stingelin, R. C. Maher, L. F. Cohen, D. D. C. Bradley, T. D. Anthopoulos, *Adv. Mater.* **2010**, 22, 4764.
- [20] L. Zhang, J. Li, X. W. Zhang, D. B. Yu, X. Y. Jiang, Z. L. Zhang, *Phys. Status. Solidi. A.* **2010**, 207, 1815.
- [21] P. T. Liu, Y. T. Chou, L. F. Teng, *Appl. Phys. Lett.* **2009**, 95.
- [22] S. Y. Park, K. Kim, K. H. Lim, B. J. Kim, E. Lee, J. H. Cho, Y. S. Kim, *J. Mater. Chem. C.* **2013**, 1, 1383.
- [23] R. B. Wehrspohn, S. C. Deane, I. D. French, I. G. Gale, M. J. Powell, R. Bruggemann, *Appl. Phys. Lett.* **1999**, 74, 3374.

## Chapter 8. Conclusion

In conclusion, solution-processed, low-temperature, and high mobility of ZnO TFTs were developed for advanced soft electronics such as flexible, transparent display and high definition display. Beyond the indium-based metal oxide semiconductor, new dopants for ZnO semiconductor from zinc ammine complex were suggested.

First, the solution-processed ZnO TFTs using zinc ammine complexes, which were prepared using ZnO powder, intrinsic Zn(OH)<sub>2</sub>, and precipitated Zn(OH)<sub>2</sub> were fabricated. From the analysis of the reaction mechanism in the zinc ammine complex, we deduced that the same chemical intermediate (zinc ammine complex) was made from three different zinc oxide sources. In the study of <sup>1</sup>H-NMR, surface morphology by AFM, crystal structure by HR-TEM, and oxygen vacancy by XPS in the ZnO films, we confirmed the same intermediate and ZnO semiconductor film fabrication irrespective of the type of zinc oxide source for the zinc ammine complex. Consequently, they induced the analogous values of the average field effect mobility, on/off current ratio, and turn-on voltage in all ZnO TFTs. Although zinc ammine complexes for ZnO semiconductors were prepared using three different zinc oxide sources, the chemical intermediate and electrical performance were the same. These solution-processed ZnO films from zinc ammine complexes have various advantages such as low-temperature process, high electron mobility, and non-toxic aqueous solution.

Second, the new doping method by employing alkali metals to achieve high-performance and solution-processed ZnO TFTs with a low processing temperature (300 °C), which is therefore applicable to flexible plastic substrates was

demonstrated. These alkali metals in the ZnO films acted as shallow donors, which dramatically enhanced the field effect mobility of the ZnO TFTs. Li doped ZnO TFTs exhibited excellent electrical properties, i.e., an electron mobility of 7.34 cm<sup>2</sup>/V·s and an on/off current ratio of 10<sup>7</sup>. The low-voltage operation of Li doped ZnO TFTs with excellent operational stability was successfully demonstrated by using high capacitance ion gel gate dielectrics.

Third, high-performance, low-temperature and solution-processed alkali metal doped ZnO TFTs were introduced in detail and analyzed by HR-TEM, AFM, XPS, EDS, electrical bias stability test and UV-vis spectroscopy. Furthermore, the change in the optical bandgap energy of Li doped ZnO semiconductor films could be supported by the Burstein-Moss like shift showed successfully the increase and decrease of the field effect mobility of Li doped ZnO TFTs related to the doping concentrations. The optical bandgap energy ( $E_{opt}$ ) is correlated with the enhancement of the electron mobility of alkali metal doped ZnO TFTs. The broadening of the  $E_{opt}$  values, which are strongly related to the amount of excited electrons from the Fermi level in the valence band to the conduction band, was observed from the Li doped ZnO 0 mol% film to the Li doped ZnO 10 mol% film. Increased electron density raise probability which electron could be transport in the extended states. Therefore, we assume that the majority of the alkali metal ions must exist as interstitial donors in the structure rather than as substitutional acceptors and alkali metal dopants enhanced the field effect mobility.

Finally, alkali earth metals as new n-type dopants enhance substantially the electrical properties of aqueous precursor-derived ZnO TFTs with low-temperature annealing. Both magnesium and calcium locate in the interstitial site and increase the carrier concentration of the ZnO semiconductor. The Ca doped ZnO TFTs (0.2

mol%) showed best performance after annealing at 300 °C; the field effect mobility was  $6.02 \text{ cm}^2/\text{V}\cdot\text{s}$  and the on/off current ratio was  $10^7$ .

In this regard, alkali metal doped ZnO semiconductors which could facilitate the fabrication of high-performance, low-temperature, solution-processed, and indium-free TFTs for cost-effective and mass-produced TFTs for advanced displays were introduced. An in-depth study of the crystal structure, morphology, and optical bandgap of ZnO films with various dopants makes a great contribution to next generation high-performance TFTs for flexible, printed and transparent electronics.

# 국문초록

## 용액형 박막 트랜지스터를 위한 산화 아연 반도체의 소재 공정

박시윤

융합과학부

융합과학기술대학원

서울대학교

박막 트랜지스터의 활성층으로서 산화물 반도체는 투명성과 유연성과 같은 독특한 물성 때문에 널리 알려져 있다. 자동차의 HUD, 스마트 유리창, 디스플레이 탁자, 스마트 카드와 말 수 있는 디스플레이와 같이 다양한 기기와 디자인들이 산화물 반도체를 사용하여 구현되고 있다. 차세대 디스플레이 기기를 위하여 유연하고 큰 밴드갭을 가지며 운반자 농도가 조절이 가능한 반도체 물질이 필수적이다. 또한 플라스틱 기판을 이용한 유연성 기기를 위하여 저가, 대면적 생산 공정이 필요하다. 산화 아연 또는 산화물 반도체를 기반으로 하는 박막 트랜지스터가 능동형 디스플레이의 구동소자로 사용된다. 산화물 반도체 박막 트랜지스터는 투명성, 높은 전자 이동도와 점멸비 등의 장점 때문에 능동형 디스플레이의 비정질 실리콘 박막 트랜지스터를 대체하고 있다. 하지만 용액 공정, 저온 공정의 산화 아연 반도체가 보고 되었으나 여전히 낮은 전자 이동도를 가지고 있다. 이러한 관점에서 용액 공정에서 가능한 도핑 방법과 원리 분석을 위한 재료 공정이 필요하다.

첫 번째로 세 가지의 전구체로부터 제작되는 산화물 반도체 박막의 제조 박막의 최적화에 대해서 조사하였다. 산화 아민 착화합물은 암모니아의 높은 휘발성

때문에 낮은 공정온도가 가능한 전구체이다. 세 가지의 산화물 전구체로부터 산화 아연 박막을 만드는 방법 중 암모니아수에 산화아연을 직접적으로 녹이는 방법이 가장 효율적인 방법이다.

둘째로 알칼리 금속을 사용하여 산화물 반도체를 도핑하는 새로운 방법을 개발하였다. 인듐-아연 산화물, 인듐-갈륨-아연 산화물과 같은 아연 양이온을 포함하는 산화물 합금은 높은 전계 효과 이동도를 가지는 전기적 성능을 가지고 있다. 하지만, 인듐의 사용은 높은 가격과 전략적 중요성 때문에 큰 도전 과제를 가지고 있다. 알칼리 금속 양이온의 침입형 도핑은 산화물 반도체의 전자 농도를 증가시키고 전계 효과 이동도에 영향을 주게 된다. 리튬 도핑된 산화 아연 박막 트랜지스터는  $7.34 \text{ cm}^2/\text{V}\cdot\text{s}$ 의 전계 효과 이동도와  $10^7$ 의 높은 점멸비 등 우수한 전기적 특성을 보였다.

셋째로 리튬 도펀트에 집중하여 정확한 도핑 원리와 자세한 분석에 대하여 연구하였다. 알칼리 금속이 도핑된 산화물 반도체에 대하여 결정성, 표면 상태, 반도체와 절연층의 계면, 광학적 흡수율과 화학적 조성을 다양한 분석 장비를 이용하여 조사하였다. 나노결정성 구조의 산화물 안에서 알칼리 금속 양이온이 침입형 위치에 존재하고 알칼리 금속 도펀트가 산화물 반도체의 전자 농도를 증가시키게 된다. 또한 재료의 손상 없이 알칼리 금속이 도핑된 산화물의 전기적 특성을 관찰할 수 있도록 광학적 흡수율을 이용해 분광 분석을 사용하였다.

마지막으로 알칼리 토금속이 도핑된 고 이동도, 용액 공정의 산화 아연 박막 트랜지스터를 개발하였다. 일반적으로 알칼리 토금속은 산소 결핍형이나 아연 침입형에 의해 발생하는 전자 농도를 감소시키는 억제제로 널리 사용되고 있다. 하지만 아연 아민 착화합물에서는 마그네슘과 칼슘 모두 침입형 위치에 존재하고 수용액 공정의 산화 아연 반도체의 전자 농도를 증가시킨다. 300 도의 가열 공정에서 제작된 칼슘이 도핑된 산화 아연 박막 트랜지스터는  $6.02 \text{ cm}^2/\text{V}\cdot\text{s}$ 의

전계 효과 이동도와  $10^7$ 의 높은 점멸비의 높은 성능을 보였다.

결론으로 유연하고 투명한 전자소자에 사용되는 박막트랜지스터를 위해 산화 아연 반도체의 재료 공정을 진행하였다. 산화 아민 착화합물은 용액공정을 위해 사용되는 탄소기반의 산화 아연 전구체를 대체할 수 있을 것이다. 알칼리 금속과 알칼리 토금속은 산화 아연 박막트랜지스터에서 높은 전계 효과 이동도를 달성시킬 수 있는 가능성을 가지고 있다.

**Keywords :** 박막트랜지스터, 산화아연, 산화물 반도체, 리튬 도펀트

**Student Number :** 2010-22669